IMPROVED QUANTIFICATION OF CONNECTIVITY IN HUMAN BRAIN MAPPING

by

Sudhir Kumar Pathak

M.S., Carnegie Mellon University, 2006

M.Sc., Indian Institute of Technology Kanpur, 2004

Submitted to the Graduate Faculty of

Swanson School of Engineering in partial fulfillment

of the requirements for the degree of

Doctor of Philosophy

University of Pittsburgh

2015

UNIVERSITY OF PITTSBURGH

SWANSON SCHOOL OF ENGINEERING

This dissertation was presented

by

Sudhir Kumar Pathak

It was defended on

October 22, 2015

and approved by

Walter Schneider, Ph.D., Professor, Department of Psychology

George Stetten, Ph.D., Professor, Department of Bioengineering

Howard Aizenstein, Ph.D., Professor, Department of Psychiatry

John Galeotti, Ph.D., Systems Scientist, Robotics Institute, Carnegie Mellon University

Juan Fernandez Miranda, M.D., University of Pittsburgh Medical Center

Peter Basser, Ph.D., Senior Investigator, NICHD, National Institute of Health

Dissertation Director: Walter Schneider, Ph.D., Professor, Department of Psychology

IMPROVED QUANTIFICATION OF CONNECTIVITY IN
HUMAN BRAIN MAPPING

Sudhir K Pathak, Ph.D.

University of Pittsburgh, 2015

Diffusion magnetic resonance imaging (dMRI) is an advanced MRI methodology that can be used to probe the microstructure of biological tissue. dMRI can provide orientation information by modeling the process of water diffusion in white matter. This thesis presents contributions in three areas of diffusion imaging technology: diffusion reconstruction, quantification, and validation of derived metrics. It presents a novel reconstruction method by combining generalized q-sampling imaging, spherical harmonic basis functions and constrained spherical deconvolution methods to estimate the fiber orientation distribution function (ODF). This method provides improved spatial localization of brain nuclei and fiber tract separation. A novel diffusion anisotropy metric is presented that provides anatomically interpretable measurements of tracts that are robust in crossing areas of the brain. The metric, directional Axonal Volume (dAV) provides an estimate of directional water content of the tract based on the (ODF) and proton density map. dAV is a directionally sensitive metric and can separate anisotropic water content for each fiber population, providing a quantification in milliliters of water. A method is provided to map voxel-based dAV onto tracts that is not confounded by crossing areas and follows the tract morphology. This work introduces a novel textile based hollow fiber anisotropic phantom (TABIP) for validation of reconstruction and quantification methods. This provides a ground truth reference for axonal scale water tubular structures arranged in various anatomical configurations, crossing and mixing patterns. Analysis shows that: 1) the textile tracts are

iv

identifiable with scans used in human imaging and produced tracts and voxel metrics in the range of human tissue; 2) the current methods could resolve crossing at 90° and 45° but not 30°; 3) dAV/NODDI model closely matches (r=0.95) the number of fibers whereas conventional metrics poorly match (i.e., FA r=0.32). This work represents a new accurate quantification of axonal water content through diffusion imaging. dAV shows promise as a new anatomically interpretable metric of axonal connectivity that is not confounded by factors such as axon dispersion, crossing and local isotropic water content. This will provide better anatomical mapping of white matter and potentially improve the detection of axonal tract pathology.

TABLE OF CONTENTS

LIST OF TABLES

LIST OF FIGURES

PREFACE

Firstly, I would like to express my sincere gratitude to my advisor Dr. Walter Schneider for the continuous support of my Ph.D study and related research. His guidance helped me in all the time of research and writing of this thesis.

I would like to specially thank Dr. Peter Basser for his detailed comments and guidance. I also want to thank rest of my thesis committee: Dr. George Stetten, Dr. Howard Aizenstein, Dr. John Galeotti and Dr. Juan Fernandez Miranda, for their insightful comments and encouragement.

I want to specially thank Catherine Fissell who guided me throughout my thesis. Her keen eye for details provided the necessary structure for my defense and editing. I will always be indebted to her for this. I would like to thanks my fellow lab member, Deepa Krishnaswamy and Emily Cauley Braun who helped me for proofread this thesis.

My thesis is dedicated to my father, Krishna Kumar Pathak, who taught me to love and enjoy mathematics. I have also survived this experience through the blessings and strength of my wife's mother Mrs. Malathi Anilkumar who has been my biggest well-wisher. I wanted to also thank my mother and my family in Kanpur, India for their support and encouragement.

Last but not the least, I would like to thank my wife Neena and my daughter Sachi for being patient and supportive of me throughout this endeavor and my life in general.

1.0   INTRODUCTION

Understanding human brain connectivity is one of the important goals of this century. There are a number of brain function disorders potentially stemming from white matter connectivity disruption [1-14]. For example Traumatic Brain Injury represents a health care problem that costs over $100 billion annually, contributes to $1.2 trillion in societal costs, and affects the lives of over 13 million people in the United States [15]. Magnetic Resonance Imaging (MRI) is a multi-model non-invasive imaging technique to probe the structure of internal human tissue organs. One such MR imaging technique, Diffusion Magnetic Resonance Imaging (dMRI), probes the diffusion process to provide micro-structural information of human tissue. dMRI can be used to study connectivity between different functional regions in the human brain. Validated diffusion MRI based methods of measuring connectivity can be applied to neurological disorders such as stroke, brain cancer, TBI, epilepsy, autism, dyslexia, psychotic disorders, and developmental disorders [2, 16-19]. Furthermore, such methods can facilitate patient understanding of these disorders as well as enable better-targeted rehabilitation. To better diagnose connection disorders, we need non-invasive techniques that can accurately quantify brain connectivity and density of fiber tracts. There are four key steps in processing diffusion MR images, diffusion image acquisition schemes (Q-space sampling), diffusion modeling, fiber tracking and quantification of axonal volume fraction to quantify structural connectivity between functional regions and validation of diffusion models and related quantification metrics. This

thesis presents contributions to three areas in diffusion MR Imaging technology. A novel diffusion reconstruction method is presented in chapters two and three. A novel mathematical formulation of an anisotropic metric is presented in chapter four. A novel textile based anisotropic phantom is used to validate reconstruction methods and anisotropic metrics described in previous work and in this thesis.

1.1   HISTORY OF STUDYING WHITE MATTER

In the 19th and early 20th centuries post-mortem dissection (see Figure 1) was used to understand gross white matter anatomy of the human brain [2, 16-19]. Histological studies were also used to create detailed maps of connectivity in various regions of the human brain [20, 21]. Other studies involving animals have used tracers and viruses to provide a detailed map of white matter pathways [22-24]. All of these types of studies provide detailed information of white matter pathways in both the human and animal brain ex-vivo (see Figure 1). Results from these studies are limited by the subject's unique anatomical variability and specific location of functional brain regions. In the late 20th century Magnetic Resonance Imaging (MRI) became available as an in-vivo brain imaging technique and has more recently been used to study white matter connectivity.

Figure 1. Dissection of the human brain. Figure showing white matter pathways using the Klinger dissection technique. (Image is provided by Dr. Juan Fernandez Miranda)

Mansfield and Lauterbur initially developed the MRI technique in 1973 [25-27]. It grew to be widely implemented in the area of neurological imaging due to its ability to produce images of great detail and increased contrast between the soft tissue parts of the body. Unlike CT it had no exposure to radiation, which makes it a noninvasive procedure. One such MR technique is diffusion MRI, which can probe the movement of water molecules in the tissue. Imaging the diffusion of water molecules in biological tissue allows us to probe geometrical properties of the tissue and can be useful in studying structural connectivity of human brain. Diffusion MRI is an in-vivo technique to delineate white matter tracts in individual patients (see Figure 2) and healthy subjects. Thus dMRI is an ideal candidate for use in clinical studies and specifically those studies that deal with diagnosing neuro-degenerative disorders and pre-surgical planning for tumor

resection. In neuroscientific research, dMRI provides valuable information about the neural circuits involved in various cognitive tasks such as language, motor or vision [28-32]. It can be applied to the study of the human brain across the life span. It can also be used to quantify axonal degeneration in various brain disorders such as Parkinson's disease, Alzheimer's disease, Huntington's disease, ALS, etc. [14, 16, 32-34]. In neuro-surgical applications it can provide information to aid in planning the surgical route for resection of a brain tumor [2, 35].
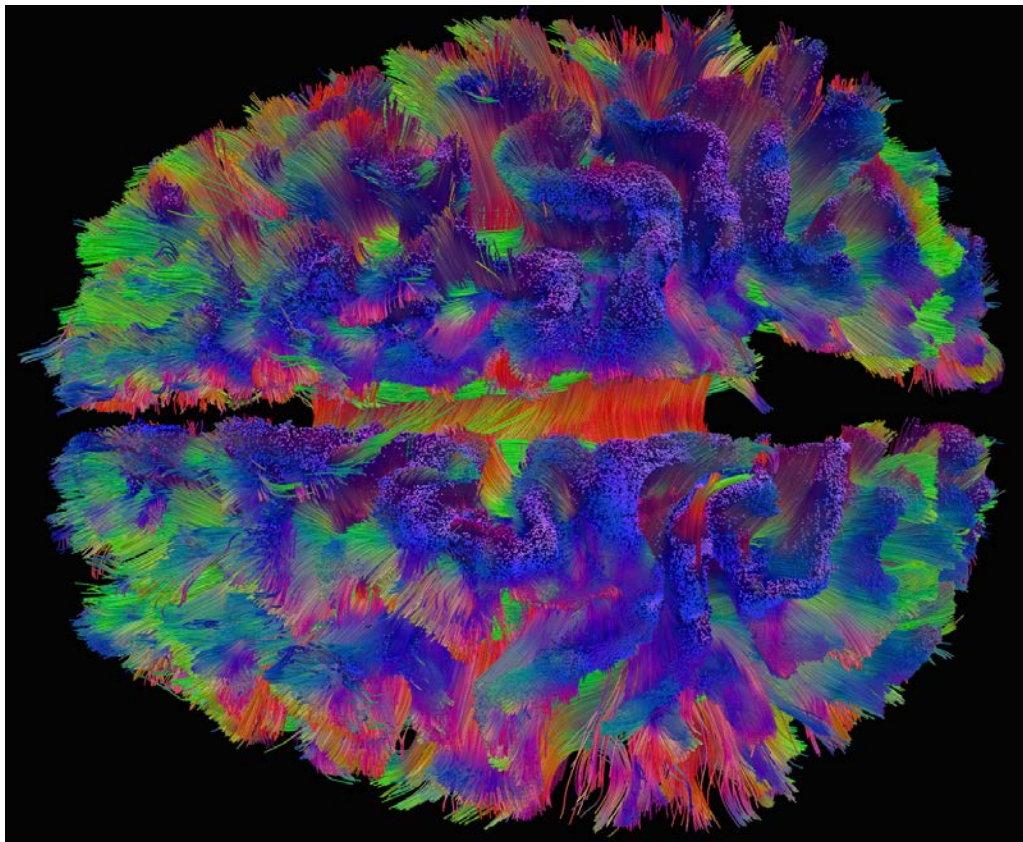
Figure 2. Whole brain tracts estimated using diffusion spectrum imaging data described in section 3.5. Advanced diffusion techniques can be used to probe white matter fiber pathways in human brain.

Processing of diffusion MRI requires multiple steps: choice of MR image acquisition, diffusion modeling, fiber tracking and quantification of anisotropic metrics. All of these steps are

dependent on each other and the choice of one step can affect the whole pipeline. This thesis work addresses diffusion modeling and quantification of fiber tracks. Chapter one provides the background on diffusion and a brief overview of diffusion imaging. Chapter two gives an overview of key diffusion models and introduces a novel reconstruction method by combining the Generalized Q-sampling Imaging [36] (GQI) and Constrained Spherical Deconvolution [37, 38] (CSD) methods. Chapter three describes the deconvolution methods in ODF space for estimation of the fiber ODF. It also shows applications of this method in fiber tracking and visualization of sub-cortical regions in the human brain. Chapter four presents a novel framework to estimate anisotropy on fiber tracts, called direction axonal volume (dAV). It uses the ODF to map anisotropic metrics along the fiber tracks. Chapter five uses a textile based anisotropic phantom to validate diffusion models and anisotropic metrics, dAV and NODDI [39].

1.2 MATHEMATICAL BASIS OF DIFFUSION

"Diffusion" is derived from the Latin word *diffundere* meaning to spread out (if a substance is spreading out). Diffusion is defined as the displacement of particles (in our case water molecules) due to physical factors such temperature or pressure from high concentration regions to low concentration regions. Diffusion is a mass transport phenomenon that doesn't require bulk motion. Other mass transport phenomena such as flow, advection and convection utilize the bulk motion of particles. For example, blood flow in the veins and arteries is due to bulk motion of blood cells in contrast to the movement/displacement of water molecules in white matter tissue, which is due to diffusion. Mathematically diffusion is characterized as the average displacement of randomly moving particles also called Brownian motion. There are two ways to

5

derive a formulation for the diffusion of particles: Fick's law and Einstein's theory of particles described below. We used Einstein's equation to formulate the probability density function of displacement of water molecules in this chapter.

1.2.1   Mathematical description of Brownian motion

Brownian motion can be described mathematically using Fick's law (phenomenological approach). For example, the diffusion of an ink drop in a glass of water can be explained by Fick's law.

According to Fick's Law, the net flux J is proportional to the spatial gradients of the concentration C of the particles (ink for example),

$$J = -D\frac{\partial C}{\partial x} \qquad\qquad (1.1)$$

where D is the diffusion coefficient.

Further, using the continuity equation, net flux J is equal to the rate of the concentration C of the particles,

$$\frac{\partial C}{\partial t} = -\frac{\partial J}{\partial x} \qquad\qquad (1.2)$$

By substituting equation 1.1 into 1.2, we can get the equation for the concentration of particles over time.

$$\frac{\partial C}{\partial t} = D\frac{\partial^2 C}{\partial x^2} \qquad\qquad (1.3)$$

The above equation describes diffusion in one dimension. The solution of equation 1.3 with

initial concentration $C(x,0) = \delta(x - x_0)$ is given by,

$$C(x,t) = \frac{1}{\sqrt{4\pi Dt}} \exp\left(-\frac{(x-x_0)^2}{4Dt}\right) = N(x \mid x_0, t, D)$$

where x_0 is the initial position of the particle and $N(x \mid x_0, t, D)$ is a Gaussian distribution with

mean x_0 and variance $2Dt$.

In three dimensions, diffusivity may depend on direction and can be represented as a

tensor of order 2. A 3×3 symmetric positive definite matrix is used to represent diffusivity in a

complex medium.

$$\frac{\partial C}{\partial t} = \nabla\left(\mathbf{D}\nabla C\right) \tag{1.4}$$

where $\mathbf{D}$ is the diffusion tensor.

Solution of equation 1.4 with initial concentration $C(\mathbf{x},0) = \delta(\mathbf{x} - \mathbf{x_0})$ is given by,

$$C(x,t) = \frac{1}{\sqrt{4\pi t \mid \mathbf{D}\mid}} \exp\left(-\frac{(\mathbf{x}-\mathbf{x_0})^T \cdot \mathbf{D}^{-1} \cdot (\mathbf{x}-\mathbf{x_0})}{2t}\right) = N(\mathbf{x} \mid \mathbf{x_0}, t, \mathbf{D}) \tag{1.5}$$

$N(\mathbf{x} \mid \mathbf{x_0}, t, \mathbf{D})$ is an anisotropic Gaussian function in 3D.

1.2.2 Einstein's Theory

Another way to describe diffusion is as a probability density function of displacement of

particles i.e., the proportion of molecules/particles that undergo a displacement $\mathbf{d}$. For example,

let the total number of molecules, N start at position $\mathbf{x_0}$ at time $t = 0$ and after time $t = \tau$ (also

called diffusion time) let them be displaced to $\mathbf{x_t}$. Diffusion can be described as the histogram of

the displacement (see Figure 3) of the population of all molecules, i.e., the probability of displacement of particles (n) that are displaced to the distance $d = \|\mathbf{x_t} - \mathbf{x_0}\|$ by,

$$p(\mathbf{d},\tau) = p(\mathbf{x_t} \mid \mathbf{x_0},\tau) = \frac{n}{N} \tag{1.6}$$

In the case of free diffusion the probability distribution function will be normally distributed by the central limit theorem. Einstein, in 1905, [40] proposed that the average displacement (root mean squared) or ensemble of displacement of particles (in one dimension) is proportional to the diffusion time τ.

$$\langle \mathbf{d} \cdot \mathbf{d}^T \rangle \propto \tau$$

$$\langle \mathbf{d} \cdot \mathbf{d}^T \rangle = 2 \cdot D \cdot \tau \tag{1.7}$$

The proportionality constant D is the diffusion coefficient that describes the viscosity of the medium. In the case of free water, the diffusion coefficient at temperature $37\,^{\circ}\mathrm{C}$ is approximately equal to $D \approx 3.0 \cdot 10^{-9}\ m^2\ s^{-1}$.
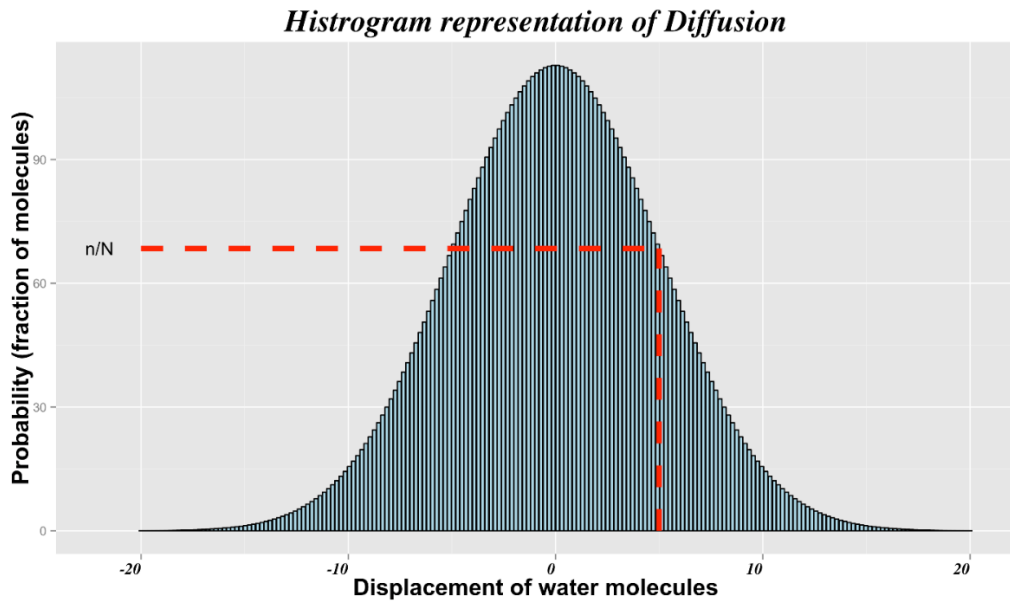
Figure 3. Histogram of displacement (in μm) of free water molecules

8

A similar principle can be used to describe the diffusion process in white matter tissue in the human brain. In a typical diffusion MRI scan, a diffusion time roughly equal to $40\,ms$ is used, which leads to mean displacement of the water molecules on the order of $d \approx 10\,\mu m$. Therefore, on a diameter scale of 1-10 μm of individual axons in a fasciculus, diffusion can be probed at the micro-structural level of information of the tissue. It is important to note that when average displacement (or corresponding diffusion time) is less than the diameter of fibers it will appear as isotropic diffusion.

The simplest model of white matter tissue can be thought of as a composition of "*densely packed, coherently oriented, impermeable, and infinitely long cylindrical axons*" (Jespersen 2012). Diffusion (or ensemble of displacement of molecules) in such an intra-cellular environment is restricted by the boundaries of the cylinder (axons).

If the diffusion time τ is long enough such that molecules can collide with surrounding boundaries, the diffusion process will no longer be free and hence the diffusion coefficient D in equation 1.7 is dependent on time. This time dependent diffusion coefficient is also known as the apparent diffusion coefficient ADC described as,

$$\langle \mathbf{d} \cdot \mathbf{d}^T \rangle = 6 \cdot D(t) \cdot \tau \qquad (1.8)$$

In reality diffusion in white matter is more complex due to the presence of different cells and the complex structure of axons. First, diffusion inside and outside (intra and extra-cellular) the axons is modeled separately as multiple compartments [41-43] with corresponding diffusivity constants and volume fractions for each compartment. Axons are far from perfect cylinders and more complexity can be added by considering complex axonal membrane, myelin sheath surrounding axons, inside structure of axons (neurofilament and microtubules). Other

possibilities to consider are the water exchange between different compartments due to the porous nature of tissue (fast and slow exchange) [44, 45].

Nevertheless, the principle source of the diffusion anisotropy is due to axonal bundles, which can be modulated by the myelin content [5]. All diffusion models described in this thesis assume the simplest model of white matter described in the paragraph above.

1.3   ESTIMATION OF DIFFUSION USING MRI

Diffusion MRI can be used to estimate complex diffusion patterns in biological tissue invivo. These diffusion processes in biological tissue can be mathematically described as a probability density function (PDF) of the displacement of water molecules, also known as an ensemble average propagator (EAP) [46, 47]. The EAP can be directly estimated using MRI by a diffusion sensitive pulse gradient. Diffusion weighted MR images acquired from the scanner have a Fourier relationship with the EAP [48, 49]. If $P_{voxel}(\vec{\mathbf{R}}, \Delta)$ represents the probability density function of the displacement of water molecules in δ time [50-52] in a voxel, then the diffusion signal $S_{voxel}(\vec{\mathbf{q}})$ is given by,

$$\frac{S_{voxel}(\vec{\mathbf{q}})}{S_{voxel}(0)} = E_{voxel}(\vec{\mathbf{q}}) = \int_{\mathbb{R}^3} P_{voxel}(\vec{\mathbf{R}}, \Delta)\, e^{2\pi \vec{\mathbf{q}} \cdot \vec{\mathbf{R}}}\, \mathrm{d}\vec{\mathbf{R}} \qquad (1.9)$$

or,

$$P_{voxel}(\vec{\mathbf{R}}, \Delta) = \int_{\mathbb{R}^3} E_{voxel}(\vec{\mathbf{q}})\, e^{-2\pi \vec{\mathbf{q}} \cdot \vec{\mathbf{R}}}\, \mathrm{d}\vec{\mathbf{q}} \qquad (1.10)$$

where,

$$E_{voxel}(\vec{\mathbf{q}}) = \frac{S_{voxel}(\vec{\mathbf{q}})}{S_{voxel}(0)}$$

and

$$\vec{\mathbf{q}} = \frac{\gamma\vec{\mathbf{G}}\delta}{2\pi}, b = \|q\|^2 (\Delta - \frac{\delta}{3})$$
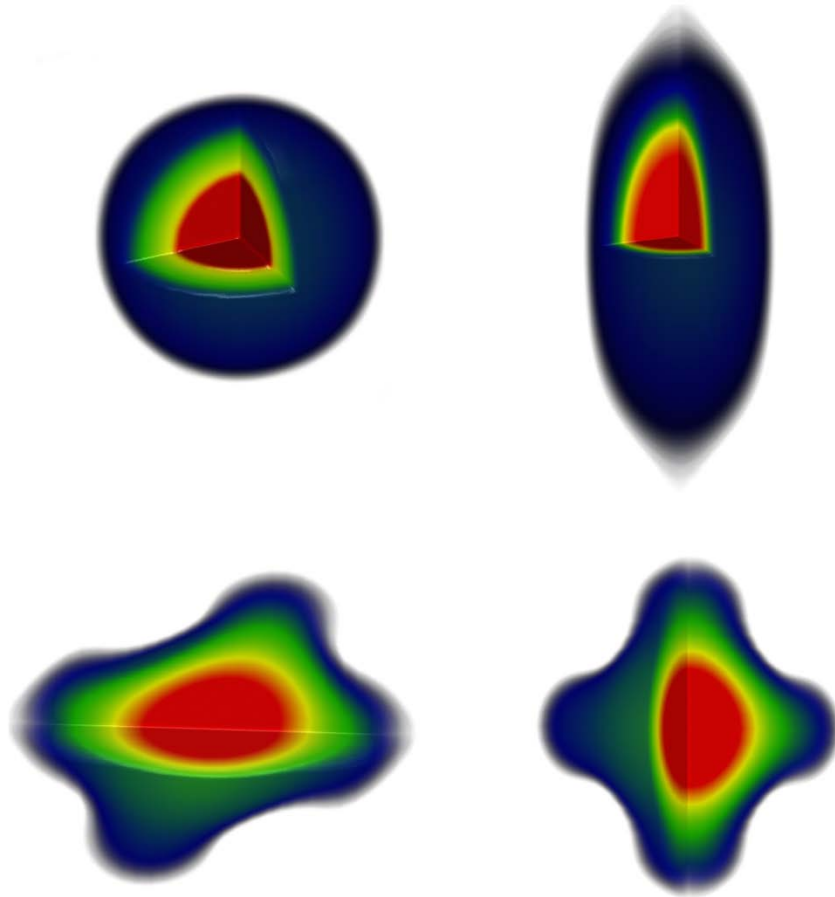
Figure 4. Volume rendering of the EAP. Four different types of diffusion patterns are used to illustrate the corresponding microstructure of tissue type. A) Isotropic diffusion with equal probability in all directions. B) Elliptic diffusion with large probability values in one direction. C) and D) Complex diffusion patterns due to crossing of fiber populations at 60° and 90° respectively

where $\vec{\mathbf{R}}$ is the displacement vector inside the voxel, $\vec{\mathbf{G}}$ is the diffusion gradient, γ is the gyro-magnetic constant for water and δ and Δ are duration and separation of the diffusion weighted gradient respectively. $P_{voxel}(\vec{\mathbf{R}}, \Delta)$ is a three dimensional scalar-valued function within voxel. Globally, $P_{voxel}(\vec{\mathbf{R}}, \Delta)$ is a function of voxel position and therefore can be considered as a six dimensional scalar valued function. To accurately estimate $P_{voxel}(\vec{\mathbf{R}}, \Delta)$, different q-space sampling techniques are used.

1.3.1 Q-Space Imaging

Equation 1.9 describes the relationship between q-space (diffusion weighted images) and the probability density function of displacement of water molecules, $P_{voxel}(\vec{\mathbf{R}}, \Delta)$ (see Figure 4). The accuracy of estimating $P_{voxel}(\vec{\mathbf{R}}, \Delta)$ depends upon the q-space sampling scheme and the diffusion model used to estimate $P_{voxel}(\vec{\mathbf{R}}, \Delta)$. Typically a diffusion model estimates the projection of $P_{voxel}(\vec{\mathbf{R}}, \Delta)$ onto a unit sphere (for details see section 1.4) known as the orientation distribution function.

Many sampling techniques have been suggested in the literature [48, 53, 54]. The most commonly used technique is to sample gradient directions uniformly on a sphere with constant b-value (typically $b = 1000\ s/mm^2$) to estimate ODF directly from DWIs. Gradient directions must be distributed uniformly to avoid the bias in the estimation of the direction of the underlying fiber population [55, 56]. Parametric modeling of $P_{voxel}(\vec{\mathbf{R}}, \Delta)$ (or ODF), for example, diffusion tensor imaging (see chapter two), requires the same set of diffusion gradients. Typically for such

modeling techniques the b-value is fixed to 900-1500 s/mm^2 and a minimum of six gradient directions are sampled [57].

Tuch [58, 59], Tournier [37, 38] and others have suggested high angular sampling on the unit sphere to model diffusion non-parametrically. High angular resolution diffusion imaging (HARDI) uses a large set of uniform gradient directions on a unit sphere with a fixed b-value, also called single shell sampling, to estimate the diffusion oriented distribution function (see next section for details). Typically 64-256 gradient directions are acquired for these types of schemes. Q-ball imaging [58, 60, 61] and constrained spherical deconvolution [37, 38] are examples of non-parametric models that use single shell techniques to model orientation features of diffusion.

Wedeen et al [48, 49] suggested a lattice sampling of q-space to estimate $P_{voxel}(\vec{\mathbf{R}}, \Delta)$ by performing the Fourier transform using equation 1.9. This technique samples q-space more densely than single-shell sampling to estimate $P_{voxel}(\vec{\mathbf{R}}, \Delta)$ but requires longer scan time to acquire the samples. Typically 256-515 gradient directions are acquired for this type of scheme. Diffusion Spectrum Imaging [48] (DSI) and Generalized Q-sampling Imaging [36] (GQI) are used to estimate $P_{voxel}(\vec{\mathbf{R}}, \Delta)$ from a lattice of q-space samples

Another alternative is multi-shell sampling in which multiple single shell schemes with different b-values are used to sample q-space [53, 54, 62]. Typically 3 to 5 b-values with 32-256 gradient directions for each shell are used. These types of sampling techniques can be used in DSI, CSD or Q-ball imaging.

1.4   THE ORIENTED DISTRIBUTION FUNCTION

The probability distribution function $P_{voxel}(\vec{\mathbf{R}}, \Delta)$ is a three dimensional function in a voxel. Volume rendering of $P_{voxel}(\vec{\mathbf{R}}, \Delta)$ can reveal the direction of the fiber population of the underlying tissue. The primary goal of diffusion MRI is to estimate the anisotropy from the EAP which is due to fiber structure and the geometrical properties of the underlying white matter tissue. The EAP can be modeled using advanced mathematical diffusion models that can be helpful to estimate fiber pathways. These fiber pathways represent the underlying axon bundles. Diffusion MRI does not directly image axons, but rather provides a probabilistic model for diffusion processes of water molecules in the axon bundle (see Figure 5).

To extract geometrical information about micro-tissue in the voxel, $P_{voxel}(\vec{\mathbf{R}}, \Delta)$ is radially projected on a unit sphere and is called the Oriented Distribution Function (ODF). There are multiple definitions of ODFs found in the literature, one of the most commonly used is the one proposed by Tuch et. al. [58, 59]

In the Tuch definition the probability distribution function $P_{voxel}(\vec{\mathbf{R}}, \Delta)$ is a scalar-valued function defined in 3D space:

$$P : \mathbb{R}^3 \to \mathbb{R}$$
$$P(\vec{\mathbf{R}}, \Delta) = P(\Delta x, \Delta y, \Delta z, \Delta)$$

ODFs are real scalar-valued functions defined on unit sphere $\mathcal{S}^2$:

$$\psi(\hat{u}) : \mathcal{S}^2 \to \mathbb{R}$$

ODFs are radial projections of the probability distribution function. They can be estimated by radially integrating,

$$\psi_{voxel}(\hat{u}) = \int_0^\infty P_{voxel}(R\hat{u}, \Delta)\, dR \qquad (1.11)$$

where $\vec{R} = R\,\hat{u}$ and $\mathcal{S}^2$ is a unit sphere and $\hat{u}$ are unit vectors on sphere $\mathcal{S}^2$.
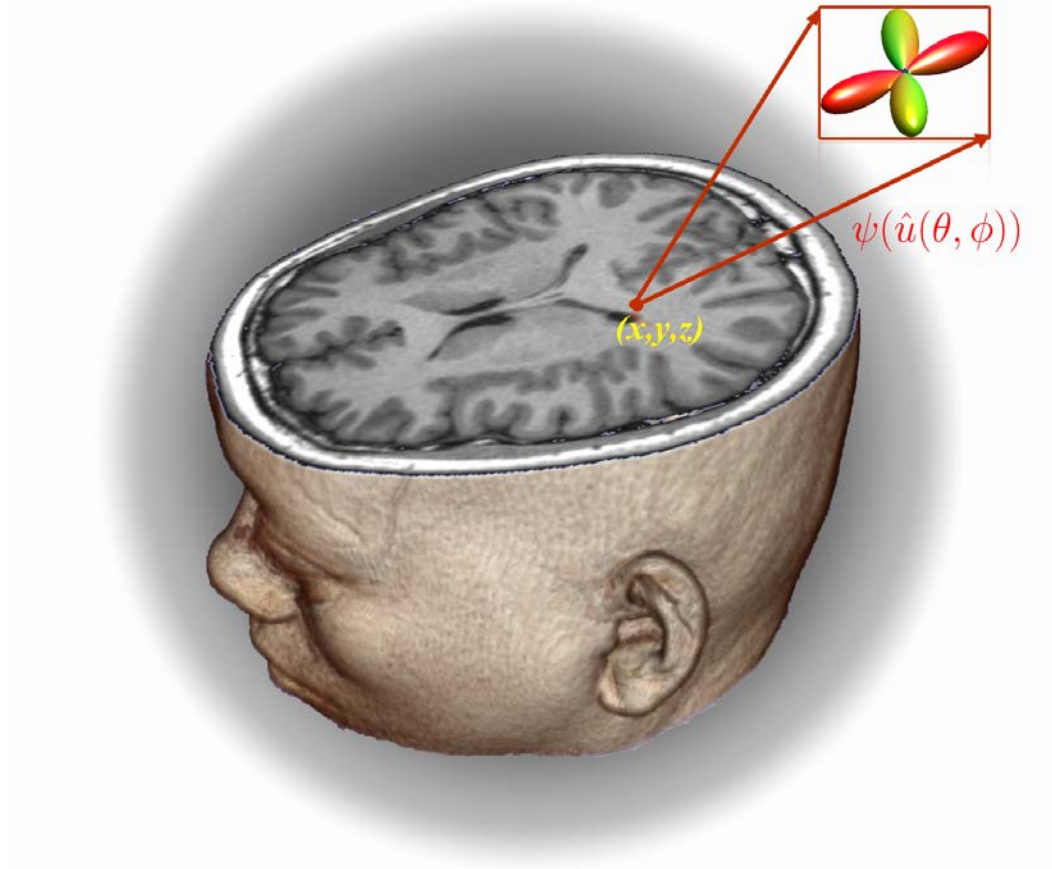
Figure 5. Surface rendering of an axial slice of human brain illustrating estimation of the Orientation

Distribution Function (ODF) for each voxel

This definition of the ODF does not include the determinant of the Jacobian term while converting from a Cartesian to a spherical coordinate system. The Jacobian term, R^2, can be added into the integral to get an ODF that is a true probability density function [63-65].

$$\psi_{voxel}(\hat{u}) = \int_0^\infty R^2\, P_{voxel}(R\hat{u}, \Delta)\, dR \qquad (1.12)$$

Values of an ODF projected onto a sphere represent the anisotropy of diffusion in that particular direction. Local maxima of ODFs on a unit sphere are taken to correspond to the underlying fiber population. These principal diffusion directions (ODF maxima) are further used in fiber tracking to estimate the underlying white matter axonal bundle.
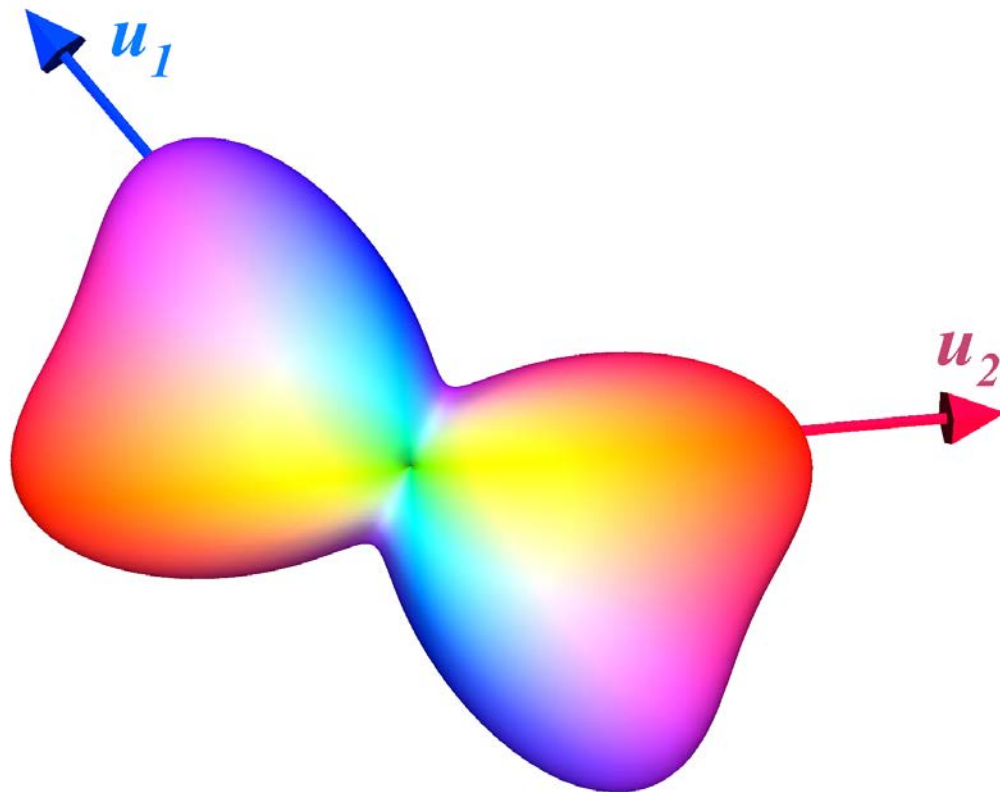
Figure 6. ODF peaks at maxima u_1 and u_2

The shape of the ODF in a particular voxel can be used to classify tissue types. A spherical shaped ODF represents a voxel containing pure CSF or grey matter, and a peanut-shaped ODF represents a voxel with a single fiber population. More complex ODF shapes with multiple peaks represent multiple fiber populations with crossing and kissing etc. (see Figure 6).

ODFs estimated from PDFs are also called diffusion ODFs (dODF) as they represent the diffusion profile of the tissue as opposed to the fiber profile of the tissue. Descoteaux el al proposed relationship between diffusion ODF and fiber ODF using Q-Ball Imaging techniques. Further, Tournier et al [37, 38] proposed a relationship between the diffusion ODF and the corresponding fiber ODF assuming fiber response function from single fiber population, which is taken to align with the underlying fiber population. Diffusion ODFs are the convolution of single fiber response with the fiber ODF. The underlying fiber population (fiber ODF) can also be represented as a delta (δ) function of the sphere, called the fiber ODF (fODF). The fODF is estimated by solving the deconvolution problem as proposed in [37, 38].

Chapters two and three will present a detailed description of the estimation of the fiber ODF using various diffusion modeling techniques.

1.5   LIMITATION OF FRACTIONAL ANISOTROPY AND DIFFUSION TENSOR IMAGING

Diffusion MRI is an advanced imaging technique that can be used non-invasively to measure the water diffusion processes in the tissue microstructure [50, 52]. By modeling both the amount of anisotropic diffusion as well as orientation information, structural connectivity can be established between different functional regions in the living human brain [66]. ODFs provide geometrical information such as fiber orientation in voxels but it can also be used to derive anisotropic volume maps to quantify axonal volume. The goal is a quantitative measurement of structural connectivity that is also anatomically interpretable. Currently, the most frequent metric

17

used in the literature to describe anisotropy (and hence structural connectivity) is fractional anisotropy (FA) [67-69]. If the goal is to measure the within axon water in order to quantify the amount of connection (e.g, summed cross sectional area of the axons making up the tract), FA is a confounded metric. This is due to its insensitivity to direction (orientation) and inaccurate modeling of diffusion in regions of fiber crossing [60, 61]. FA does not represent any real anatomical unit, such as the volume of axons. Edema represents another confounding factor. As the isotropic water increases, FA decreases, even when the cross sectional area of the axons is preserved. In TBI, edema is often a transient response. One would not want to falsely conclude that the fiber tracts are damaged based on an FA measurement when what had actually occurred is only a temporary increase in extra-cellular content.

This thesis proposes a novel diffusion-based structural connectivity metric called directional Axonal Volume (dAV) which relies on advanced acquisition techniques such as diffusion spectrum imaging (DSI) [48], and a novel method to map this metric on to fiber tracts. In contrast to metrics such as FA, dAV attempts to estimate a physical property of tissue; anisotropic water content. DAV is a fiber tract based metric, which quantifies the amount of anisotropic water content from intra-cellular water in axons, and can be projected along the fiber tracts for between-group comparisons. The proposed framework for the quantification of anisotropy is theoretically robust to fluctuations in axonal volume due to fiber crossings. Note that the three novel techniques proposed in this thesis do not depend on each other: alternate reconstruction method such as generalized q-sampling imaging (GQI [36]) can be used to compute dAV; and alternate volume metrics such as generalized fractional anisotropy or quantitative anisotropy [36] can be mapped to fiber tracts with the mapping methods proposed in chapter four.

18

1.6   VALIDATION METHODS

Various diffusion reconstruction models and derived anisotropic metrics are used to analyze diffusion images. Some of these metrics are statistical summaries of anisotropy of diffusion in a voxel and others may relate to the physical properties of the underlying tissue. Validation of these methods and related anisotropic metrics can establish mathematical accuracy and thus enable widespread use in clinical settings. Different types of phantoms are used in MR Imaging for quality assurance [70-73]. There are recent developments to create phantoms to test diffusion MRI based methods. These phantoms use solid or hollow fibers (to simulate axons) with different geometrical configurations [70, 74, 75]. In this thesis we are using a new textile based anisotropic phantom provided by an external firm (Psychology Software Tools, Inc) [76]. It will provide the ground truth measurement of restricted and hindered water in an empirical textile water phantom for diffusion imaging. Chapter five tests three hypotheses in the phantom based validation of the work presented in chapters two, three, and four.

1.7   CONCLUSIONS

Processing of diffusion MRI requires multiple steps including the choice of MR image acquisition, modeling and remediation of noise and distortion, diffusion modeling, fiber tracking and quantification of anisotropic metrics. All of these steps are dependent on each other and the choice of one step can affect the whole pipeline. This thesis work addresses diffusion modeling and quantification of fiber tracks. Chapter two gives an overview of key diffusion models and introduces a novel reconstruction method by combining Generalized Q-sampling Imaging [36]

(GQI) and Constrained Spherical Deconvolution [37, 38] (CSD) methods. Chapter three describes the deconvolution methods in ODF space for estimation of the fiber ODF. It also shows applications of this method in fiber tracking and visualization of sub-cortical regions in the human brain. Chapter four presents a framework to estimate diffusion anisotropy on fiber tracts, called direction axonal volume (dAV). It uses the ODF to map anisotropic metrics along the fiber tracks. Chapter five uses a textile based anisotropic phantom to validated diffusion models and the anisotropic metrics, dAV and NODDI [39].

2.0   RECONSTRUCTION OF DIFFUSION MRI

This chapter will present different diffusion modeling techniques. Diffusion models can be broadly categorized into parametric and non-parametric techniques. Section 2.3 describes the most popular parametric diffusion imaging technique, diffusion tensor imaging and its extensions, multi-tensor and the CHARMED model. Section 2.4 describes non-parametric modeling techniques including Q-ball imaging, diffusion spectrum imaging, and generalized q-sampling imaging (GQI). The use of the constrained spherical deconvolution (CSD) technique in Q-ball imaging will be discussed. Further applications of CSD are detailed in chapter three. Section 2.5 presents a novel reconstruction technique which combines spherical harmonics expansion with GQI to reconstruct the diffusion ODF from the diffusion dataset. This technique can thus take advantage of key benefits of both CSD and GQI. This technique can be used on diffusion imaging datasets acquired at multiple b-values. The analytical solution is presented for estimating the spherical harmonic coefficients of the diffusion ODFs and is demonstrated on simulated data. Use of this technique on human and phantom data is presented in chapters three and five.

2.1   INTRODUCTION

Over the past few decades there has been growing research in the area of modeling the diffusion of water molecules using diffusion weighted magnetic resonance imaging (diffusion MRI) [77-79]. Diffusion is a property of populations of water molecules as opposed to the individual molecules and is therefore described as an ensemble. The earliest approaches to diffusion imaging did not attempt to estimate the direction of diffusion, only the diffusion magnitude was estimated. The primary model for this is the apparent diffusion coefficient (ADC) [80-84]. The ensemble is modeled by three dimensional probability density functions (PDF) of the displacement of water molecules. These functions are also called ensemble diffusion propagators. The 3D PDF is radially projected on a unit sphere to create an oriented distribution function (ODF) model [58-61, 64, 65]. These models of diffusion are used to estimate the anisotropy of water in the underlying tissue and these estimates then delineate white matter structure in the tissue. Many of these modeling techniques depend on specific sampling of q-space during image acquisition [50]. For example Q-Ball imaging uses a constant b-value to sample q-space, while diffusion spectrum imaging uses a grid sampling.

The key goal of diffusion based MR imaging in all of these methods is to accurately model the diffusion of water in biological tissue. The choice of mathematical model will affect the accuracy of the estimates of both anisotropy and fiber orientation [50, 85]. There are two broad categories of mathematical models to describe PDFs. If the model has a known mathematical function it falls into the category of parametric models. For these models, model parameters must be fit at each voxel to characterize diffusion [77]. For example in diffusion tensor imaging (DTI) [68], PDFs are assumed to have an anisotropic Gaussian function. Six diffusion parameters are needed

to estimate the diffusion tensor [57]. On the other hand, non-parametric models such as diffusion spectrum imaging do not assume any analytical function [48, 49]. Instead, they directly estimate the PDF on a regular grid within each voxel. Non-parametric models for diffusion can also utilize basis functions to decompose a PDF into the linear sum of a known orthogonal basis set [85, 86]. For example, Q-ball imaging [58, 59, 87] uses spherical harmonics basis functions to represents PDFs. Non-parametric models have the advantage that they do not need to assume an analytical model that may be a poor fit to the data. But, they tend to capture more features of diffusion in a voxel and require more diffusion weighted images and hence more scanning time. The reconstruction model proposed below is a non-parametric model and attempts to improve upon the accuracy of the GQI [36] model.

2.2   ESTIMATION OF DIFFUSION MAGNITUDE

Diffusion in white matter tissue can be sensitized using a Pulsed Gradient Spin Echo (PGSE) sequence [88]. Contrast in these diffusion-weighted images (DWI) depends on the strength of pulse gradient and direction. The diffusion signal in a voxel is an average of diffusion in both intra- and extra-cellular tissue [41]. The diffusivity of water inside different tissue types is used as a contrast mechanism to differentiate tissue. A DWI technique to estimate diffusion magnitude, Apparent Diffusion Coefficient (ADC) modeling, was introduced by Moseley et al [89]. It uses multiple diffusion weighted images to estimate total diffusion, anisotropic and isotropic combined, but no diffusion direction, in the underlying tissue. ADC is estimated by solving,

$$\frac{S(b,\mathbf{g})}{S_0} = \exp\left(-4\pi^2\tau \left\|\vec{\mathbf{q}}\right\|^2 D\right) = \exp\left(-bD\right) \tag{2.1}$$

The ADC can be estimated with very few diffusion images. Mullins et al [90] shows the clinical usefulness of ADC over conventional MR imaging and CT. ADC scans have been successfully used in clinical research applications where it is useful to simply identify areas of reduced diffusion [91, 92]. For example they are used to distinguish between ischemic and healthy tissue in stroke patients. In 691 patients Mullins et al found that mean ADC has substantially better accuracy than T1/T2/T2* images in diagnosing stroke in its early period (less than 12 hours) [90, 93].

ADC imaging continues to be used in applications that only need to measure total diffusion magnitude. However the use of more sophisticated parametric and non-parametric models gives the ability to separate the anisotropic component of diffusion and accurately measure diffusion direction [48, 58, 68, 79]. Metrics derived from these models are the basis of more advanced applications of diffusion imaging [11, 67, 74, 94, 95]. Modeling the diffusion direction in a voxel requires more diffusion-weighted images with different gradient directions and gradient strength. Diffusion models can provide a) geometric properties of underlying tissue and b) anisotropic/isotropic water content [42, 43, 48, 49]. Peaks of ODFs derived from diffusion data set are used to estimate the direction of fiber populations within a voxel. These principal diffusion directions can then be used to create white matter fiber bundles in the human brain in the process of tractography [96].

2.3 PARAMETRIC MODELS OF DIFFUSION

2.3.1 Diffusion Tensor Imaging

Diffusion Tensor Imaging (DTI) is one of the original methods in the literature to model the diffusion propagator as proposed by Peter Basser, et al [68]. The key assumption in Diffusion Tensor Imaging is that diffusion in microstructure can be modeled as a 3D Gaussian function. Gaussian diffusion is captured by a second order tensor (3×3 positive definite symmetric matrix) [77, 97, 98]. The diffusion tensor can be related to Einstein's equation for diffusivity (equation 1.8 from chapter one). It is a generalization of the one dimensional diffusion in equation 1.8 to three dimensions:

$$\mathbf{D} = \begin{pmatrix} D_{xx} & D_{xy} & D_{xz} \\ D_{yx} & D_{yy} & D_{yz} \\ D_{zx} & D_{zy} & D_{zz} \end{pmatrix} = \frac{1}{6\tau} \langle \mathbf{R} \cdot \mathbf{R}^T \rangle \qquad (2.2)$$
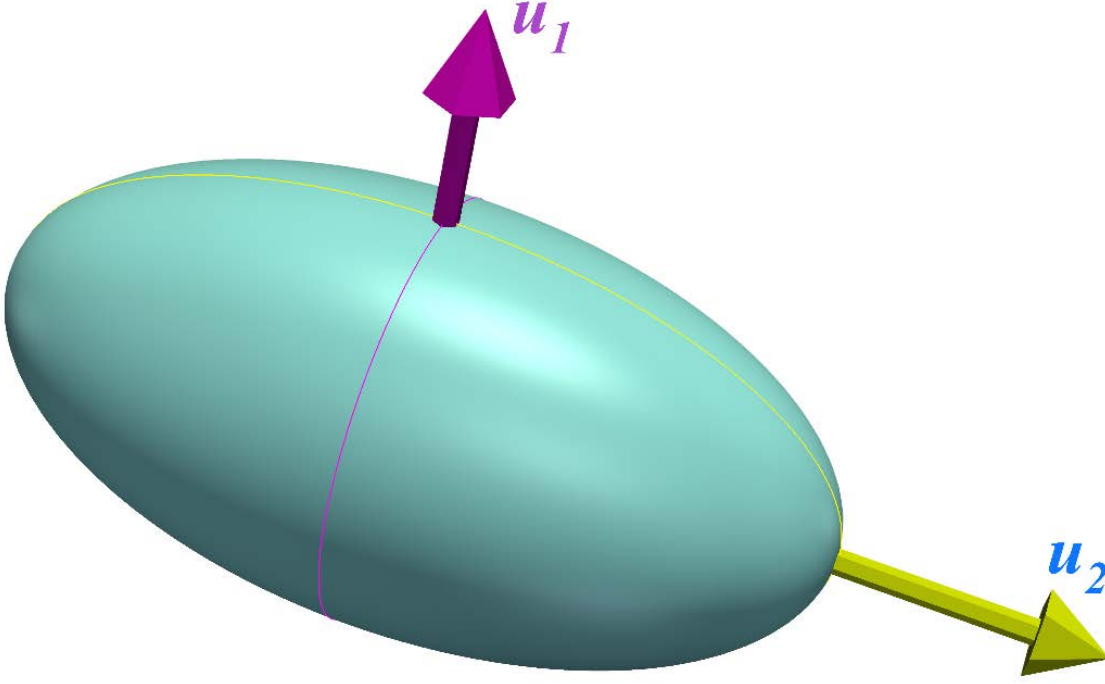
Figure 7. Diffusion tensor can be geometrically represented as an ellipsoid. Eigen value decomposition of the tensor provides principal diffusion direction (u_1, u_2, u_3).

By substituting equation 2.2 for the Einstein equation into equation 1.9, we can represent the relationship between diffusion weighted images and the diffusion tensor:

$$E(\vec{\mathbf{q}}) = \frac{S(b, \mathbf{g})}{S_0} = \exp\left(-b\, \mathbf{g}^T \cdot \mathbf{D} \cdot \mathbf{g}\right) \tag{2.3}$$

where $S(b, \mathbf{g})$ is a diffusion weighted image with b as diffusion weighting factor and $\mathbf{g}$ as gradient direction, $\vec{\mathbf{q}} = \dfrac{\gamma \vec{\mathbf{G}} \delta}{2\pi}$ is the q-vector, $\vec{\mathbf{G}}$ is the diffusion gradient, γ is the gyro-magnetic constant for water, δ and Δ are duration and separation of the diffusion weighted gradient respectively, $b = 4\pi^2 \left\|\vec{\mathbf{q}}\right\|^2 (\Delta - \dfrac{\delta}{3})$, S_0 is the diffusion unweighted image and $\mathbf{D}$ is a diffusion tensor of second order as described above. The probability density function of net

displacement of water molecules $P(\vec{\mathbf{r}})$ can then be estimated by taking the Fourier transform ($\mathcal{F}$) of equation 2.3

$$P(\vec{\mathbf{r}}) = \mathcal{F}(E(\vec{\mathbf{q}})) = \frac{1}{\sqrt{(4\pi\tau)^3 |\mathbf{D}|}} \exp\left(-\frac{\vec{\mathbf{r}}^T \mathbf{D}^{-1} \vec{\mathbf{r}}}{4\tau} \right) \qquad (2.4)$$

A minimum of seven diffusion images (six diffusion weighted and one un-weighted) are needed to estimate the six parameters of diffusion tensor $\mathbf{H} = (D_{xx}, D_{xy}, D_{xz}, D_{yy}, D_{yz}, D_{zz})$. Note $\mathbf{D}$ is a symmetric positive definite matrix so $D_{xy} = D_{yx}, D_{yz} = D_{zy}$ and $D_{xz} = D_{zx}$. Given N diffusion weighted signals $\{S(b_i, \mathbf{g}_i)\}_{i=1\cdots N}$, estimation of the diffusion tensor can be written as a system of linear equations as follows [77, 97, 98]:

$$P(\vec{\mathbf{r}}) = \mathcal{F}(E(\vec{\mathbf{q}})) = \frac{1}{\sqrt{(4\pi\tau)^3 |\mathbf{D}|}} \exp\left(-\frac{\vec{\mathbf{r}}^T \mathbf{D}^{-1} \vec{\mathbf{r}}}{4\tau} \right) \qquad (2.5)$$

$$-\log\left(\frac{S(b,\mathbf{g})}{S_0} \right) = b_i g_i^T \mathbf{D} g_i = \mathbf{W} \cdot \mathbf{H}$$

Where the ith row of matrix $\mathbf{W}$ is given by,

$$\mathbf{W}_i^T = \left(b_i g_i^x g_i^x, b_i g_i^x g_i^y, b_i g_i^x g_i^z, b_i g_i^y g_i^y, b_i g_i^y g_i^z, b_i g_i^z g_i^z \right), \mathbf{g}_i = \left(g_i^x, g_i^y, g_i^z \right) \qquad (2.6)$$

In equation 2.5, $\mathbf{H}$ can be solved using least a square estimation method [98].

$$\mathbf{H} = (\mathbf{W}\,\mathbf{W}^T)^{-1}\,\mathbf{W}\,\mathbf{E} \qquad (2.7)$$

Where,

$$\mathbf{W} = \begin{bmatrix} \mathbf{W}_1 \\ \mathbf{W}_2 \\ \vdots \\ \mathbf{W}_N \end{bmatrix} = \begin{bmatrix} b_1 g_1^x g_1^x & b_1 g_1^x g_1^y & b_1 g_1^x g_1^z & b_1 g_1^y g_1^y & b_1 g_1^y g_1^z & b_1 g_1^z g_1^z \\ b_2 g_2^x g_2^x & b_2 g_2^x g_2^y & b_2 g_2^x g_2^z & b_2 g_2^y g_2^y & b_2 g_2^y g_2^z & b_2 g_2^z g_2^z \\ \vdots & \vdots & \vdots & \vdots & \vdots & \vdots \\ b_N g_N^x g_N^x & b_N g_N^x g_N^y & b_N g_N^x g_N^z & b_N g_N^y g_N^y & b_N g_N^y g_N^z & b_N g_N^z g_N^z \end{bmatrix}$$

and

$$\mathbf{E} = \begin{bmatrix} -\log\left(\dfrac{S(b_1, \mathbf{g}_1)}{S_0} \right) \\ -\log\left(\dfrac{S(b_2, \mathbf{g}_2)}{S_0} \right) \\ \vdots \\ -\log\left(\dfrac{S(b_N, \mathbf{g}_N)}{S_0} \right) \end{bmatrix} \tag{2.8}$$

This is simplified formulation of the diffusion tensor model. For a full and detailed formulation see [68].

Once the diffusion tensor has been estimated, eigenvalue decomposition (EVD) (see Figure 7) of **D** can provide geometric and anisotropic information about the micro-structure of tissue [67, 77, 95]. The eigenvector or principal diffusion direction that is estimated using *EVD* (see Figure 8) is then taken to reflect the orientation of white matter tissue in the imaged voxel as follows [99].

$$\mathbf{D} = \sum_{i=1}^{3} \lambda_i \mathbf{v}_i \cdot \mathbf{v}_i^T \tag{2.9}$$
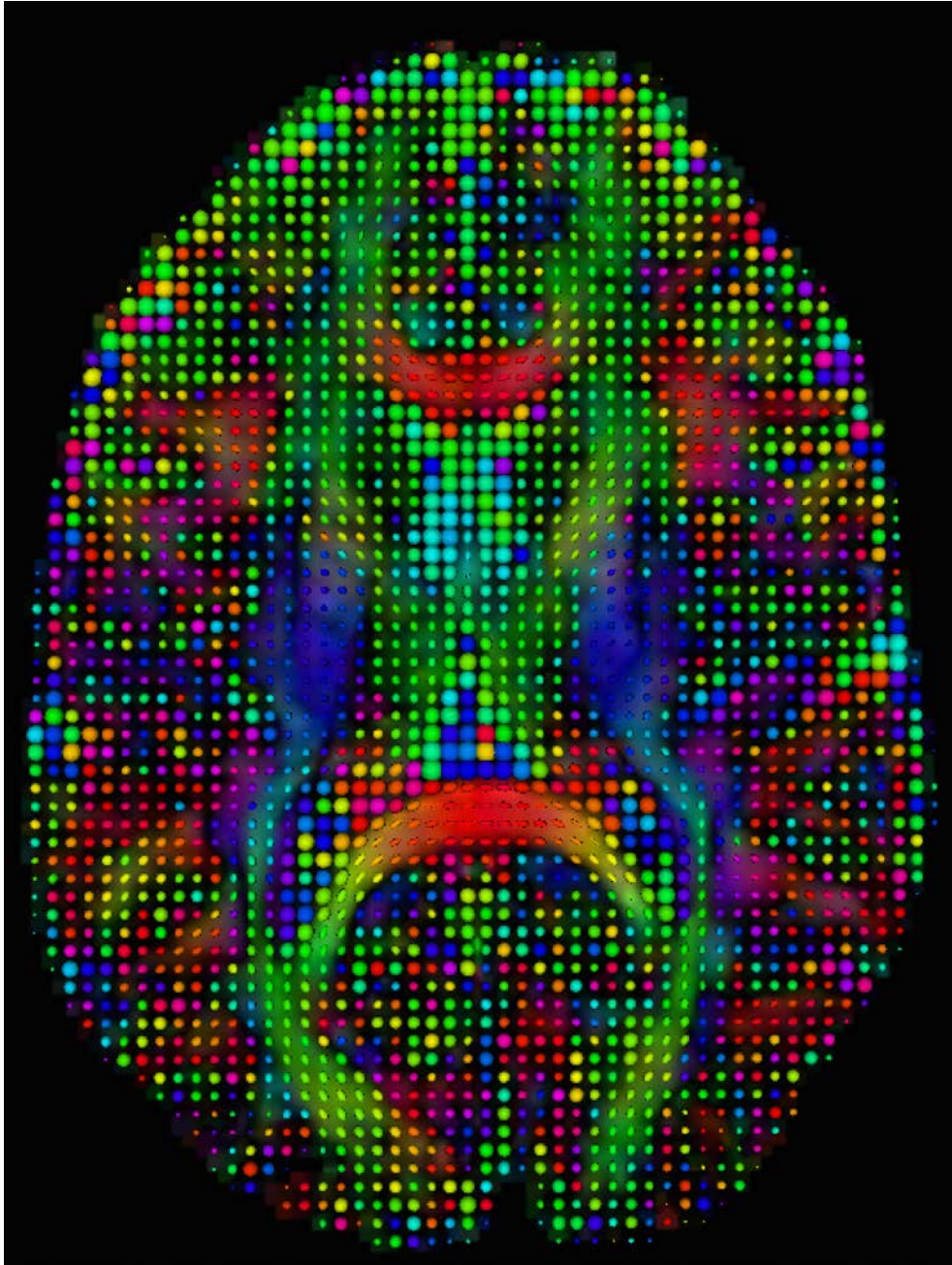
Figure 8. Visualization of the diffusion tensor in each voxel of an axial slice of a diffusion MRI scan. Voxels in areas with densely packed axons show an ellipsoidal tensor (corpus callosum) as opposed to spherical in regions of isotropic diffusion (cerebro spinal fluid (CSF)). Color in each voxel represents the orientation of the fiber (red color shows fiber oriented in a left-right (x-axis) direction, green for anterior-posterior (y-axis) and blue for inferior-superior (z-axis). In the case of isotropic diffusion i.e., non-determinant fiber orientation the voxel has a random color.

The principal eigenvector ($\mathbf{e}_1$) corresponding to the maximum eigenvalue ($\lambda_1 \geq \lambda_2 \geq \lambda_3$) is estimated for each voxel. Various scalar metrics are derived from eigenvalues and used to characterize the tissue anisotropy. The most commonly used metric to characterize white matter anisotropy is fractional anisotropy (*FA*) [67, 68, 95]. It is a scalar valued map whose values vary from 0.0 to 1.0. *FA* equal to 0.0 indicates isotropic diffusion (for example CSF) and *FA* equal to 1.0 indicates pure anisotropic diffusion (for example Corpus Callosum, see Figure 8).

$$\mathbf{FA} = \sqrt{\frac{3\left((\lambda_1 - \bar{\lambda})^2 + (\lambda_2 - \bar{\lambda})^3 + (\lambda_3 - \bar{\lambda})^2\right)}{2\left(\lambda_1^2 + \lambda_2^2 + \lambda_3^2\right)}} \qquad (2.10)$$

where $\bar{\lambda}$ is mean diffusivity i.e., $\bar{\lambda} = \dfrac{\lambda_1 + \lambda_2 + \lambda_3}{3}$.
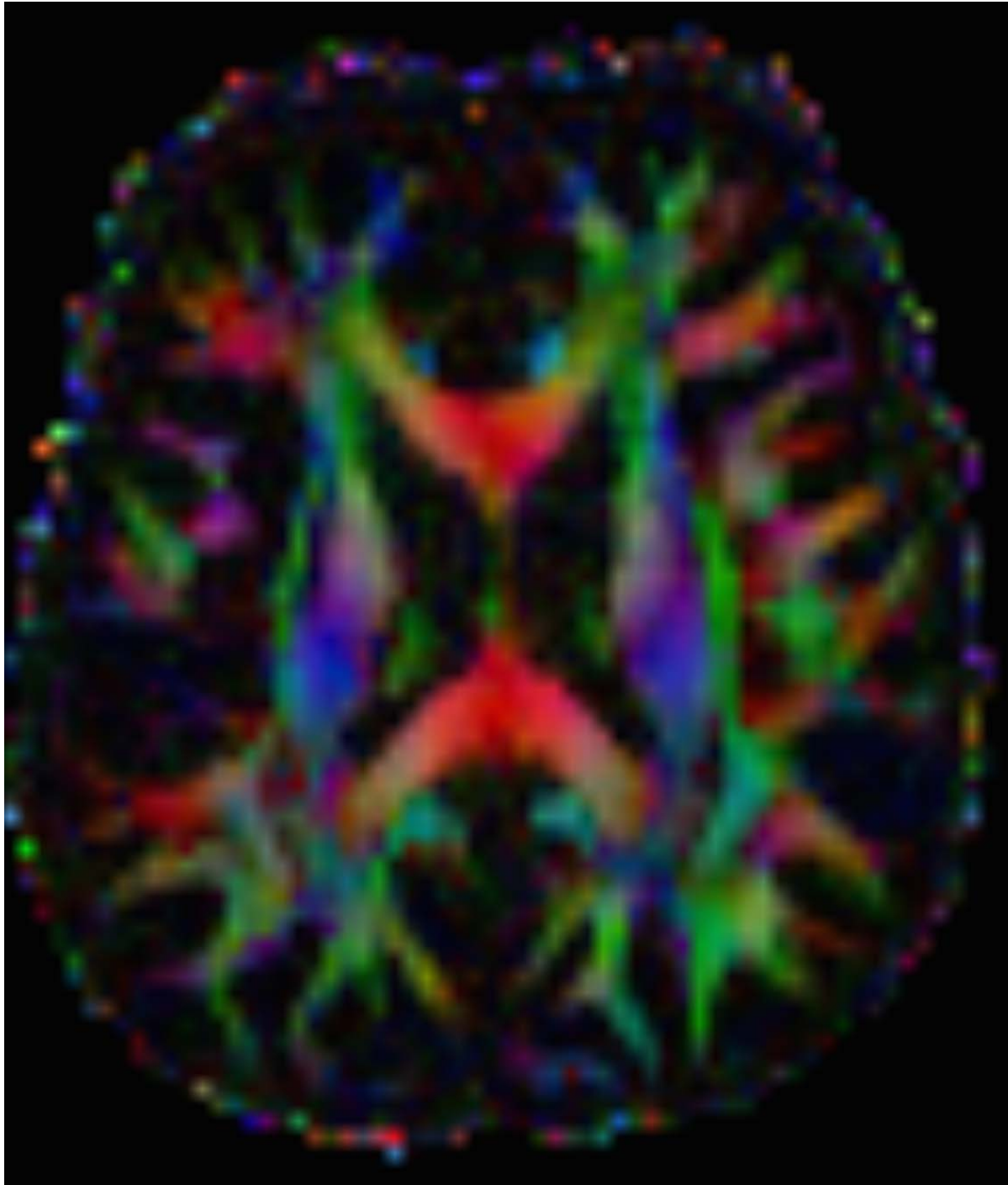
Figure 9. Direction encoded color (DEC) map of an axial slice from a diffusion MRI scan. Red color shows fibers oriented in the left-right (x-axis) direction, green for anterior-posterior (y-axis) and blue for inferior-superior (z-axis). For example, Corpus Callosum is colored as red, optic radiation as green and cortico-spinal tracts as blue.

A number of related metrics can also be derived from the diffusion tensor [67, 95]. Standard metrics such as radial and mean diffusivity will be discussed in chapter four. Westin et al [100] proposed several metrics based on the diffusion tensor to characterize the type of diffusion in different tissue types (see Figure 9).

DTI based reconstruction of diffusion requires a simple acquisition scheme (a minimum of six gradient directions) with a very short scanning time (typically 3-6 minutes). As with the ADC map, short scanning time and fast reconstruction method makes DTI very popular in clinical applications such neurosurgery [4], epilepsy [101, 102], multiple sclerosis (MS) [103-105], amyotrophic lateral sclerosis (ALS) [17], and Huntington's disease (HD) [14, 16, 106].

The diffusion tensor model and its parameter estimation using ordinary least squares (OLS) is a simple and computationally inexpensive method. However, there are three problems in this solution. First, the OLS solution does not guarantee a positive definite matrix. These are modified versions of the least squares methods that address this issue. For example, a weighted least squares method described ensures positive definiteness of diffusion tensor [68, 107]. Second, OLS implicitly models noise as Gaussian. An improvement is to explicitly choose a noise model. For example, one could model noise as Rician rather than Gaussian, which is a more appropriate model for diffusion MRI [108]. Third, in regions with complex geometry like fiber crossings a single diffusion tensor model cannot capture both fiber populations [58, 60, 61, 65, 67, 69]. There are two ways to model multiple fiber populations to address this issue. First, higher rank tensor models which capture multiple peaks and can resolve crossing issues are used [109, 110]. Second, multi-tensor based models, which are generalizations of diffusion tensor models can be used to address this problem [111-113]. The multi-tensor based reconstruction method uses a weighted linear sum of multiple anisotropic Gaussian functions to model multiple

32

fiber populations in each voxel. It can be used to resolve complex fiber structures such as crossings. However a limitation is that it requires a prior knowledge of how many fiber populations one wants to fit in a voxel [114].

For K-fiber populations,

$$E(\vec{\mathbf{q}}) = \frac{S(b,\mathbf{g})}{S_0} = \sum_{i=1}^{K} w_i \exp\left(-b\, \mathbf{g}^T \cdot \mathbf{D}_i \cdot \mathbf{g}\right) \tag{2.11}$$

where w_i are weights such that $\sum_{i=1}^{K} w_i = 1$ and $\mathbf{D}_i$ are tensors for the ith fiber (see Figure 10).
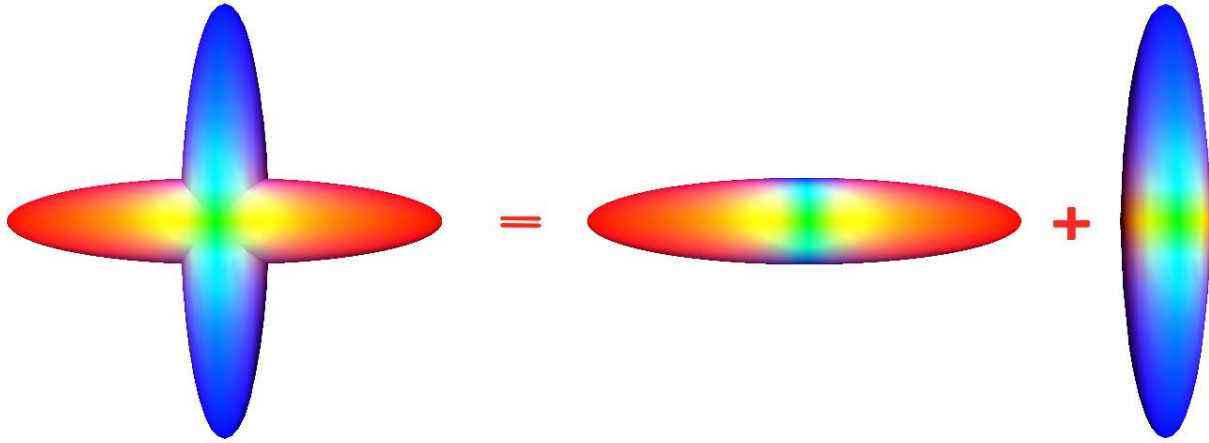
Figure 10. Multi Tensor modeling of a diffusion dataset. The diffusion signal can be modeled as a weighted sum of tensors.

Unlike DTI, multi-tensor modeling requires non-linear fitting. A minimization problem needs to be solved using a fast iterative solver like Levenberg [115] or Marquardt [116] minimization. It has been shown that the minimum of the above equation is ill posed because the solution for the w_i terms is conflated with the solution of the D_i terms [77, 97, 107, 117]. Adding more constraints on the diffusion tensor permits the minimization problem to be solved

[97, 108]. One such method is the Ball and Stick model proposed by Behrens [118, 119]. Although this method provides a robust solution to the minimization problem, it does not model non-Gaussian diffusion processes in the micro-structure of white matter tissue.

2.3.2 CHARMED Model of Diffusion

A significant extension of the diffusion tensor approach is to use a biophysically inspired parametric model that separately models intracellular and extracellular diffusion in a voxel. The CHARMED [41, 42] model characterizes diffusion in a voxel with multiple compartments, restricted and hindered. Intracellular water that has restricted diffusion (inside axons) does not follow Gaussian assumptions. Therefore it is modeled using a closed form analytical solution for diffusion inside a cylinder of known radius instead of a Gaussian. Extracellular water, that has hindered and isotropic diffusion, is modeled using the diffusion tensor models discussed in the previous section. Multiple hindered and restricted compartments are used for each fiber population.

In the CHARMED model each restricted and hindered compartment can be written as a product of radial and axial components of diffusion. Diffusion signal, E_r for the hindered compartment can be modeled as a product of radial ($E_{r,\parallel}$) and axial ($E_{r,\perp}$) compartment:

$$E_h(\vec{\mathbf{q}}, \Delta) = E_{h,\parallel}(\vec{\mathbf{q}}, \Delta) E_{h,\perp}(\vec{\mathbf{q}}, \Delta) \qquad (2.12)$$

where,

$$E_{h,\parallel}(\vec{\mathbf{q}}, \Delta) = \exp\left(-4\pi^2 \left\|\vec{\mathbf{q}}_{\parallel}\right\|^2 \left(\Delta - \frac{\delta}{3}\right) D_{\parallel}\right) \qquad (2.13)$$

and for restricted compartment also,

34

$$E_r(\vec{\mathbf{q}}, \Delta) = E_{r,\parallel}(\vec{\mathbf{q}}, \Delta) E_{r,\perp}(\vec{\mathbf{q}}, \Delta) \tag{2.14}$$

where,

$$E_{r,\parallel}(\vec{\mathbf{q}}, \Delta) = \exp\left(-4\pi^2 \left\| \vec{\mathbf{q}}_\parallel \right\|^2 \left(\Delta - \frac{\delta}{3} \right) D_\parallel \right) \tag{2.15}$$

$$E_{r,\perp}(\vec{\mathbf{q}}, \Delta) = \exp\left(-\left(\frac{4\pi^2 R^4 \left\| \vec{\mathbf{q}}_\perp \right\|^2}{D_\perp \tau} \right) \left(\frac{7}{96} \right) \left(2 - \frac{99R^2}{112 D_\perp \tau} \right) \right) \tag{2.16}$$

and,

$$\left\| \vec{\mathbf{q}}_\parallel \right\| = \left\| \vec{\mathbf{q}} \right\| \sqrt{1 - (\sin(\theta_q)\sin(\theta_N)\cos(\phi_q - \phi_N) + \cos(\theta_q)\cos(\theta_N))^2}$$

$$\left\| \vec{\mathbf{q}}_\perp \right\| = \left\| \vec{\mathbf{q}} \right\| \cdot | \sin(\theta_q)\sin(\theta_N)\cos(\phi_q - \phi_N) + \cos(\theta_q)\cos(\theta_N)) |$$

where, (θ_q, ϕ_q) is spherical coordinate of q-vector with azimuthal angle θ_q and polar angle ϕ_q. (θ_N, ϕ_N) is spherical coordinate of orientation of underlying microstructure with azimuthal angle θ_N and polar angle ϕ_N. θ_N and ϕ_N are unknown and estimated by solving equation 2.17.

Using the above equations 2.12 and 2.14, the diffusion signal can be modeled as a mixture of hindered and restricted compartments,

$$E(\vec{\mathbf{q}}, \Delta) = \sum_{i=1}^{K} (v_i E_r^i(\vec{\mathbf{q}}, \Delta)) + (1 - v_0) E_h(\vec{\mathbf{q}}, \Delta) \tag{2.17}$$

Equation 2.17 can be solved using non-linear optimization methods (e.g. Newton's method [120]). The volume fraction v_i of diffusion is estimated for each compartment (v_0 for hindered and $v_i, i = 1..K$ for restricted) along with the radius of the underlying fiber population.

The CHARMED model has the advantage that it models the underlying physical diffusion process in white matter. This permits it to estimate physical properties such as axon diameter and diffusivity. However, as with the multi-tensor models the number of fiber populations in a voxel must be specified. Another limitation of the CHARMED model is that it assumes that the diameters of all fibers within a single voxel are the same. AxCaliber [42] extends the CHARMED model to address multi-diameter fiber populations in a voxel.

2.4   NON-PARAMETRIC MODELS OF DIFFUSION

Non-parametric diffusion reconstruction techniques do not assume any mathematical form of the probability density function of displacement of molecules $P_{voxel}(\vec{\mathbf{R}}, \Delta)$. These models elucidate underlying fiber populations without any modeling constraints on its form. The following sections describe three non-parametric reconstruction methods: Q-Ball Imaging, Diffusion Spectrum Imaging, and Generalized Q-Sampling Imaging (GQI). It derives and discusses the novel reconstruction model developed in this thesis work. In non-parametric models diffusion is typically described using oriented distribution functions (ODFs) defined on a unit sphere. There are two type of ODF, the fiber ODF (fODF) which describes the distribution function of fibers and the diffusion ODF (dODF) which describes the distribution function of diffusing water molecules in a particular direction. ODFs are distribution function on the unit sphere. Any functions defined on a unit sphere can be usefully decomposed into spherical harmonics basis functions. Therefore, before describing the non-parametric models, the next section will outline the mathematics of spherical harmonic decomposition.

2.4.1 Spherical Harmonics

Spherical harmonic (SH) coefficients are estimated by decomposition of the ODF into a linear sum of spherical harmonic functions. Spherical harmonics are a well-known set of basis functions on a sphere [121]. Spherical harmonics are solutions of the Laplace equation $\Delta^2 u = 0$.

The Laplace equation in a spherical coordinate system $(u(r,\theta,\phi) = R(r)Y(\theta,\phi))$ can be written as:

$$\frac{1}{r^2}\frac{\partial u}{\partial r}\left(r^2\frac{\partial u}{\partial r}\right) + \frac{1}{r^2\sin\theta}\frac{\partial}{\partial\theta}\left(\sin\theta\frac{\partial u}{\partial\theta}\right) + \frac{1}{r^2\sin^2\theta}\frac{\partial^2 u}{\partial\phi^2} = 0 \qquad (2.18)$$

Substituting radius $r = 1$ for a unit sphere, $u(r,\theta,\phi) = Y(\theta,\phi)$, equation 2.18 can be rewritten as:

$$\frac{1}{Y}\frac{1}{\sin\theta}\frac{\partial}{\partial\theta}\left(\sin\theta\frac{\partial Y}{\partial\theta}\right) + \frac{1}{Y}\frac{1}{\sin^2\theta}\frac{\partial^2 Y}{\partial\phi^2} = -\lambda \qquad (2.19)$$

where λ is a real number and θ and ϕ are polar and azimuthal angles respectively.

The solution of equation 2.19 can be decomposed into functions of θ and ϕ as, $Y(\theta,\phi) = \Theta(\theta)\Phi(\phi)$. After substituting these into equation 2.19 one gets,

$$\lambda\sin^2\theta + \frac{\sin\theta}{\Theta(\theta)}\frac{d}{d\theta}\left[\sin\theta\frac{d\Theta}{d\theta}\right] = m^2 \qquad (2.20)$$

Above equation λ can take form $l(l+1)$ for $l > |m|$. Solving the above equation for a particular l and m gives:

$$Y_l^m(\theta,\phi) = \sqrt{\frac{2l+1}{4\pi}\frac{(l-m)!}{(l+m)!}}P_l^m(\cos\theta)e^{im\phi} \qquad (2.21)$$

Where P_l^m are the associated Legendre polynomials with degree l and order m and $\theta \in [0, \pi]$ and $\theta \in [0, 2\pi]$. Spherical harmonics of even order are used to decompose the ODF i.e., l is even for the analyses discussed in this thesis.

The SH framework outlined here will play a role in the Q-Ball and the proposed novel reconstruction technique. The use of SH in CSD will be discussed in chapter three.

2.4.2 Q-Ball Imaging

The idea behind q-ball imaging is to estimate the ODF directly from spherically sampled (with b = constant) diffusion weighted images in q-space. There are multiple definitions of the ODF found in the literature, with the most common one proposed by Tuch at el. Tuch [58, 59] proposed using the Funk Radon Transformation (FRT) to estimate the ODF

The FRT estimates the oriented distribution function at $\vec{\mathbf{u}}$ by integrating the diffusion signal on a unit 3D circle $\mathcal{U}_\perp$.

The FRT is defined as, for a given function $f(\vec{\mathbf{v}})$ defined on unit sphere $\mathcal{S}_2$,

$$f : \mathcal{S}_2 \to \mathbb{R}$$

Then,

$$\mathbf{FRT}\left[f(\vec{\mathbf{v}})\right](\vec{\mathbf{u}}) = \int_{\vec{\mathbf{v}} \in \mathcal{U}_\perp} f(\vec{\mathbf{v}}) d\vec{\mathbf{v}}$$

where $\mathcal{U}_\perp$ is set of vectors perpendicular to $\vec{\mathbf{u}}$.
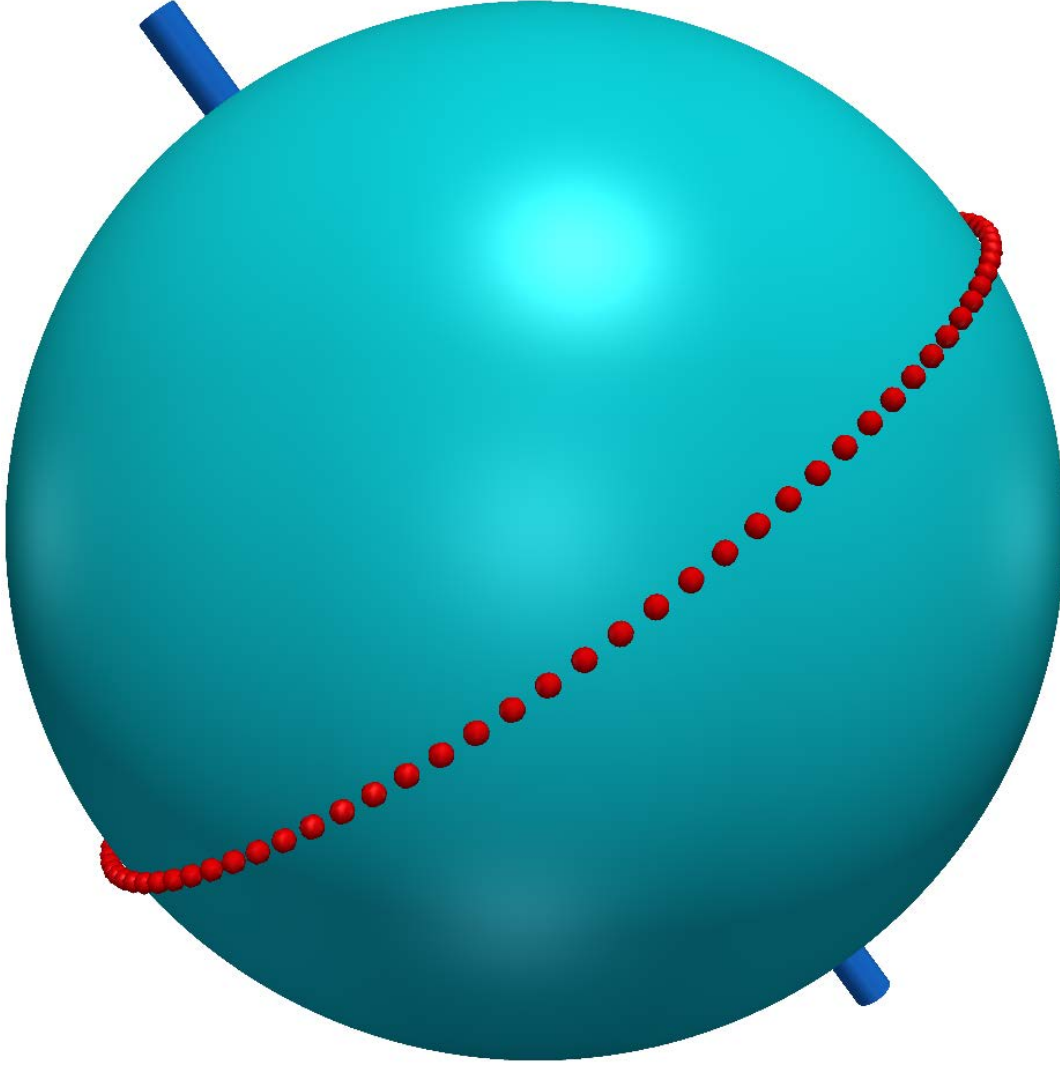
Figure 11. Funk-Radon Transformation (FRT) estimates the orientation distribution function (ODF) at $\vec{\mathbf{u}}$ by integrating the diffusion signal on a unit 3D circle $\mathcal{U}_\perp$.

Tuch et al [58, 59] showed that the relationship between ODF and the normalized signal

$E(\vec{\mathbf{q}}) = \dfrac{S(b, \mathbf{g})}{S_0}$ using FRT is,

$$\Phi(\vec{\mathbf{u}}) = \frac{1}{Z} \mathbf{FRT}(E(\vec{\mathbf{q}})(\vec{\mathbf{u}}, r)) \qquad (2.22)$$

where $Z = \left\| \Phi(\vec{\mathbf{u}}) \right\|$ is the normalization constant and r is the sampling radius.

The idea behind the FRT is that to estimate the ODF Φ at $\vec{\mathbf{u}}$, one needs to integrate $E(\vec{\mathbf{q}})$ on a unit 3D circle such that the plane of the circle is perpendicular to $\vec{\mathbf{u}}$ (see Figure 11). $E(\vec{\mathbf{q}})$ is interpolated to estimate the integral along the circle. Numerical schemes have been proposed by Tuch et al [58, 59] to estimate the ODF on discrete points on a unit sphere. The estimated ODF is then further used to calculate multiple principle diffusion directions in each voxel.

An analytical solution can be derived for diffusion weighted imaging data on a single shell using the FRT to estimate the spherical harmonic coefficients of the diffusion ODF [60, 61]. Analytical QBI represents the signal $E(\vec{\mathbf{q}}, \Delta)$ with a spherical harmonics basis (see Figure 12 and 13).

$$E(q_0\hat{\mathbf{u}}) = \sum_{l=0}^{L} \sum_{m=-l}^{l} c_{lm} Y_l^m(\hat{\mathbf{u}}(\theta, \phi)) \qquad (2.23)$$

where,

$$Y_l^m(\hat{\mathbf{u}}(\theta, \phi)) = \sqrt{\frac{2l+1}{4\pi} \frac{(l-m)!}{(l+m)!}} P_l^m(\cos\theta) e^{\imath m\phi}$$

$$(2.24)$$

For $k = 0, 2, 4, ..., l$ and $m = -k, ..., 0, ..., k$ let $j = j(k, m) = \dfrac{k^2 + k + 2}{2} + m$ then,

$$Y_j = \begin{cases} \sqrt{2} \cdot \mathrm{Re}(Y_k^m) & \text{if } -k \le m < 0 \\ Y_k^0 & \text{if } m = 0 \\ \sqrt{2} \cdot \mathrm{Im}(Y_k^m) & \text{if } 0 < m \le k \end{cases} \qquad (2.25)$$
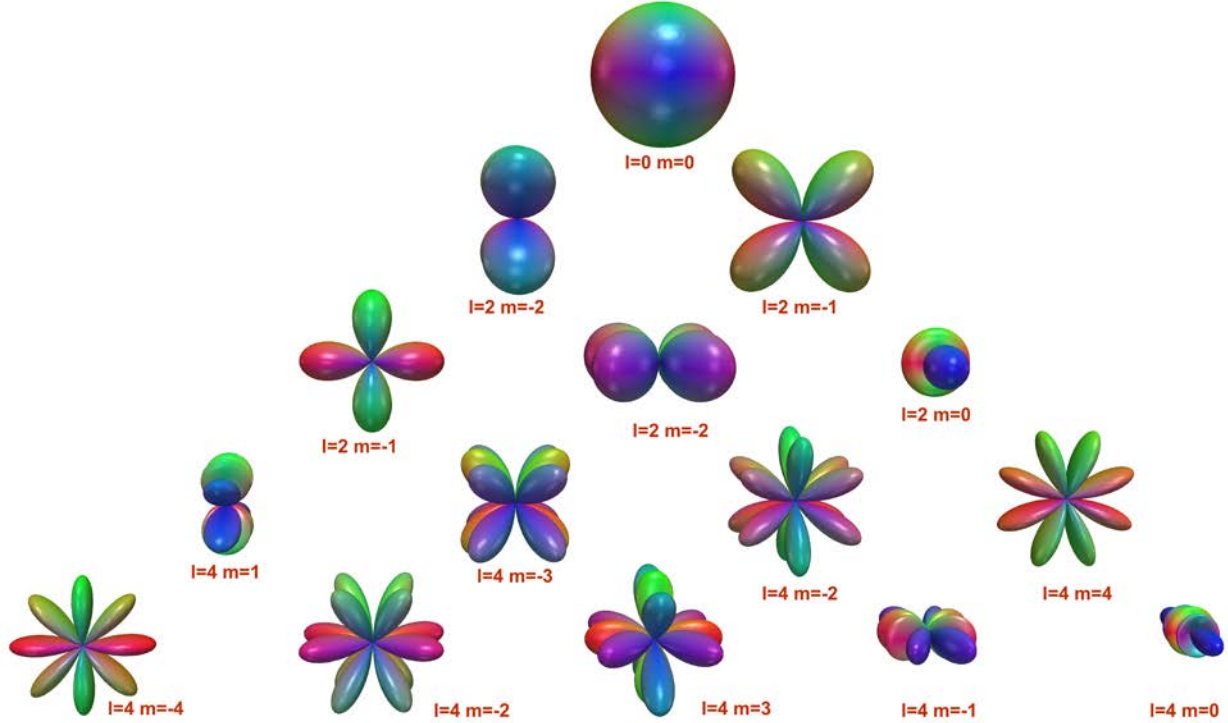
Figure 12. Spherical harmonic functions with different degree *m* and order *l*. These functions form an orthonormal basis for the unit sphere $\mathcal{S}_2$.

Therefore,

$$E(\theta_i, \phi_i) = E(q_0\hat{\mathbf{u}}) = \sum_{j=0}^{K} c_j Y_j(\theta_i, \phi_i) \tag{2.26}$$

Now using the Funk-Hecke theorem, the spherical harmonic coefficients of diffusion ODF can be estimated as:

$$E(\theta_i, \phi_i) = E(q_0\hat{\mathbf{u}}) = \frac{1}{Z} \sum_{j=0}^{K} 2\pi P_j(0) c_j Y_j(\theta_i, \phi_i) \tag{2.27}$$

where $\Phi(\theta_i, \phi_i)$ is ODF value at (θ_i, ϕ_i) and $P_j(0)$ is the Legendre polynomial of degree K evaluated at 0.

The above equation can be represented in discrete form with N gradient directions and spherical harmonics with maximum order L from equation 2.27 as follows:

$$\mathbf{B} = \begin{bmatrix} Y_1(\theta_1,\phi_1) & Y_2(\theta_1,\phi_1) & \cdots & Y_K(\theta_1,\phi_1) \\ Y_1(\theta_2,\phi_2) & Y_2(\theta_2,\phi_2) & \cdots & Y_K(\theta_2,\phi_2) \\ \vdots & \vdots & \ddots & \vdots \\ Y_1(\theta_N,\phi_N) & Y_2(\theta_N,\phi_N) & \cdots & Y_K(\theta_N,\phi_N) \end{bmatrix} \tag{2.28}$$

The equation in discrete form with relation to signal S is:

$$\mathbf{S} = \mathbf{B} \cdot \mathbf{C} \tag{2.29}$$

where $c_j = \int_\Omega E(\theta,\phi)Y_j(\theta,\phi)d\Omega$ and $d\Omega = \sin\theta d\theta d\phi$.

A regularization term is added to improve the estimation of the harmonic coefficients.

$$E(f) = \int_\Omega (\Delta_b f)^2 d\Omega \tag{2.30}$$

where Δ_b is the Laplace-Beltrami operator.

In a spherical coordinate system Δ_b can be defined as:

$$\Delta_b = \frac{1}{\sin\theta}\frac{\partial}{\partial\theta}\left(\sin\theta\frac{\partial}{\partial\theta}\right) + \frac{1}{\sin^2\theta}\frac{\partial^2}{\partial\phi^2} \tag{2.31}$$

Spherical harmonic functions are eigenfunctions of the Laplace-Beltrami operator.

$$\Delta_b Y_l^m(\theta,\phi) = -l(l+1)Y_l^m(\theta,\phi) \tag{2.32}$$

By substituting the function as a sum of spherical harmonic basis functions, the regularization factor can be written in discrete form as:

$$\begin{aligned} E(f) &= \int_\Omega (\Delta_b f)^2 d\Omega = \int_\Omega \Delta_b(\sum_p c_p Y_p)\Delta_b(\sum_p c_p Y_p)d\Omega \\ &= \int_\Omega (-\sum_p l_p(l_p+1)c_p Y_p)(-\sum_p l_p(l_p+1)c_p Y_p)d\Omega \\ &= \sum_j^K l_j^2(l_j+1)^2 c_j^2 = \mathbf{C}^T \cdot \mathbf{L} \cdot \mathbf{C} \end{aligned} \tag{2.33}$$

Spherical harmonic coefficients can be estimated with regularization using the least squares method as,

$$\mathbf{C} = (\mathbf{B}^T\mathbf{B} + \lambda\mathbf{L})^{-1}\mathbf{B}^T\mathbf{S} \qquad (2.34)$$

where λ is regularization factor and $\mathbf{L}$ is $K \times K$ diagonal matrix with $l_j^2(l_j + 1)^2$ as the diagonal term.

Using above equation, coefficients for oriented distribution function are estimated as follows:

$$\mathbf{C}' = \mathbf{P}(\mathbf{B}^T\mathbf{B} + \lambda\mathbf{L})^{-1}\mathbf{B}^T\mathbf{S} \qquad (2.35)$$

where, $\mathbf{C}'$ are spherical harmonic coefficients of ODF and $\mathbf{P}$ is a diagonal matrix with entries $P_i(0)$.

Q-ball imaging provides the best estimate of parameters with b-value in range of 2000-3000. It requires 100 or more gradient direction to resolve multiple fibers consistently [111]. Although Q-ball imaging can resolve multiple fiber orientation, it estimates diffusion ODFs which essentially capture a Gaussian diffusion process. Further techniques like constrained spherical deconvolution can be used to estimate fiber ODFs.

2.4.3 Diffusion Spectrum Imaging

A second non-parametric technique, Diffusion Spectrum Imaging (DSI), uses the fact that the PDF is related to the diffusion signal by a Fourier relationship. It uses a large number of diffusion-weighted images to estimate the probability density function of the displacement of water molecules (PDF) using a direct Fourier transform. Practically, a limited number of samples is acquired for the estimations. Wedeen et al [48, 49] uses 515 gradient images (q-space samples) to estimate the PDF. They use a Cartesian sample lattice to sample q-space. As typical in any

discrete signal processing analysis, a window filter is applied to reduce spectral leakage. A Hanning window is applied before performing the Fourier transform to smooth the attenuated echo signal to prevent truncation error [48, 49, 122]. Diffusion weighted signals ($E(q)$) are inter/extrapolated to do the numerical Fourier transform.

$$\frac{S(\vec{\mathbf{q}})}{S(0)} = E(\vec{\mathbf{q}}) = \int_{\mathbb{R}^3} P(\vec{\mathbf{R}}, \Delta)\, e^{2\pi \vec{\mathbf{q}} \cdot \vec{\mathbf{R}}}\, d\vec{\mathbf{R}} \tag{2.36}$$

The PDF estimation is computed by taking the inverse Fourier transform,

$$P(\vec{\mathbf{R}}, \Delta) = \int_{\mathbb{R}^3} E(\vec{\mathbf{q}})\, e^{-2\pi \vec{\mathbf{q}} \cdot \vec{\mathbf{R}}}\, d\vec{\mathbf{q}} \tag{2.37}$$

where

$$\vec{\mathbf{q}} = \frac{\gamma \vec{\mathbf{G}} \delta}{2\pi}, b = 4\pi^2 \left\| \vec{\mathbf{q}} \right\|^2 \left(\Delta - \frac{\delta}{3} \right)$$

In DSI reconstruction the PDF is calculated by first by applying an inverse Fourier transform [48, 49, 122] equation 2.37. A Hanning filter is applied to reduce higher-frequency noise. The ODF is then estimated by solving equation 2.38. The major limitation of DSI technique is due to large sampling required to cover q-space to reconstruct the probability density function. In a typical DSI protocol, 500 to 1000 images are needed for the Fourier transform. In recent studies [123, 124] this limitation is addressed using Multi-band techniques. Typically the maximum multi-band factor used in a diffusion scan is three, thus reducing scan time up to factor of three (at the cost of reduced SNR). The Fourier relationship to estimate the PDF holds for a short gradient pulse. This is an idealistic assumption for typical MR scanner.

2.4.4 Generalized Q-Sampling Imaging

A third non-parametric reconstruction technique, GQI [36], combines diffusion spectrum imaging reconstruction and oriented distribution function estimation to approximate ODF values directly from diffusion weighted images. Tuch's definition of the ODF [58, 59] is used as in Q-Ball reconstruction [60, 61], but the method of estimating the ODF is different than in Q-ball reconstruction. Generalized Q-sampling imaging [36] combines the Fourier and ODF integrals to further solve the equation 2.41 and 2.43 analytically

$$\Psi(\hat{u}) = \int_0^\infty P(R\hat{\mathbf{u}}, \Delta) \, dR \tag{2.38}$$

where $\vec{\mathbf{R}} = R\,\hat{u}$.

In the above definition the determinant of the Jacobian term is not included while converting from a Cartesian to a spherical coordinate system. The Jacobian term that is R^2 can be added into the integral to get a true probability density function [64, 65], which leads to a second definition of the ODF.

$$\Psi(\hat{u}) = \int_0^\infty R^2 \, P(R\hat{\mathbf{u}}, \Delta) \, dR \tag{2.39}$$

In the above integral, the upper limit will be truncated to L_Δ to avoid high frequency noise. Note that noise will be greater in the R^2-weighted ODF. Details about the choice of L_Δ are described in [36]. L_Δ can be written in terms of diffusivity of water D and effective diffusion time τ with is dependent on the q-vectors/b-values. According to Einstein's equation,

$$L_\Delta \propto \sqrt{6D\tau}$$

$$L_\Delta = \sigma\sqrt{6D\tau} \tag{2.40}$$

with $b = \sqrt{2\pi \|\vec{\mathbf{q}}\|} \tau$. σ is an adjustable factor. Typical value of σ is 1.1 to 1.25. After substituting these terms we can get,

$$2\pi L_\Delta \vec{\mathbf{q}} \cdot \vec{\mathbf{R}} = \sigma \sqrt{6Db} \; \hat{\mathbf{q}} \cdot \hat{\mathbf{u}} \tag{2.41}$$

where,

$$\hat{q} = \frac{\vec{\mathbf{q}}}{\|\vec{\mathbf{q}}\|}$$

Further, the diffusion coefficient of water at 25°C is 2.51×10^{-3} mm^2 s^{-1} which gives,

$$2\pi L_\Delta \vec{\mathbf{q}} \cdot \vec{\mathbf{R}} = \sigma \sqrt{0.01506 \cdot b} \; \hat{\mathbf{q}} \cdot \hat{\mathbf{u}} \tag{2.42}$$

Note that in the GQI [36] method the diffusion coefficient of water is assumed to be the same for each voxel, and this may not be true for brain tissue. Other methods such as restriction spectrum imaging [125] use different values of diffusivity to model different tissue compartments.

$$\psi_{voxel}^{GQI}(\hat{u}) = L_\Delta^3 \int_{\mathbb{R}^3} E_{voxel}(\vec{q}) \, f(2\pi L_\Delta \vec{q} \cdot \hat{u}) \, d\vec{q} \tag{2.43}$$

where $f = f_1$ if equation 2.38 is used and $f = f_2$ if equation 2.39 is used; where:

$$f_1(x) = \begin{cases} \dfrac{\text{sinc}(x)}{L_\Delta^2} & \text{if } x \neq 0 \\[2mm] \dfrac{1}{L_\Delta^2} & \text{if } x = 0 \end{cases} \tag{2.44}$$

$$f_2(x) = \begin{cases} \dfrac{2x\cos(x) + (x^2 - x)\sin(x)}{x^3} & \text{if } x \neq 0 \\[2mm] \dfrac{1}{3} & \text{if } x = 0 \end{cases} \tag{2.45}$$

Combining equations 2.37 and 2.38 will smooth the ODF signal and provide a less noisy ODF.

The GQI technique uses a similar acquisition for ODF reconstruction and therefore requires more scanning time. GQI estimates the values of ODF directly from diffusion weighted images as opposed to PDF in case of DSI [36]. It does not provide any fiber orientation information. Typically, constrained spherical deconvolution technique is used to estimate the fiber ODF from the diffusion ODF. But in order to utilize CSD framework (described in chapter three) the diffusion ODF need to be in spherical harmonic form. The next section presents a derivation of spherical harmonic coefficients of diffusion ODF using a DSI data set.

2.5   PROPOSED RECONSTRUCTION OF DIFFUSION

The proposed algorithm provides a method to directly estimate the coefficients of spherical harmonics [60, 61] from a DSI data set.

$$\psi_{voxel}(\hat{u}(\theta,\varphi)) = \sum_{l=0}^{L_{max}} \sum_{m=-l}^{m=l} c_{lm} \, Y_l^m(\theta,\varphi) \tag{2.46}$$

where c_{lm} are spherical harmonic coefficients describing the oriented distribution function.
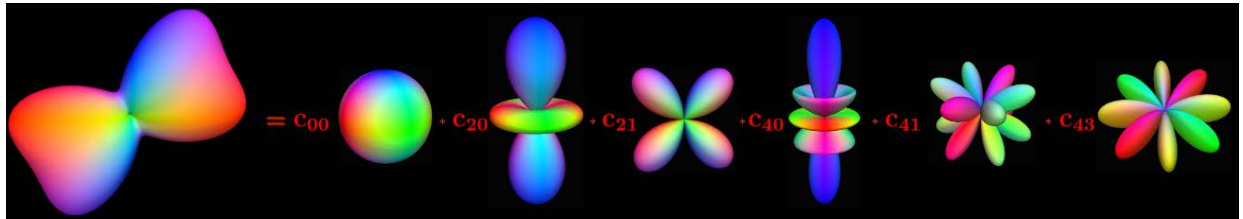
Figure 13. Orientation distribution functions are scalar valued functions on the unit sphere and can be represented as the sum of spherical harmonics (orthonormal basis for unit sphere). This expansion provides a continuous representation for the ODF.

Combining equation 2.46 and 2.43 we get,

$$\sum_{l=0}^{L_{max}} \sum_{m=-l}^{m=l} c_{lm} Y_l^m(\theta,\varphi) = L_\Delta^3 \int_{\mathbb{R}^3} E_{voxel}(\vec{q}) f(2\pi L_\Delta \vec{q} \cdot \hat{u}) \, d\vec{q} \tag{2.47}$$

This equation can be solved using the spherical harmonics transform for estimating c_{lm}.

Analytically, c_{lm} has a closed form solution,

$$c_{lm} = \int_{\mathbb{R}^3} \int_\Omega L_\Delta^3 f(2\pi L_\Delta \vec{q} \cdot \hat{u}) Y_l^m(\theta,\varphi) E_{voxel}(\vec{q}) d\Omega \, d\vec{q} \tag{2.48}$$

By rearranging terms in equation 2.48, we can relate the spherical harmonic coefficients of the diffusion ODF to the diffusion spectrum images,

$$g(\vec{q},\hat{u}(\theta,\phi),l,m) = \int_\Omega L_\Delta^3 f(2\pi L_\Delta \vec{q} \cdot \hat{u}) Y_j(\theta,\varphi) \, d\Omega \tag{2.49}$$

For a given diffusion gradient direction $\vec{q}_i$ and spherical harmonic function Y_j,

$$g_{ji} = \int_\Omega L_\Delta^3 f(2\pi L_\Delta \vec{q}_i \cdot \hat{u}) Y_j(\theta,\varphi) \, d\Omega \tag{2.50}$$

where,

$$j = j(l,m) = \frac{(l^2 + l + 2)}{2} + m$$

Equation 2.49 can be solved in discrete form as:

$$\mathbf{C} = \mathbf{G} \cdot \mathbf{E} \tag{2.51}$$

where the ith rows of matrices $\mathbf{C}$, $\mathbf{G}$ and $\mathbf{E}$ are given by,

$$\mathbf{C} = \begin{bmatrix} c_1 \\ c_2 \\ \vdots \\ c_j \end{bmatrix} \qquad \mathbf{E}_{voxel} = \begin{bmatrix} e_1 \\ e_2 \\ \vdots \\ e_j \end{bmatrix}$$

and

$$\mathbf{G} = \begin{bmatrix} g_{11} & g_{12} & \cdots & g_{1N} \\ g_{21} & g_{22} & \cdots & g_{2N} \\ \vdots & \vdots & \vdots & \vdots \\ g_{j1} & g_{j2} & \cdots & g_{jN} \end{bmatrix}$$

where $\mathbf{C} = [\, c_j \,]$, $\mathbf{G} = [\, g_{ji} \,]$ and $\mathbf{E}_{voxel} = [\, e_i \,] = [\, E_{voxel}(\vec{\mathbf{q}}_i) \,]$, $j = j(l,m) = \dfrac{(l^2 + l + 2)}{2} + m$

with l and m as order and degree of spherical harmonic function $Y_l^m(\theta, \varphi) = Y_j(\theta, \varphi)$.
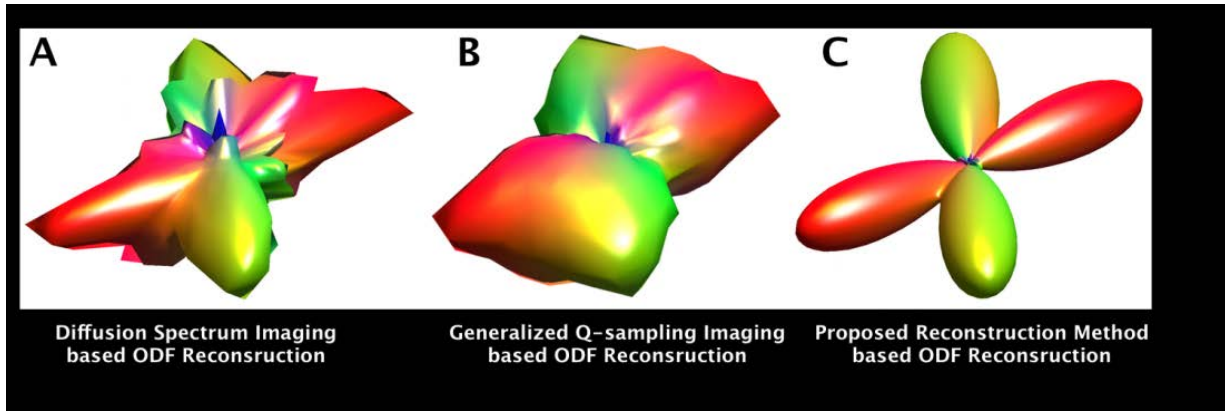
Figure 14. ODF reconstruction of a 60° angle crossing using DSI, GQI and the proposed reconstruction method. A. DSI-based reconstruction uses q-space data to create the PDF using a direct Fourier transform. The DSI-based ODF shows more noise and false diffusion peaks. B. GQI-based ODF is smoother than DSI. GQI reduces high frequency noise by solving the ODF integral analytically. C. Proposed reconstruction algorithm combines DSI and the spherical deconvolution method to find diffusion peaks. This method shows clear diffusion peaks in the ODF.

Matrix $\mathbf{G}$ is composed of two matrices, the matrix from the generalized q-sampling imaging reconstruction method and the matrix relating the spherical harmonic coefficients to the values of the ODF.

Matrix equation 2.51 can be solved by inverting $\mathbf{G}$. A regularization term is needed to invert $\mathbf{G}$ as it is a low-rank matrix. A Laplace-Beltrami operator can be used to find a regularized solution as described in [60, 61]. This method allows us to directly estimate spherical harmonic coefficients from diffusion weighted images (see Figure 14). This method can further be used to estimate the fiber ODF by performing constrained spherical deconvolution [38, 126] in ODF space (see chapter three).

2.6   LIMITATION AND FUTURE DIRECTIONS

Current constrained spherical deconvolution techniques assume a single tissue type model [43, 125, 127]. Recently, multi-tissue models have been introduced that model the response function separately for grey matter, white matter, and cerebro-spinal fluid. The multi-tissue model in [127] uses a multi-shell q-sampling scheme to estimate the volume fraction for each tissue type. Similar techniques can be used to extend the proposed reconstruction algorithm. The proposed reconstruction method also lacks error analysis to provide numerical accuracy for the method. In the future, we will analyze error in the proposed reconstruction method as a function of different parameters such as b-values, SNR, and spherical harmonic order.

2.7   CONCLUSION

In this chapter, we presented a novel reconstruction algorithm which combines generalized q-sampling imaging and spherical harmonic expansion to estimate spherical harmonic coefficients

of the diffusion orientation distribution function. Other popular techniques, such as constrained spherical deconvolution (CSD) use a single shell data-set to estimate the fiber ODF. By combining GQI and SH expansion, similar CSD techniques can be used in ODF space to estimate the SH coefficients of the fiber ODF for a DSI data set. In chapter three we will present a formulation for deconvolution techniques using the proposed reconstruction algorithm and constrained spherical deconvolution.

3.0   APPLICATION OF SPHERICAL HARMONIC COEFFICIENTS

This chapter presents constrained spherical deconvolution techniques and their application in localization and visualization of sub-cortical nuclei and in fiber tractography. A novel reconstruction technique that extends the constrained spherical deconvolution techniques introduced by Tournier et al [37, 38] to multiple b-value diffusion acquisitions is presented. The proposed technique performs constrained spherical deconvolution (CSD) in oriented distribution function (ODF) space (as opposed to diffusion space) to estimate the fiber ODF from the diffusion ODF. The technique for generating the spherical harmonic coefficients used in CSD was derived in chapter two. In section 3.1 the relationship between the fiber and diffusion ODFs is discussed. In section 3.2 the mathematical formulation of CSD is reviewed. In section 3.3 the proposed reconstruction technique is derived and discussed. The proposed technique is demonstrated on simulated datasets in section 3.4 and on human datasets in section 3.5. In this section it is also demonstrated that the estimated fiber ODF created with the proposed technique can be resampled to a high resolution space.

3.1   INTRODUCTION

Non-parametric diffusion reconstruction techniques compute an oriented distribution function on the unit sphere rather than a diffusion tensor for each voxel. This permits the

techniques to fully characterize the diffusion in all directions at each voxel. The ODF can describe the distribution function of diffusion, the diffusion ODF (dODF) [58-60], or it can describe the distribution function of the fiber population, the fiber ODF (fODF) [37, 38, 126]. One of the key problems in the diffusion imaging research field is how the dODF is related to the fODF. The dODF is estimated from diffusion weighted images using Q-Ball, generalized q-sampling imaging, or diffusion spectrum imaging reconstruction methods. The dODF is a measure of the diffusion in the imaged voxel. It is used to estimate fiber orientation in the voxel in applications such as tractography. However, the orientation estimates provided by a dODF are blurred. Similar to the effect of the point spread function blurring in MRI k-space acquisition, the point spread function in diffusion space is the response of a single direction fiber population to the applied gradient. This issue can be addressed by sharpening the diffusion ODF with deconvolution techniques. The sharpened dODF more accurately captures the fiber orientations and is called the fiber oriented distribution function, or fODF. Tournier et al [37, 38, 126] introduced the method of using spherical deconvolution to compute the fODFs. His technique uses diffusion weighted images sampled with a constant b-value (typically $b = 2000 \ s \ mm^{-2} \ to \ 3000 \ s \ mm^{-2}$) to estimate the fODF in each voxel. His original deconvolution formulation was ill posed [38] and he later addressed this by adding a regularization term in the constrained spherical deconvolution (CSD) method [37]. Alexander et al and Seunarine et al [112, 128] used a maximum entropy spherical deconvolution method to estimate fiber ODF. Their method uses a nonlinear optimization technique to sharpen the diffusion ODF and thus is computationally very expensive. Other spherical deconvolution techniques in [129] and [130] are also for the estimation of fiber orientations. Dell'Acqua et al [129] used damped Richardson-Lucy algorithm to spherical deconvolution method. Schultz et al

[130] on the other hand, proposed a framework to combine multi-tensor model with spherical deconvolution technique. Both methods estimate spherical harmonic coefficients of fiber ODF. One of the major limitations of the Tournier's CSD and related methods [129, 130] is that they can only be used for single shell diffusion acquisitions.

The reconstruction method offered in this chapter addresses this limitation of current CSD methods and extends the applications of the SH reconstruction derived in chapter two. The representation of the dODF with spherical harmonics from chapter two is now used in a constrained spherical deconvolution formulation to estimate the fODFs across multiple b-value acquisitions. Spherical harmonic coefficients estimated from diffusion spectrum images allow a continuous representation of the fODF and therefore it can be resampled into a high resolution space. In this space, nuclei in sub-cortical structures like the thalamus, cerebellum and brain stem can be localized and visualized. The high resolution fODFs can then be used in tractography to obtain better delineated fiber pathways.

The SH reconstruction method of chapter two is estimated from diffusion spectrum images. This permits the reconstruction method proposed in this chapter to use these spherical harmonics in CSD to estimate the fiber ODF from multiple b-value acquisition images; the continuous fiber ODF can be resampled to high resolution structural space. This will provide the further advantage in anatomical localization and validation of fiber pathways.

3.2 BACKGROUND

3.2.1 Constrained Spherical Deconvolution

Spherical deconvolution aims to estimate fiber ODF, distribution of fiber population than diffusion ODF which is the distribution of diffusing water molecules in underlying white matter tissue. The sharpening operation is a linear transformation of spherical harmonics coefficients of the diffusion ODF. The key idea behind sharpening is that the diffusion ODF, which is a sum of a mixture of fiber populations, can be written as the convolution between the response function, which is typically the diffusion profile of single fiber population, with the fiber ODF of interest. The fiber ODF can also be represented in terms of spherical harmonic coefficients. These coefficients can be estimated using the spherical deconvolution method. Usage of spherical deconvolution method in diffusion imaging was originally proposed by Tournier et al [37, 38] and modified by others [129-131]. Fiber ODFs can accurately delineate complex micro-structure such as fiber crossings which can lead to more accurate fiber tracking results [126].

Mathematically, for a given diffusion ODF $\Psi(\theta, \phi)$ with mixture of n fiber populations, let $\mathcal{H}_i$ represent a rotation operator such that i^{th} fiber is rotated with the $\mathcal{H}_i$ operator in a direction (θ_i, ϕ_i),

$$\Psi(\theta, \phi) = \sum_{i=1}^{n} f_i \mathcal{H}_i R(\theta) \qquad (3.1)$$

where $R(\theta)$ represents the response function estimated using the diffusion profile of single fiber.

Equation 3.1 can also be written as the convolution on a unit sphere of the response function $R(\theta)$ with the fODF $\Psi_f(\theta,\phi)$ as,

$$\Psi(\theta,\phi) = R(\theta) \otimes \Phi_f(\theta,\phi) \qquad (3.2)$$

where $\otimes$ is convolution operator and $\Phi_f(\theta,\phi)$ is fiber ODF which is sum of n Dirac delta functions corresponding to each fiber direction with volume fraction f_i within the voxel.

Spherical deconvolution is performed by first estimating $R(\theta,\phi)$ from the diffusion data or by specifying an analytical form. Typically, the response function is estimated from the data by selecting a region with higher anisotropy (high FA value). All of the fiber data is then aligned in the z-axis and averaged to estimate the response function of a single fiber population. Spherical deconvolution is a linear operation and can be reduced to a least squares estimation problem.
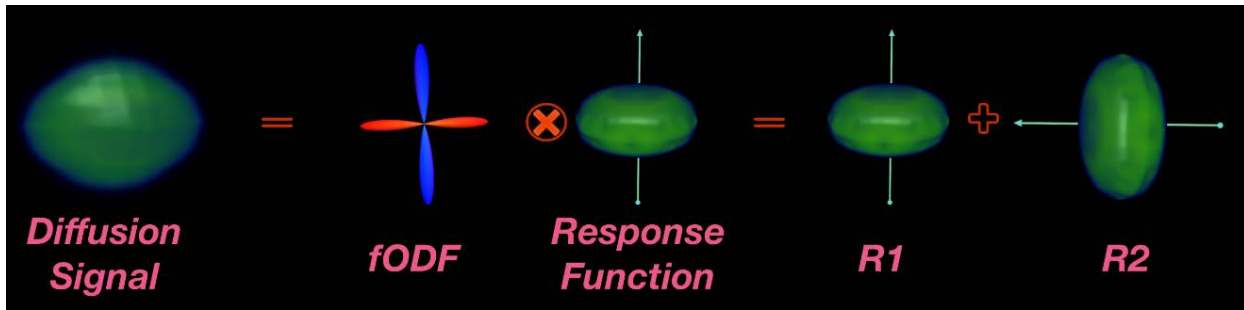
Figure 15. The diffusion signal can be written as the convolution of the fiber ODF and the response function from a single fiber population. The response functions for both crossing fiber populations are assumed to be the same.

In discrete form, if c_l and f_l are spherical harmonic coefficients of the diffusion and fiber ODF respectively then,

$$c_l = \mathbf{R}_l \cdot f_l \qquad (3.3)$$

where $\mathbf{R}_l$ is the rotational harmonic coefficient of the convolution kernel $R(\theta)$.

Spherical deconvolution is an ill posed problem; Tikhonov regularization is added to find a unique solution [37]. Constraints on spherical harmonic coefficients are added to bound the solution. Equation 3.1 further reduces into a non-linear minimization problem (see equation 3.4 that can be solved using a fixed point iteration method, see details in [37]. CSD techniques described in [37] are used to numerically estimate f_l using a fixed point iteration method with bounded spherical harmonic coefficients of the fiber ODF.

$$\min\left(\left\| \mathbf{R}_l f - b \right\|^2 + \lambda \left\| \mathcal{L}(f) \right\|^2 \right) \qquad (3.4)$$

where $\mathcal{L}$ is regularization operator and λ regularization parameter. Typically $\mathcal{L}$ is the L_2 norm operator.

3.3   PROPOSED RECONSTRUCTION METHOD IN ODF SPACE

Orientation distribution functions are functions defined on the unit sphere $\mathcal{S}_2$. Spherical harmonic functions are a well-known orthonormal basis on a sphere. As described in chapter two, diffusion ODFs can be estimated using the proposed reconstruction algorithm to directly estimate spherical harmonic coefficients of the fiber ODF from a DSI data set.

$$\Psi(\hat{\mathbf{u}}(\theta,\varphi)) = \sum_{j=0}^{K} c_j \, Y_j(\theta,\varphi) = L_\Delta^3 \int_{\mathbb{R}^3} E(\vec{\mathbf{q}}) \, f(2\pi L_\Delta \vec{\mathbf{q}} \cdot \hat{\mathbf{u}}) \, \mathrm{d}\vec{\mathbf{q}} \qquad (3.5)$$

Combining equation 3.1 and equation 3.5 we get,

$$R(\theta) \otimes \Phi_f(\theta,\phi) = L_\Delta^3 \int_{\mathbb{R}^3} E(\vec{\mathbf{q}}) \, f(2\pi L_\Delta \vec{\mathbf{q}} \cdot \hat{\mathbf{u}}) \, \mathrm{d}\vec{\mathbf{q}} \qquad (3.6)$$

Let $\Phi_f(\theta,\phi) = \sum_{l=0}^{K} f_l \, Y_l(\theta,\varphi)$ be the spherical harmonic expansion of the fiber ODF

where the f_l are the spherical harmonic coefficients of the fiber ODF.

$$\sum_{l=0}^{K} f_l R(\theta) \otimes Y_l(\theta,\varphi) = L_\Delta^3 \int_{\mathbb{R}^3} E(\vec{q}) \, f(2\pi L_\Delta \vec{q} \cdot \hat{u}) \, d\vec{q} \tag{3.7}$$

Equation 3.7 can be discretized in matrix form,

$$\mathbf{R}_l \cdot f_l = \mathbf{G} \cdot \mathbf{E} \tag{3.8}$$

where matrix $\mathbf{G}$ is a discrete form of the right hand side of equation 3.8 that estimates the spherical harmonics coefficients from diffusion weighted images, $\mathbf{E}$ is vector with each element as the diffusion weighted signals, and matrix $\mathbf{R}_l$ is the discrete form of the left hand side of equation 3.8. $\mathbf{R}_l$ is a low rank matrix and is non-invertible. Therefore a regularization term is needed to estimate a bounded solution for spherical harmonic coefficients f_l.

A fixed point iteration method is used to estimate the bounded solution for f_l. This method extends the constrained spherical deconvolution technique presented in Tournier's work [37, 38] to diffusion spectrum imaging (multiple b-value) acquisitions. Next section demonstrate the proposed CSD technique on a simulated and healthy subject acquired/created using diffusion spectrum imaging protocol [48].

3.4   DEMONSTRATION OF PROPOSED RECONSTRUCTION ON SIMULATED

DATA SET

The proposed reconstruction method and the constrained spherical deconvolution method are tested on a simulated data set with pure water, single fiber and crossing fiber populations. The test of this technique on a diffusion spectrum imaging scan of a healthy human subject is detailed in section 3.5

3.4.1   Simulated dataset

The diffusion signal is created for four different types of tissue: a) Free water (for example cerebral spinal fluid) b) Single fiber population (for example the corpus callosum) c) Crossing fiber population at 60° d) Crossing fiber population at 90°. The diffusion signal is used first to estimate the spherical harmonic coefficients of the ODF for each tissue type as described in Chapter 2. Spherical deconvolution, as describe in this chapter, is performed to estimate the spherical harmonic coefficients of fiber ODFs for simulated tissue type.

3.4.1.1 Creating simulated data

     A diffusion spectrum imaging protocol [48] with 257 gradient directions and $b_{max} = 7000$ is simulated. For a given fiber orientation (ϕ_i, θ_i), diffusion gradients g_i corresponding to b_i and volume fraction ν_i of the ith fiber population in a voxel, diffusion signals can be simulated using following equation,

$$\frac{S(\mathbf{g}_i, b_i)}{S_0} = \exp\left(-b_i \mathbf{g}_i^T R_{(\phi_i, \theta_i)}^T D_i \mathbf{g}_i R_{(\phi_i, \theta_i)}\right) \qquad (3.9)$$

where, D is the tensor matrix with the diagonal terms as longitudinal ($D_\parallel$) and transverse diffusivity ($D_\perp$), $S(0)$ is the proton density map and $S(g_i, b_i)$ is the diffusion weighted signal corresponding to gradient direction g_i and b-vector b_i.

This is a general equation for diffusion. For computation simplicity we chose a tensor model in the simulation as opposed to restricted diffusion. In this simulation, $D_\parallel$ and $D_\perp$ are assumed to be 1.70×10^{-3} mm^2 s^{-1} and 0.3×10^{-3} mm^2 s^{-1} for each fiber population respectively. Equal volume fractions are assumed (i.e., $v_i = 0.5$) in the case of crossing fibers. The tensor matrix D is rotated using the rotational matrix, $R(\phi_i, \theta_i)$ corresponding to each fiber orientation (ϕ_i, θ_i).

3.4.1.2 Results

The fiber ODF for pure water, single fiber and crossing fiber orientation with $60°$ and $90°$ crossing angles, are estimated using the deconvolution method described in the previous sections. Figure 16 shows the diffusion ODF estimated using the reconstruction algorithm described in chapter two. Diffusion ODFs are blurry but smoother. Blurriness of diffusion ODF leads to the uncertainty in the underlying fiber orientation. The fiber ODF estimated using the spherical deconvolution technique shows a sharper ODF. Sharper fiber ODF reduces uncertainty of peak finding see Figure 17. Methods such as those discussed in [132] and [133] models the uncertainty in the fiber peaks using Bingham and Watson distribution functions. Like spherical harmonic, Watson and Bingham defined on the sphere [134]. These probability distribution function is used to estimate expected fiber peaks along with standard deviation. Although

60

spherical deconvolution produces a sharper ODF, ODF in pure isotropic voxel have spurious peaks. False ODF peaks are due the choice of response function. Current choice of response only consider single fiber population. Method described in [127] uses multiple response function for estimation of volume fraction of tissue type in a voxel.
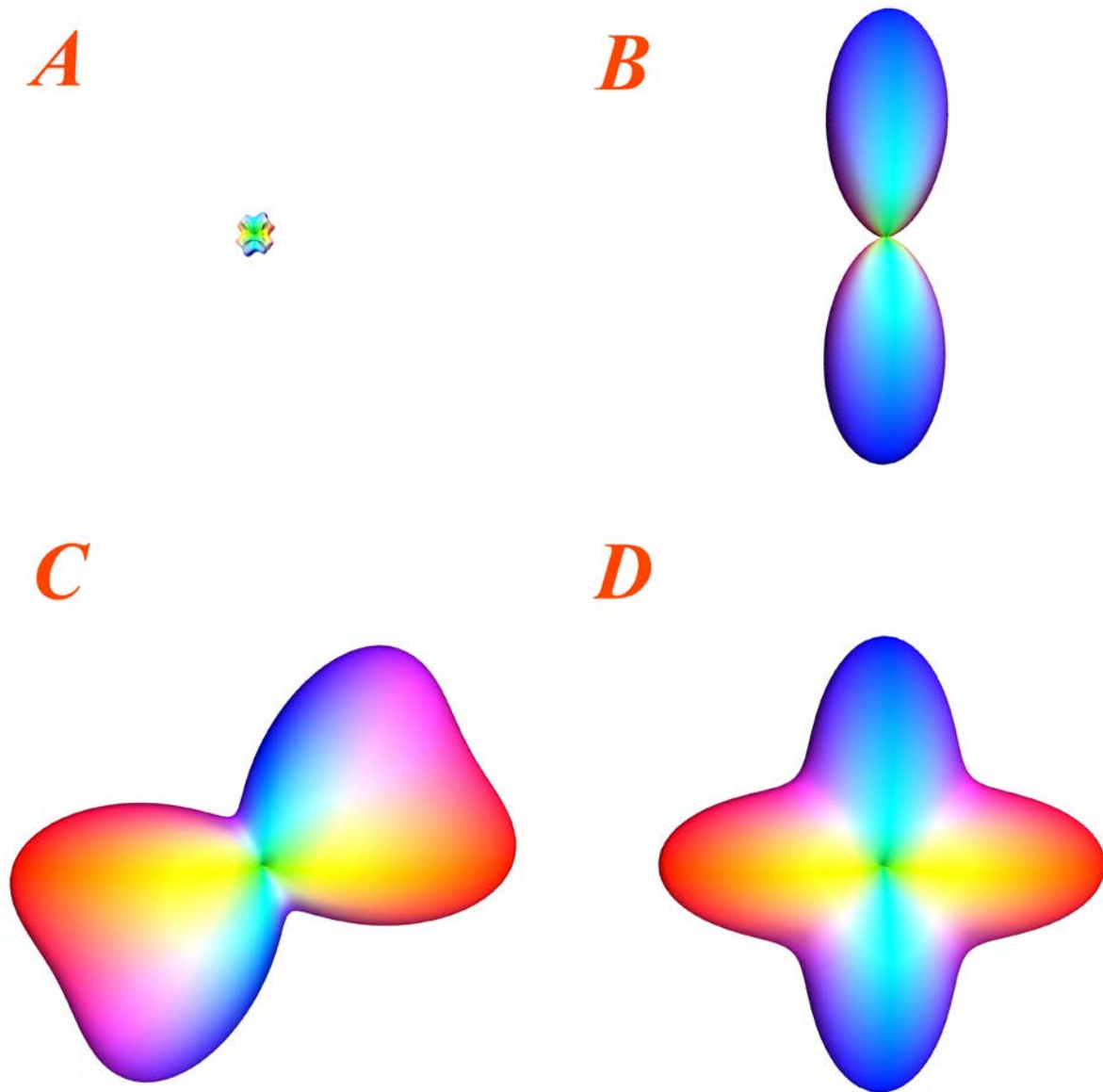
Figure 16. Diffusion orientation distribution function estimated using proposed algorithm described in chapter two. A) Voxel containing cerebral spinal fluid. B) Single fiber population. C) Crossing fiber population at a $60°$ angle D) Crossing fiber population at a $90°$ angle.
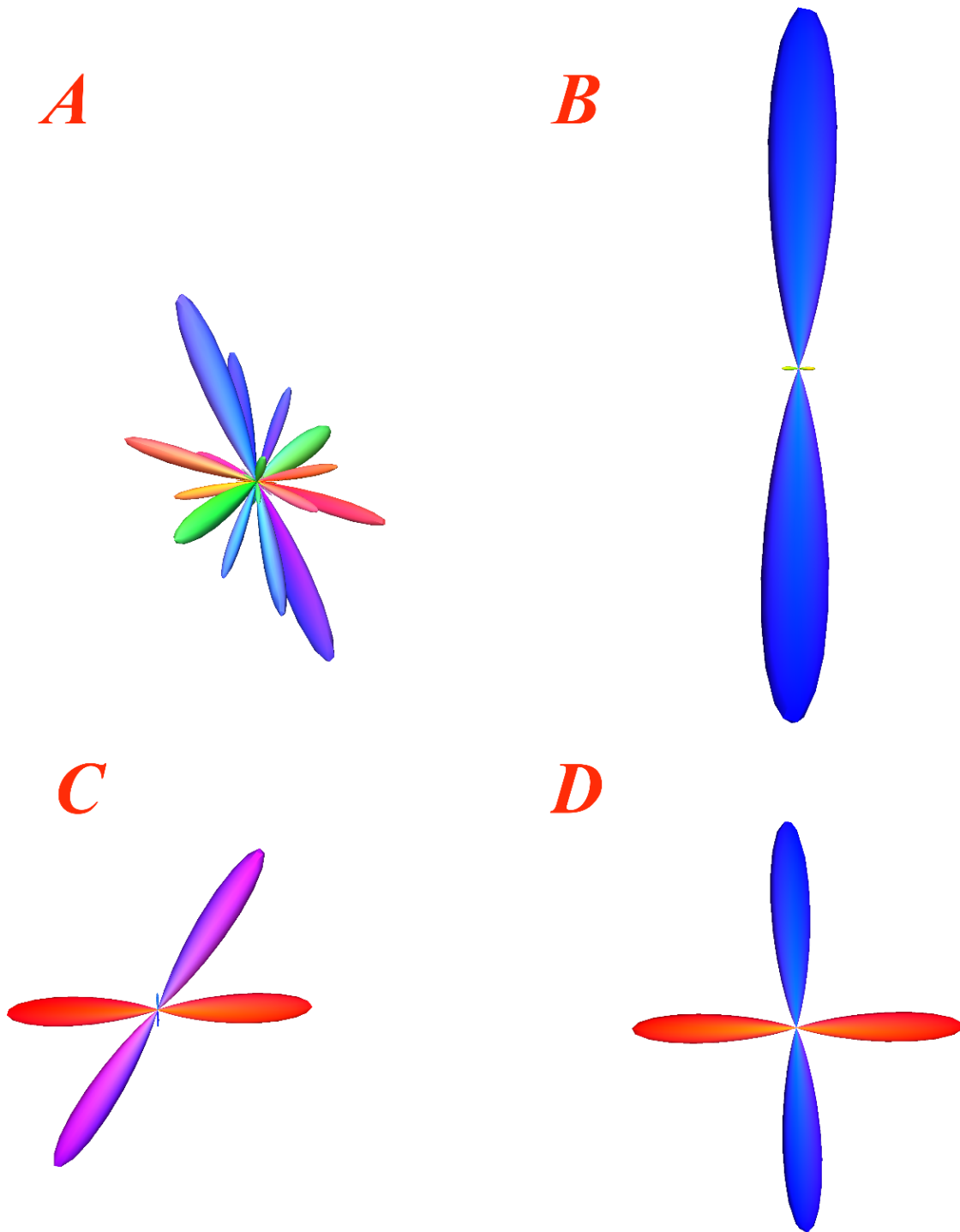
Figure 17. Fiber orientation distribution function estimates using constrained spherical deconvolution techniques. A) Voxel containing cerebral spinal fluid. B) Single fiber population. C) Crossing fiber population at a 60° angle D) Crossing fiber population at a 90° angle.

3.5   DEMONSTRATION OF PROPOSED RECONSTRUCTION ON HUMAN DATA SET

3.5.1   MR Acquisition

MR images were collected on a 3T Siemens Tim Trio with a 32 channel head coil with a whole body gradient $\|G\|_{max} = 40mT / s$ at the Magnetic Resonance Research Center (MRRC), University Of Pittsburgh. A diffusion spectrum imaging [48] scan with total of 258 diffusion weighted images, 257 gradient directions with $b_{max} = 7000 \ s \ mm^{-2}$ and one $b = 0$ with an axial echo-planar imaging readout (EPI) are acquired. Total time to acquire diffusion weighted images is 45 minutes. A fixed echo time of $TE=92ms$ and repetition time of $TR=3000ms$ is used for all diffusion measurements. A matrix of 96×96 is used over a field of view (FOV) of 224×224 for an EPI readout, which results in an isotropic voxel size of $2.4 \times 2.4 \times 2.4mm^3$. A total of 63 axial slices are acquired over the whole brain. A high resolution T1 weighted image (10 minutes) is also acquired using an axial magnetization prepared rapid gradient echo (MPRAGE) sequence with $TR = 2110 \ ms$, $TE = 2.63 \ ms$ and a flip angle of 8°. A total of 176 axial slices were acquired to cover the whole brain.

Figure 18. Raw Diffusion Weighted Images of a coronal slice. A) T1 image B) DWI with b = 0 Image. (C), (D), (E) and (F) DWI with $b_{max} = 1000, 3000, 5000, 7000 \ s \ mm^{-2}$.

3.5.2 Diffusion MRI Processing

The proposed reconstruction algorithm and spherical deconvolution methods described above are developed and implemented in-house using MATLAB [135]. Diffusion ODFs are estimated voxel-wise using GQI technique in raw diffusion-space (low resolution space). The proposed reconstruction algorithm with the spherical deconvolution technique is applied voxel-wise to estimate the spherical harmonic coefficients of the fiber ODFs. Fiber ODFs are then resampled into a higher resolution space (1mm isotropic) using a linear interpolation of the spherical harmonic coefficient estimated in equation 2.48. MRTrix [136] software is used for ODF visualization. Fiber peaks are estimated from the fiber ODF using the peak finding program implemented in the MRtrix software [136]. Estimation of peaks provides the fiber orientation and the corresponding anisotropic values. These anisotropic values and fiber orientations are further used to perform fiber tracking using DSIStudio software [32, 137].

3.5.3   Registration and sub-sampling spherical harmonic coefficients of the fiber ODF

Spherical harmonic coefficients of the fODF estimated from constrained spherical deconvolution can be registered to a high resolution space such as an MPRAGE/T1. First a rigid-body transformation matrix is estimated by registering the $b = 0$ diffusion image to the T1 image. This transformation matrix is further used to resample onto higher resolution T1 space and to orient fODF in each voxel using the method described in [136]. Note, ODFs are defined on sphere and therefore cannot be resampled using typical Euclidean techniques. Resampling of the spherical harmonic coefficients of the fiber ODF is also performed to create a detailed map of fiber peaks in each voxel. Although we are not creating any new information, we are using neighborhood information to create a smooth interpolation of the ODF. For visualization purposes peaks of the fiber ODF weighted by the value of the fODF at those peaks are mapped to the RGB color channel to create a directional encoded color volume map (DEC). These sub-sampled fiber peaks are used to localize sub-cortical nuclei in the thalamus and cerebellum using FSL's fslview software [138]. High and resolution fiber peaks are also used in fiber tracking of three major white matter pathways using DSIStudio software [137] to demonstrate the accuracy of techniques.

3.5.4   Results and Discussion

3.5.4.1 Localization and Visualization of Sub-cortical Nuclei

Three subcortical regions, the thalamus, cerebellum and brain stem, were chosen to demonstrate the application of the method described in this chapter. Two DEC maps are estimated using a spatially resampled fODF (high resolution) and non-resampled diffusion ODF

(low resolution). In high resolution fiber ODF continuous spherical harmonic coefficient are spatially resampled using FSL. Low resolution diffusion ODF values are estimated using GQI [36] techniques for each voxels. These structures are identified and a directional encoded color (DEC) map estimated using high resolution fiber ODFs is compared to a DEC map estimated using low resolution diffusion ODFs. High resolution hyper-sampled fiber ODFs show clear edges of the nuclei. Low resolution diffusion ODFs blur the edges of these small thalamic nuclei. Thalamic nuclei cannot be parcellated using conventional MR imaging on a 1.5T or 3.0T MR scanner. Many diffusion MRI based techniques segments thalamic nuclei using various clustering technique [59, 139-144]. In this section we are using a directional encoded map directly estimated from ODF peaks to localize two ventro-lateral nuclei. Other nuclei such as dorsomedial nucleus, interlaminar nuclei, lateral posterior nucleus etc. are not clearly seen using this method. Further post processing is needed [141-144] to localize subsets of nuclei.

Thalamic Nuclei play a key role in relaying information to the cerebral cortex [145, 146]. Localization of nuclei in the thalamus has clinical application to deep brain stimulation [147, 148], epilepsy [149], Parkinson's disease [150] and obsessive compulsive disorder (OCD) [151]. The thalamus (Dorsal Thalamus) is the largest component of the diencephalon. Its primary role is to relay sensory information to the cerebral cortex. It is composed of various nuclei which primarily project to different functional regions of the cerebral cortex. There are three basic type of thalamic nuclei 1) relay nuclei 2) associative nuclei 3) non-specific nuclei [145, 146]. Relay nuclei project and receive signals from functionally distinct cortical areas. The ventral posterolateral (VPL) and ventral posteromedial (VPM) nuclei relay primary sensory signals to the cortex [152]. The Ventrolateral (VL) and Ventroanterior nuclei are involved in feedback

signals of the basal ganglia output [153]. Associative nuclei receive signals and project back to the cortex in the associative area to regulate activity. Non-specific nuclei (intra-lamina, midline thalamic nuclei) are broadly thought to be involved in the general function of alerting [154, 155]. Different thalamic nuclei connect to different functional regions in the cerebral cortex and therefore have a different connectivity pattern. This connectivity pattern can produce different colors in a directionally encoded color (DEC) map of fiber orientation. VL and VPL are localized in DEC maps of hyper-sampled fiber ODFs. A high resolution T1/MPRAGE image is used as underlay to provide anatomical location. Location of the identified nuclei are in good agreement from past literature.
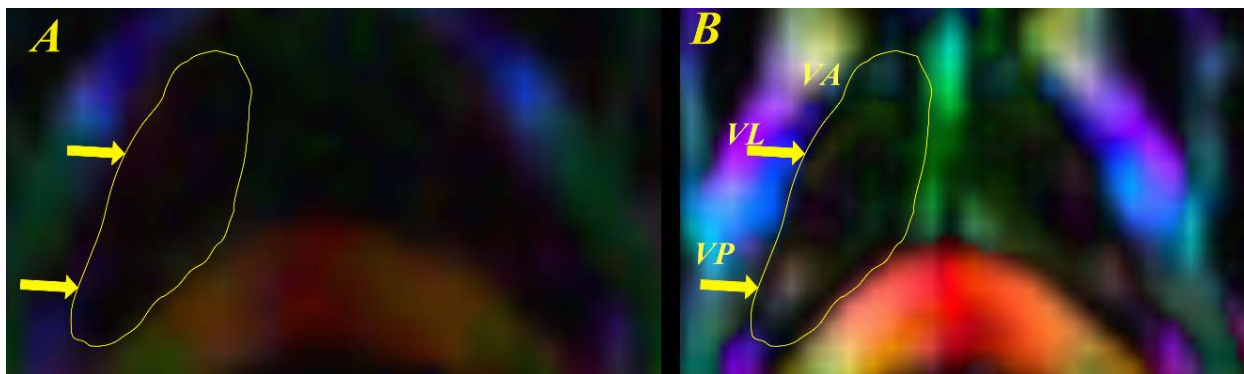
Figure 19. An axial slice of the DEC map of fiber peaks estimated from low resolution dODF (A) and high resolution fODF created by resampling spherical harmonic coefficients (see section 3.5.2) (B). Two nuclei of Thalamus (yellow curve), VP and VL, can be identified in high resolution.

The low resolution map from the diffusion ODFs does not show a clear boundary between the nuclei. Due to the large voxel size, edges of the nuclei are blurred in the DEC map from the dODFs (see Figure 19). Other methods [59, 139-144] use probabilistic tractography and cluster techniques to segment thalamic nuclei, which is computationally expensive. The current

method not only provides nuclei location but can also be used to create fiber pathways to identify tracts that connect each nucleus to cerebral cortex.

Cerebellar Nuclei The Cerebellar nuclei play an important role in motor function and language [156-160]. Identifying nuclei and their connection with the cerebral cortex and other subcortical regions could provide insight into their role in information processing between these functional regions [157, 161]. The cerebellum has four deep cerebellar nuclei embedded in the white matter in its center. Most of the fibers of the cerebellum originate from these nuclei. From lateral to medial the four cerebellar nuclei are the dentate, emboliform, globose and fastigii [162-164]. In humans, the emboliform and globose fuse to form interposed nucleus [156].

In a DEC Map estimated from the fiber ODF are shown three regions (yellow circle) which are in agreement with the anatomical locations of the three nuclei of cerebellum (see Figure 20).
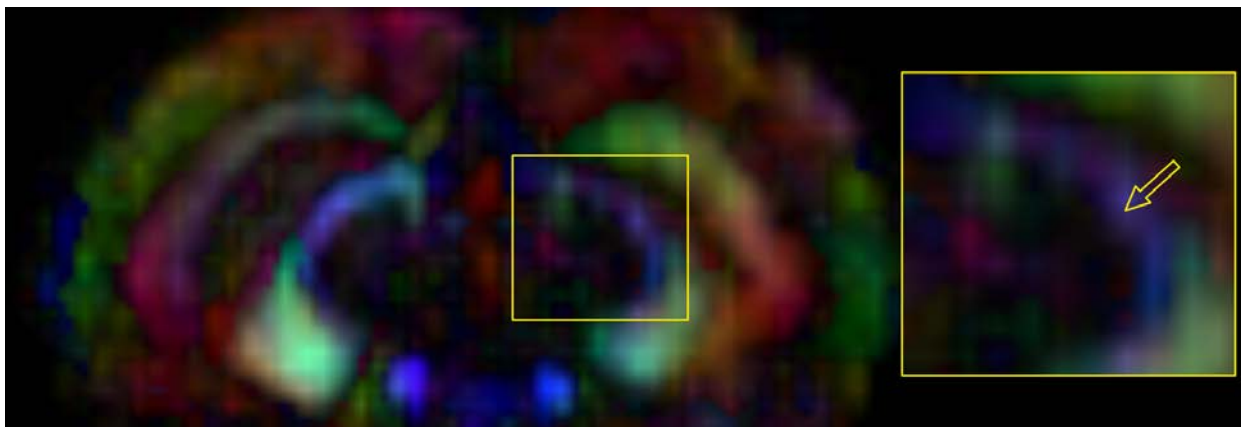
Figure 20. Three Cerebellar nuclei (yellow circle), dentate emboliform and interposed, can be identified in high resolution DEC map estimated from fiber ODF.

Brain Stem structures The brainstem is the posterior part of the human brain that includes the medulla oblongata (myelencephalon), pons (part of metencephalon), and midbrain (mesencephalon) [139]. Although it is a small region, it contains crucial white matter and grey

matter structures [165-170]. It is a challenge to localize and visualize accurately the structures in the brain stem due to its size and complexity [171-173]. DEC maps can identify some of the white matter structure. Major pathways such as the corticospinal tract (motor) [174], the posterior column-medial lemniscus pathway (fine touch, vibration sensation and proprioception) [175-177] and the spinothalamic tract (pain, temperature, itch, and crude touch) [178-180] pass though the brainstem. It plays an important role in the regulation of cardiac and respiratory functions [169, 181]. It also regulates the central nervous system and is pivotal in maintaining consciousness and regulating the sleep cycle [167, 170].
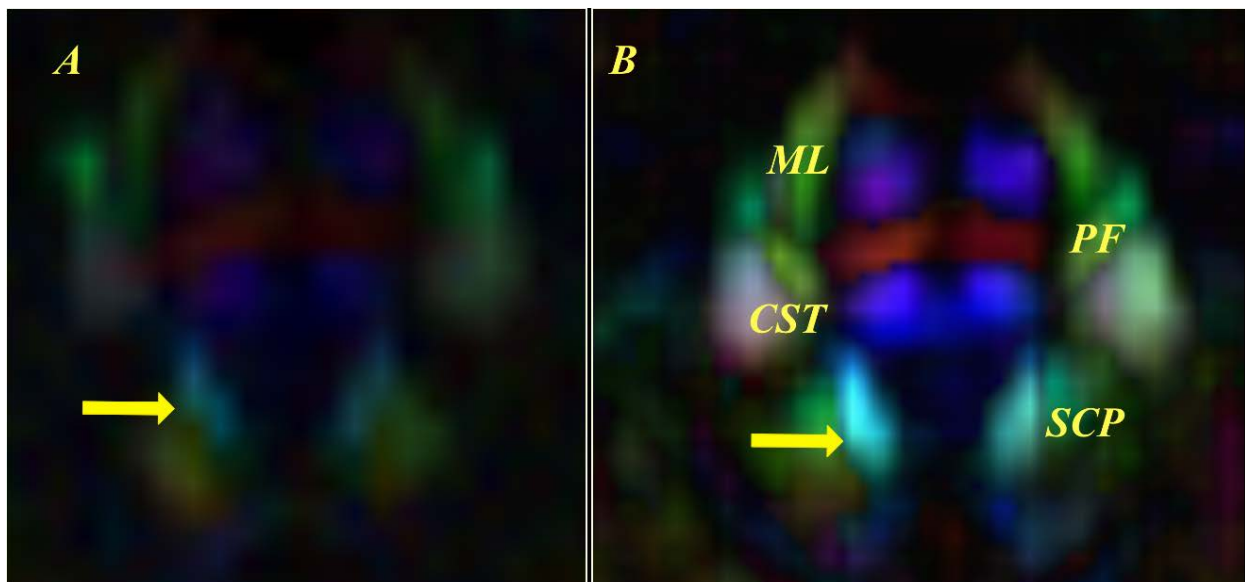
Figure 21. Brainstem regions in an axial slice of DEC Map estimated from low resolution dODF (A) and fODF (B). Edges of CST, SCP and ML is clearly visible in high resolution. Low resolution dODF show blurry edges.

Three brainstem structures are more clearly seen in the resolution DEC map estimated from fiber ODF (See Figure 21 (B)). First, cortico-spinal tracts (CST) connecting motor cortex to spinal cord can be clearly identified in higher resolution space (Figure 21 (B)). Although the lower resolution imaging shows this structure, the boundary of the CST is not very clear (Figure

21 (A)). Second major white matter structure in brain stem, medial lemniscus (ML) (upper blue region) oriented parallel to CST and pontine fossa (cross red region), connects cerebellar hemisphere separates CST and ML, are clearly visible with clear edges in high resolution space.

Resampling of fiber ODFs has a clear advantage over lower resolution diffusion ODF in localizing small structures in the human brain. Localization of these white matter structures have clinical application such as neurosurgery. Further, fiber peaks can be used in fiber tractography to reconstruct white matter pathways. The following section shows the advantage of sub-sampled fiber ODFs in fiber tractography over low resolution diffusion ODF based fiber tracking.

3.5.4.2 Tracking major fiber pathways using the proposed reconstruction method

Resampled fiber ODFs are used to create three major white matter fiber pathways: the fornix, arcuate fasciculus and superior cerebral peduncle (SCP) on a healthy subject. For comparison purposes, fiber tracking is performed on lower resolution diffusion ODF space to segment three tracts, fornix, arcuate fasciculus and superior cerebral peduncle (SCP). In this section the comparison of lower and high resolution data sets highlights features of fiber tracts which will be useful to access accuracy. It is important to note that fiber tracts are in continuous space for both the lower and higher resolution space, but resampling of the underlying information can produce less noisy tracts. The high resolution fiber tracking data set shows qualitatively better results than the lower resolution data set. Resampling of fiber ODFs enhances the endpoints of fiber tracts which can help identify functional GM regions by WM tract or sub-tract termination regions and produces fewer noise fibers in crossing regions.

Fornix The Fornix is a well-known anatomical C-shaped structure and clearly identified in structural images. It connects the hippocampus to the mammillary body. It is part of the limbic system. It is involved in recall memory [182, 183]. Damage to the fornix can cause difficulty in recalling long term memory [9, 184, 185].

Both diffusion and fiber ODF based fiber tracking can successfully segment the fornix on both hemispheres. The overall structure of the fornix is very similar in both cases, but in low resolution imaging the end part abruptly stops in white matter whereas in high resolution it has better segmentation on both hemispheres. Another important features is the intra-hemispheric gap in the fornix. High resolution clearly shows the anatomically known gap as compared to lower resolution. This effect is due to resampling of the fiber ODF. The resampled fiber ODF is robust near the edges of white matter structures as show in the previous section for subcortical nuclei (see Figure 22).
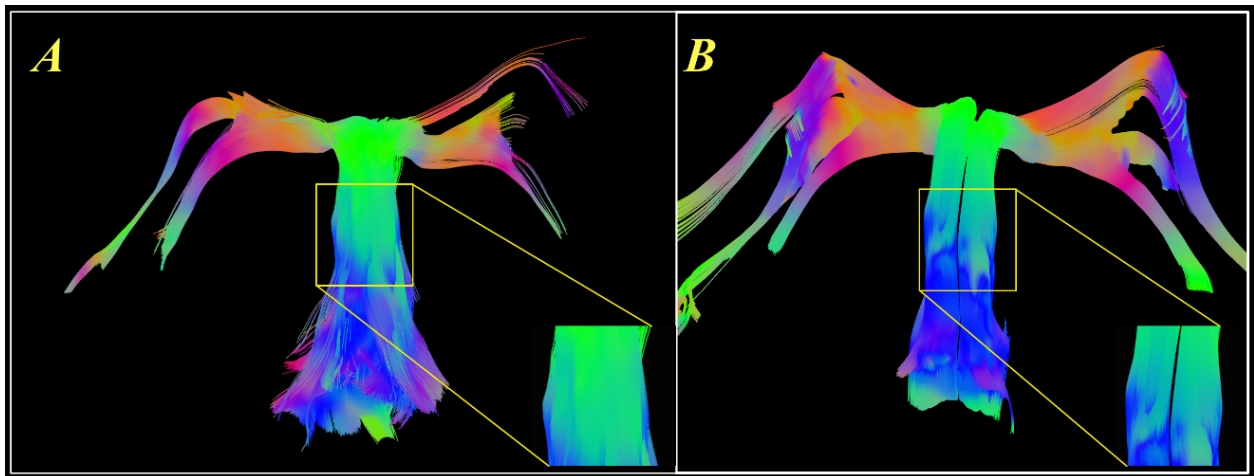
Figure 22. Fornix tract reconstructed on both hemisphere using peaks estimated from low resolution dODF (A) and high resolution fODF (B). High resolution fODF-based fiber tracking shows inter-hemispheric space and have better fiber termination at mammillary body.

71

Arcuate fasciculus The arcuate fasciculus is a white matter pathway that is connected to the inferior and middle frontal cortex to the temporal cortex [186-188]. Functionally, the arcuate is a connection between two important areas in the human brain involved in language processing: Broca's area which is part of the inferior frontal gyrus involved in speech production and Wernicke's area which is part of the posterior temporal gyrus involved in production of written and spoken language [16, 189].

Both diffusion and fiber ODF based fiber tracking reconstruct the arcuate tract. Endpoints of reconstructed tracts are consistent with the known anatomical location [190]. The high resolution arcuate tract qualitatively shows less noise and better endpoints terminating at grey-matter white-matter border (see Figure 23). The endpoints of the arcuate connect to different functional regions. These sub-segments of arcuate tracts may provide insight into functional regions involved in language processing.
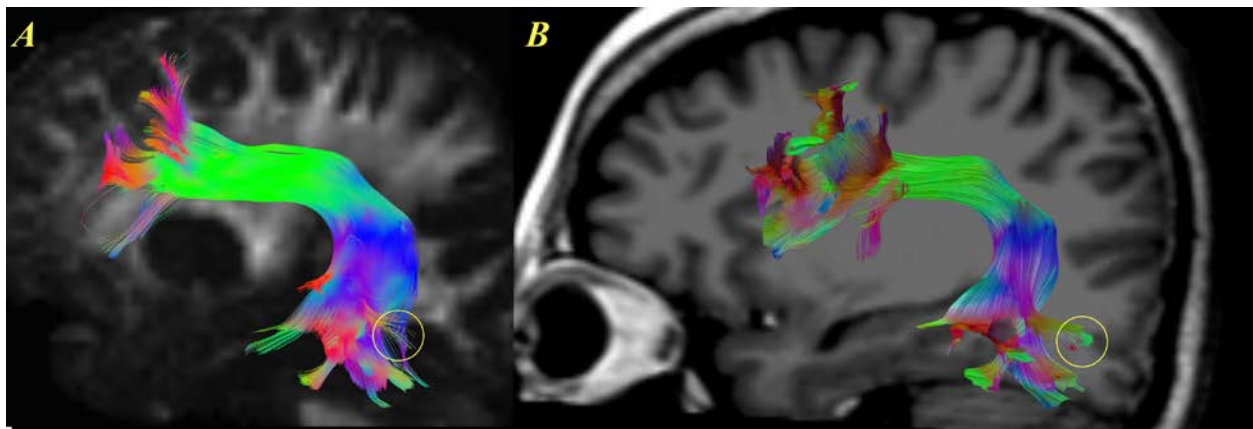
Figure 23. Arcuate tract reconstructed on left hemisphere using peaks estimated from high resolution fODF (A) and low resolution dODF (B). High resolution fODF-based fiber tracking shows better fiber termination at GM-WM border.

Superior cerebellar peduncles Tracts The superior cerebral peduncle is a white matter structure that connects the cerebellum to the midbrain. It consists of the efferent fibers from the cerebellum to the thalamus and the red nucleus. The Superior cerebellar peduncle decussates in the midbrain and creates an anatomically known fiber crossing [191-193].

To create SCP tracts, a region of interest (ROI) is selected in an axial slice at the position where crossing tracts are easily visible and a large region of avoidance is created above the thalamus plane. Fiber tracking is preformed using the following parameters in DSI Studio software, step size = 0.5, anisotropy threshold = 0.2, number of tracts = 10,000 and smoothing parameters = 0.2. Further 10% (approx.) of fibers are trimmed to select SCP tracts. This well-known crossing region is used to test the accuracy of diffusion and fiber ODFs and corresponding fiber tracking. Both methods can successfully resolve crossing and reconstruct the superior cerebral peduncle. The high resolution SCP tract shows much less noise in the crossing region as opposed to the lower resolution SCP. Endpoints of both SCP segments are easily identified in high resolution space. The ipsilateral parts of both segments in low resolution are noisier and thus fail to identify endpoint regions (see Figure 24).
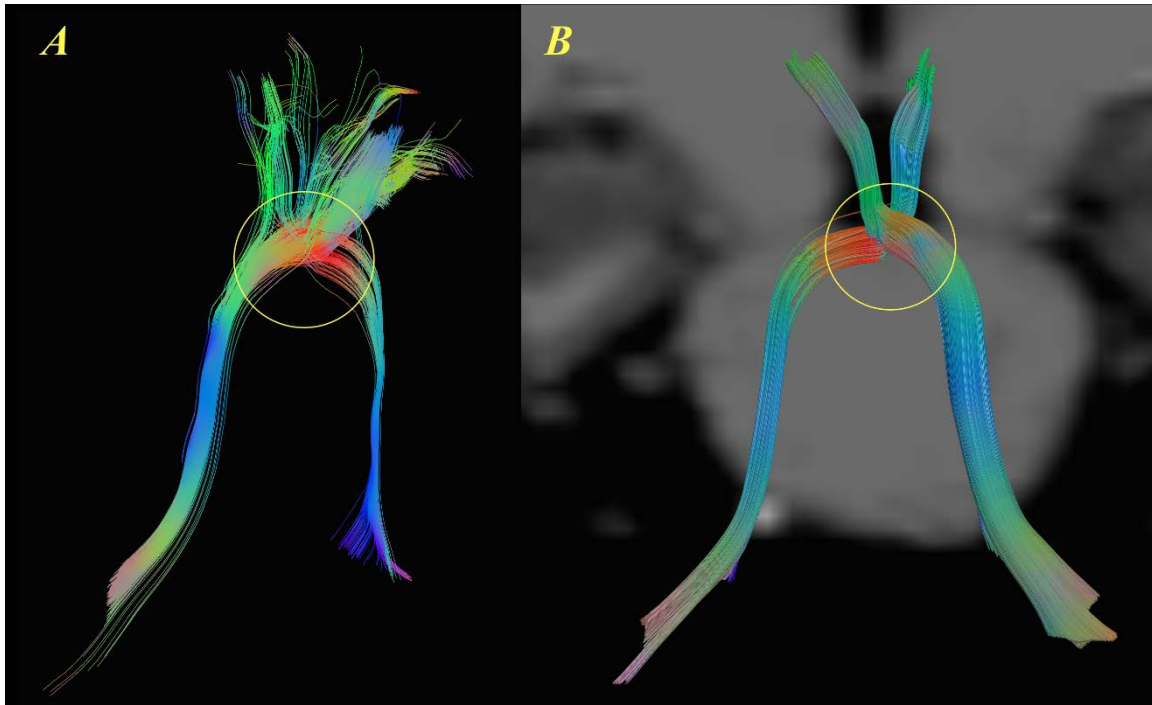
Figure 24. Superior Cerebral Peduncle tract reconstructed on both hemisphere using peaks estimated from low resolution dODF (A) and high resolution fODF (B). High resolution fODF-based fiber tracking shows clear crossing of the tracts and clear endpoint of the tracts. Low resolution has noiser crossing.

3.6   CONCLUSION

This chapter has successfully showed that fiber ODFs can be estimated using the reconstruction algorithm presented in chapter two. A novel mathematical formulation to perform constrained spherical deconvolution on the spherical harmonic coefficients of diffusion ODFs to estimate fiber ODFs was derived. It has been shown that CSD can also be applied on datasets acquired using a diffusion spectrum imaging protocol. The key difference between proposed method and CSD technique presented in [37, 38] is that it can only be applied to single shell image acquisition. This technique can be extended to multi-shell image acquisition. Juerisson et

al [127] presented CSD formulation by modeling different tissue-type and multi-shell acquisition scheme.

It was demonstrated that spherical harmonic coefficients of fiber ODFs can be resampled onto a high resolution space. Further this high resolution fODF can either be directly used or a high resolution MPRAGE/T1 image can be registered for visualization. This enables localization of small sub-cortical nuclei such as thalamic and cerebellar nuclei feasible. Finally, the advantages of resampled fiber ODF in reconstructing fiber pathways were illustrated on three major fiber tracts.

3.7   LIMITATIONS AND FUTURE DIRECTIONS

The constrained spherical deconvolution technique used in this chapter considered only one tissue model (white matter). This CSD technique can be extended to include a multi-tissue model to estimate the volume fraction of each tissue (cerebral spinal fluid, grey matter and white matter) along with the direction(s) of the fiber populations (as described in [127]). This multi-tissue method can then be further used in fiber tractography for thresholding and fiber stopping criterion.

Advanced numerical techniques can be used to improve the accuracy and computing speed for reconstructing fiber ODFs. Currently, fixed point iteration methods are used to numerically solve the constrained spherical deconvolution problem. CSD that is formulated as a least squares problem with constraints can be reformulated as a quadratic programming problem. The advantage with a quadratic programming model is it is computationally fast and produces accurate results. Similar techniques are presented in [194]. Fiber peaks estimated from fiber ODF

75

(or diffusion ODF) have uncertainty in estimated underlying fiber orientation due to noise introduce by mathematical model used or MR scanner. Probability distribution techniques such [132, 133] can model those uncertainty.

Three major white matter pathways are selected to demonstrate the techniques. A detailed sub-segmenting of these fiber tracts can be analyzed to further show the accuracy of the method. Three brain regions are selected to demonstrate the potential of the techniques to localize small brain structures. Future work will explore the effect of motion artifacts on the techniques.

4.0   QUANTIFICATION OF WHITE MATTER IN HUMAN BRAIN

Quantifying anisotropy of diffusion in white matter though MRI techniques is an active area of research. Various anisotropic metrics that describe underlying tissue type and structural connectivity have been proposed in the literature. The most popular ones, such as fractional anisotropy (FA) [67, 68], are derived from the diffusion tensor. These diffusion tensor based metrics have limited utility due to their directional insensitivity and inability to model anisotropy at multiple directions within a single voxel caused for example by crossing fibers. An anisotropic metric that is sensitive to crossing fibers and relates to the physical quantity in each voxel will enable a more accurate quantification of white matter structure. This chapter develops a novel metric, directional Axonal Volume (dAV), to quantify diffusion anisotropy in biological tissue. It is both directionally sensitive and biophysically interpretable. This chapter focuses on the derivation of the theoretical framework for voxel-wise and tract-based dAV. Its validation is addressed in chapter five using a textile based anisotropic phantom.

The motivation for the dAV metric is introduced in section 4.1. The mathematical formulation of diffusion tensor based anisotropy metrics is reviewed in Section 4.2. Section 4.3 presents the definition, derivation and discussion of the proposed dAV anisotropy metric. Section 4.4 presents an algorithmic framework to transfer the dAV metric from a volumetric framework to a tract profile based framework. This will permit dAV values to be mapped on to fiber tracts without inter mixing the anisotropies of multiple fiber tracts crossing in a voxel. In section 4.5

the dAV metric is demonstrated on simulated and human datasets. Future development and limitations of the dAV metric are outlined in section 4.8.

4.1 INTRODUCTION

Quantifying anisotropy is one of the most important tasks in diffusion-based MR imaging. Scalar metrics derived from the diffusion tensor such as fractional anisotropy (FA, mean diffusivity (MD), radial diffusivity (RD), axial diffusivity (AD)) [67, 68] are commonly used to characterize anisotropy in white matter tissue. These metrics provide more details of white matter tissue than a regular structural MRI or CT scan [90]. These tensor based metrics are successfully used in research studies such as amyotrophic lateral sclerosis [8], Multiple sclerosis [104], Schizophrenia [195] etc. They are also used in clinical settings to locate areas of stroke damage [12, 196], white matter lesions [197-200], and degeneration in diseases such as Huntington's disease [14, 106], Parkinson's disease [34], Obsessive Compulsive Disorder [6], Schizophrenia [34, 195, 201]. Although useful in these contexts, these metrics have significant drawbacks. One of the key limitations of tensor based metrics is in brain regions with fiber crossings. These metrics combine anisotropy from multiple fiber populations into a single statistical measure. Typically these scalar metrics are descriptive statistics of the eigenvalues of the diffusion tensor estimated using DTI [68, 95, 202]. For example, the Fractional Anisotropy (FA) [68, 95] metric is the dispersion of eigenvalues. A second limitation of these scalar metrics is that they do not relate directly to a physical property of the tissue. Therefore they can be difficult to interpret and to be applied in longitudinal or multi-site studies [111, 203-205].

The novel directional axonal volume (dAV) metric developed in this chapter presents a framework to resolve these direction insensitivity and biological interpretability issues. The dAV metric has three key parts. First, it estimates the anisotropy in each voxel at multiple directions by reconstructing the diffusion ODF [58, 59, 61]. This makes the metric robust to fiber crossings. Second, it separates out the isotropic component of diffusion at each direction so as to capture characteristics of just the specific tissue of interest, white matter axons. Although dAV quantifies anisotropic and isotropy in a voxel, it assumes that anisotropy is due to fiber tracts and that isotropy is due to pure water. This is an idealized assumption as white matter voxels contain various tissue/cells. And third, it relates the directional anisotropies to a biophysical diffusion property by weighting with a proton density map. A T2 weighted MR image can be used instead of a proton density map. The T2 weighted image can add bias into dAV due to the different T2 constants for different tissue types. The quantized directional anisotropies are then calibrated with a reference voxel with known proton density values. This relates the quantified directional anisotropies to the molar concentration of anisotropic water content for a given voxel and potentially axonal volume of underlying white matter tissue. Calibration of dAV has the potential to standardize this metric across scanners and across subjects.

4.2   DIFFUSION TENSOR BASED ANISOTROPIC METRICS

Among diffusion MRI based imaging techniques, diffusion tensor imaging is a simple way to estimate anisotropy non-invasively in biological tissue. The diffusion tensor can be estimated using a minimum of six diffusion weighted images and one non-weighted ($b = 0$) image [68].

Ordinary least squares and other nonlinear techniques are used to estimate six parameters of a rank two tensor (a 3x3 positive definite matrix), see chapter two for details. Diffusion tensors estimated using ordinary least squares are sometimes symmetric not positive definite matrices. Positivity constraints are applied on eigenvalues $(\lambda_1, \lambda_2, \lambda_3)$ in tensor estimation [97].

Almost all anisotropic metrics derived from diffusion tensor imaging are based on statistical summaries of eigenvalues of the tensor. The common metrics used in the literature are: mean diffusivity (MD), fractional anisotropy (FA), axial diffusivity ($D_{\parallel}$) and radial diffusivity ($D_{\perp}$) [68, 95].

Mean diffusivity is the mean of the eigenvalues. It is a statistical measure of the central tendency of the eigenvalues. It indicates whether if diffusion is free (high value) versus if diffusion is restricted or non-free (low value). It can be directly estimated using tensor coefficients by calculating the trace of the tensor matrix. The critical property of the mean diffusivity is that it is rotationally invariant i.e., it measures feature of diffusion which is independent of the laboratory or patient coordinate system [68].

$$\mathbf{MD} = \frac{(\lambda_1 + \lambda_2 + \lambda_3)}{3} \qquad (4.1)$$

Fractional anisotropy is the ratio of the standard deviation of the eigenvalues with their norm. This is a statistical measure of dispersion of the eigenvalues. If all eigenvalues are equal i.e., diffusion in each of the principle directions is equally likely, the FA value is equal to 0.0. For example, a voxel fully contained in cerebral spinal fluid (CSF) or tissue with micro-structure such that it is restricted equally in all directions has an FA value of 0.0. A voxel containing a single fiber population or diffusion that is restricted only in one direction has an FA value of 1.0.

$$\mathbf{FA} = \sqrt{\frac{3\left((\lambda_1 - \bar{\lambda})^2 + (\lambda_2 - \bar{\lambda})^3 + (\lambda_3 - \bar{\lambda})^2\right)}{2\left(\lambda_1^2 + \lambda_2^2 + \lambda_3^2\right)}} \qquad (4.2)$$

FA in crossing regions will have a lower value as two eigenvalues will have similar values i.e., $\lambda_1 = \lambda_2 \gg \lambda_3$. In crossing region fractional anisotropy has limited interpretation. As lower values of FA due to either crossing or lower anisotropy in a single fiber population [67].

Axial diffusivity, ($D_\parallel$, provides anisotropy along the fiber population and Radial diffusivity, ($D_\perp$), provides anisotropy across the fiber. In the case of a single fiber population $D_\parallel$ and $D_\perp$ provide tissue specific micro-structural information. Radial diffusivity $D_\perp$ can be sensitive to micro-structural changes like change in myelin content [7, 206, 207]. These metrics have limitation in crossing regions. They not only give a weighted average of diffusivity of crossing fibers but also cannot provide any information regarding the volume fraction for each fiber population [58, 61, 205]. Metric derived from higher order model such as multi tensor model [111], q-ball imaging [58], diffusion spectrum imaging [48] etc., can overcome some of these issues.

Other biophysical models like CHARMED [41], AxCaliber [42] etc. can estimate the volume fraction of crossing fibers and properties of tissue in terms of diffusion (diffusivity in each fiber direction, diameter of fiber(s) etc.). Some advanced diffusion MRI methods employ multiple pulsed field gradient MRI sequences to measures features like mean axon diameter and axon diameter distribution, as well. These metrics require special pulse sequences for data acquisition [42, 208, 209].

Most of the metrics described above are voxel-based. One of the advantages of voxel based metrics is the availability of volumetric based tools. For example, there are a number of

volumetric atlases [210-214], tools to create surface models from volume data, [215-217], and tools to identify regions of interest [218, 219]. However, volumetric data can be harder to interpret than tract based data because the volume data is discretized into a grid of voxels that has no relation to the imaged anatomy, whereas the tract based data is at millimeter precision and more closely relates to the white matter anatomy. The tract based data, however, provides only the geometry and location of white matter tracts; the valuable information about anisotropy estimates at each voxel is not incorporated. Mechanisms have been developed to map these voxel based anisotropic metrics onto fiber tracks [220-222]. And, methods analogous to volume based methods to compare tracts across populations and in longitudinal studies have begun to be developed [222]. These methods have only dealt with mapping scalar metrics and would need to be adapted to function on tuple based metrics such as dAV. The following section formulates the dAV metric, that is derived from the non-parametric diffusion model described in chapter two, and provides a mechanism to map it onto fiber bundles.

4.3   DIRECTIONAL AXONAL VOLUME (DAV)

DAV measures directional dependent anisotropy and relates it to the water content. DAV offers separate anisotropies for crossing fiber and calibrates the estimates thus resolving two major limitations of anisotropic scalar metrics. Directional axonal volume (dAV) can be defined as the amount of water molecules displaced due to diffusion in a given direction. DAV estimation requires two steps: Proton density estimation and ODF (diffusion or fiber) estimation at each voxel.

Given a direction $\hat{u}$ in a voxel, $dAV(\hat{u})$ is defined as the amount of anisotropic water diffused in direction $\hat{u}$ for a volume V_{voxel}.

$dAV(\hat{u}) = ($ Total spin in a voxel $) \times ($ fraction of anisotropic water diffused in direction $\hat{u})$

$$dAV(\hat{u}) = \varrho_0 \times \hat{\mu} \tag{4.3}$$

where ϱ_0 is the total spin density and $\hat{\mu}$ is the fraction of anisotropic spin diffused in direction $\hat{u}$

First, the isotropic part is removed from the ODF to estimate the pure anisotropic water content (see Figure 25). Anisotropy can be normalized to create a probability density function. It is a vector quantity defined on the sphere of the diffusion or fiber ODF. If the diffusion ODF is used in anisotropic estimation, it blurs dAV values in the fiber direction(s). The fiber ODF is better choice for dAV estimation. dAV is estimated by weighting the proton density map to the anisotropy estimates.
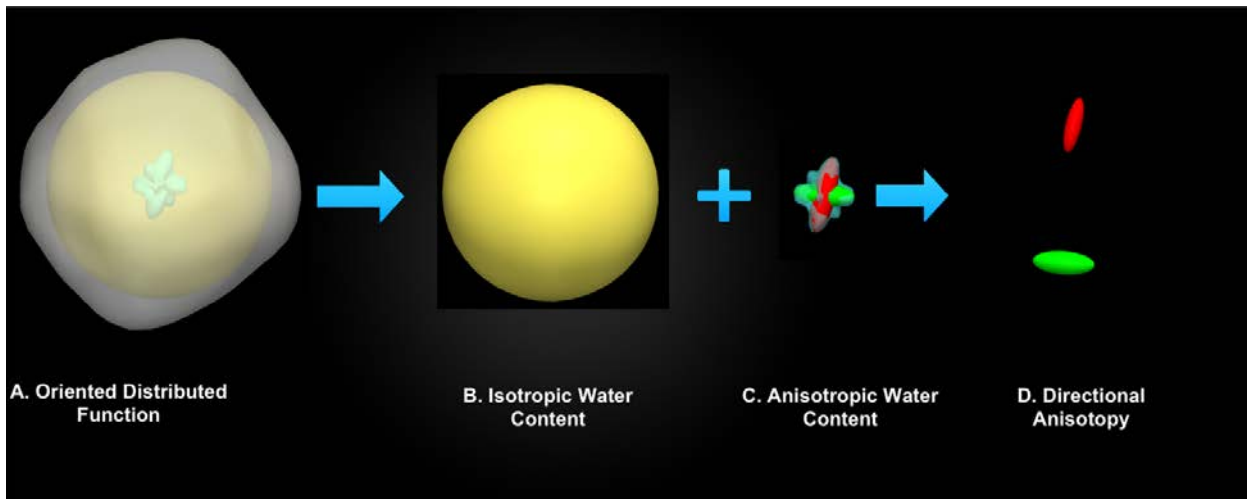
Figure 25. Orientation Distribution Function is decomposed into an isotropic and anisotropic parts. dAV is related to the anisotropic part of the ODF.

4.3.1   Spin density estimation of total water content

A proton density [27, 223, 224] map quantifies the water content (more precisely number of hydrogen protons 1H) in each voxel. The proton density map is heterogeneous across brain voxels. To calibrate water content a reference voxel is used to estimate a map ϱ_0 with the fraction of water molecules present in a voxel (total spin density map). To estimate ϱ_0, we first must pick a reference voxel with a known density of water (or a reference phantom voxel). Typical choices are a voxel completely inside CSF or a voxel from a phantom with known water content.

If the density and volume of water in a voxel are d_{ref}, V_{ref} and W is the molar mass of water, then the number of moles in the voxel is $d_{ref} V_{ref} / W$.

Let M_{ref} and M_{voxel} be the proton density signals from a reference voxel and a voxel of interest (VOI) respectively and let V_{voxel} be the volume of a voxel. Then,

$$\text{Number of Moles in VOI} = \frac{d_{ref} V_{ref}}{W} \frac{M_{ref}}{M_{voxel}} \frac{V_{voxel}}{V_{ref}}$$

$$\varrho_0 = \frac{d_{ref}}{W} \frac{M_{ref}}{M_{voxel}} V_{voxel} \tag{4.4}$$

It is important to note that Proton Density (PD) imaging requires extra scanning time. Typically we use Echo-Planner Images with multiple TEs (time of echo) to estimate PD by regressing out the $T2^*$ effect. [27, 223, 224].

$$M_{voxel} = PD_{voxel} \exp(-\frac{TE}{T2_{voxel}})$$

Without regressing out the $T2^*$ effect we will introduce a $5\% - 20\%$ error in dAV estimation depending upon the TE used in the diffusion scan and on the tissue type. This calculation was performed using a typical T2 constant for CSF, grey matter and white matter.

4.3.2 Estimation of Isotropic water content

There are many ways to estimate isotropic water content. This work used the simplest model: the minimum of the ODF values. The isotropic part includes contributions from both the hindered and free water compartments. Note that the isotropic part is a scalar quantity. The isotropic value indicates the fraction of water molecules displaced in all directions. Other methods [10, 225] describe separate modeling of free water in diffusion weighted imaging space. DAV performs the isotropic estimation in ODF space (after reconstruction step).

$$I_{voxel} = \min_{\hat{u}}(\psi_{voxel}(\hat{u})) \tag{4.5}$$

This is a simplified model of isotropy and is sensitive to noise. More sophisticated models can be used to accurately model isotropic water content [10, 225].

Combining equations 4.5 and 4.4 provides the isotropic water content in a voxel:

$$Iso_{voxel} = \varrho_0 \times I_{voxel} = \frac{d_{ref}}{W} \frac{M_{ref}}{M_{voxel}} V_{voxel} \, I_{voxel} \tag{4.6}$$

It is important to note that dAV values are dependent on the ODF used in the calculation. The dAV formulation here was derived using diffusion ODFs. Diffusion ODFs are probability distribution functions on a unit sphere. Diffusion ODF values in a particular direction represent the fraction of water molecules diffusing in that direction. Due to the non-zero radii of the fibers, water molecules move in all directions including perpendicular to the fiber axis. Therefore part

of the minimum value of a diffusion ODF is due to movement in a perpendicular direction, from within intra-cellular space. A similar diffusion process is happening in extra-cellular space. Hence, the isotropic water content estimated above is not just free water but also contains contributions from intra and extra cellular space. In the case of fiber ODFs, only the fiber population is estimated and therefore the isotropic part will be zero. Depending upon the study, either ODF can be chosen. If characterization of diffusion properties is of interest then the diffusion ODF will be used. If only the axonal bundle is of interest then the fiber ODF will be used.

4.3.3   Estimation of Anisotropic water content

The anisotropic water content can be estimated by subtracting the isotropic part from the ODF. The anisotropic part is then normalized to form a probability density function. It is the fraction of water molecules displaced due to diffusion in a voxel and is also defined on a unit sphere as ODF.

$$\mu(\hat{u}) = \psi_{voxel}(\hat{u}) - I_{voxel} \tag{4.7}$$

Combining equations 4.7 and 4.4 will provide dAV in a given direction $\hat{u}$.

$$dAV_{voxel}(\widehat{(u)}) = \varrho_0 \times \mu(\hat{u}) = \frac{d_{ref}}{W} \frac{M_{ref}}{M_{voxel}} V_{voxel} \mu(\hat{u}) \tag{4.8}$$

The anisotropic part includes contributions from both the hindered and restricted compartments. It is sensitive to changes in white matter tissue.

86

Other methods [39, 41, 42] also estimate the volume fraction of restricted and hindered compartments separately based on tissue property. The dAV framework can be modified to adapt volume fraction estimates from these models.

Voxel-wise dAV estimated by equation 4.8 is used in fiber tracking to map anisotropy onto each point in a given fiber bundle. The next section presents an algorithm to map dAV along the fiber tracts. Fiber slicing techniques are used to further estimate dAV flux along fiber bundles. The key difference between scalar based anisotropy mapping techniques (see [222]) and dAV is that the dAV technique is able to discriminate anisotropy in the direction of fibers.

4.4   MAPPING AND PROFILING OF DAV ONTO FIBER BUNDLES

Although voxel-wise metrics are an important part of group studies, tract based methods provide a better anatomical solution to study structural connectivity and probe axonal change in human brain. Methods such as TBSS [138] map anisotropy on a skeleton of FA volume maps. It maps FA values from a subject population on a template skeleton FA volume to estimate white matter changes. Although this method has the advantage of permitting statistical hypothesis testing, it doesn't provide tract specific metrics and cannot be applied to individual subjects for damage detection. This section provides a method to create tract based dAV metrics.

Tract-based metrics combined with profiling of the tract provide a mechanism to assess damage along a fiber bundle in an individual patient. Previous studies [222] have mapped scalar anisotropic metrics such as fractional anisotropy onto the tract. This section will first present a novel method to map the non-scalar dAV values onto fiber tracts and then will present a novel profiling technique to combine and project dAV values from each fiber onto a mean fiber tract.

87

These mean fiber dAV projections can be visually inspected for irregularities indicative of potential tract damage. Or, if normative data has been gathered quantitative comparisons can be performed [222]. These algorithms are independent of the fiber tracking method used to create fiber tracts. All studies in this thesis used the fiber tracking method described in [32].

4.4.1 Mapping dAV onto fiber tracts

dAV values first map onto the fiber points along the tangent direction of the fiber points. Each point of each fiber tract in a given fiber bundle has dAV values mapped. Fiber tracts are then profiled to estimate dAV flux along the fiber bundle. In order to calculate dAV changes along the fiber bundle, first a mean fiber is estimated by selecting and averaging fibers of the same length. Cutting planes are created that are orthogonal at each point of the mean fiber. dAV values are estimated at the intersection of the plane and fibers.

Like the diffusion and fiber ODFs, dAV is a function on unit sphere. The dAV values in each voxel are represented as a finite set of N directions (points), uniformly distributed on a sphere, with the dAV magnitudes discretized across these points. For a given point in a fiber, there are thus N possible dAV magnitudes (from the voxel enclosing the fiber point). Fiber points are not independent, they are part of a 3D curve and therefore each point has orientation information, the tangent. For each fiber point, the tangent is estimated and the dAV magnitude whose direction most closely aligns with the tangent direction is chosen.

In contrast, for mapping of scalar metrics, fiber tracts are not considered as 3D curves. Instead, they are taken as a set of independent points. The scalar metric is interpolated at each point without taking advantage of the local fiber orientation. The key contribution of the dAV metric is that is provides a directionally sensitive metric and it also provides a method to use that

directional information to guide and enhance the process of mapping from volumetric to tract space.

4.4.2   Tract profiling of dAV metric

After mapping dAV values onto fiber tracts, dAV of fiber bundle is reduced to a mean fiber tract. Mean fiber for a given fiber bundle is estimated by averaging fibers of similar length. Then at each points onto mean fiber, a plane perpendicular to the tangent, is selected. Fiber bundle is then cut using the selected plane. Here are the detailed steps to map dAV onto fiber bundles. Given a Fiber Bundle $\mathfrak{F}$, a collection of fibers f_i, $\mathfrak{F} = \cup_i f_i$:

1. ***Identify mean fiber*** f_{mean} ***:*** The mean fiber is calculated by selecting long fibers with similar length. Then a spline filter is used to interpolate all selected fibers such that each fiber has an equal number of points. The mean fiber is then calculated by summing these points for each of the selected fibers.

2. ***Orthogonal Planes*** $\overrightarrow{\mathbf{p_i}}$: The tangent at each point along the mean fiber (f_{mean}) is used to calculate a plane such that the normal to the plane is the same as the tangent ($\overrightarrow{\mathbf{t_i}}$) at each point ($\overrightarrow{\mathbf{p_i}}$). In other words, the equation of the plane can be described as $\overrightarrow{\mathbf{x}} \cdot \overrightarrow{\mathbf{t_i}} = \overrightarrow{\mathbf{p_i}}$.

3. ***Slicing fiber tracks using orthogonal planes***: Each fiber is then cut using the planes calculated in step (2). dAV at each point of intersection between the plane and the fibers is estimated using interpolation. Then the sum of all dAV values for each plane along the mean fiber is calculated.

Profiled fiber bundle at each point of mean fiber tract have dAV value contribution from each fibers. An average value of dAV at each point in mean fiber is mapped.

This technique has potential advantage over the technique used in [222]. DAV profiling technique uses a plane that is aligned with fiber bundle for individual as opposed to the MR scanning plane.

Other techniques such as Automated Fiber Quantification (AFQ) [222] and Tract-Based Spatial Statistics (TBSS) [138] are also used to map anisotropy onto fiber tracts or a common template volume. AFQ uses interpolation of the FA metric to map anisotropy onto each fiber point and then fibers are profiled using a scanning x-y-z plane. In contrast, dAV uses the whole ODF and the proton density map to first map anisotropy in the direction of fiber tract, and then profiling is performed along the plane of mean fibers. ODF based anisotropic maps provide a better estimate of anisotropy in crossing regions. Profiling can be performed in multiple possible ways. Planes perpendicular to a mean fiber are unique at a particular point; this is an advantage over scanning x-y-z planes.

This tract-based mechanism of mapping dAV onto fiber tracts has the potential to provide information related to structural connectivity in healthy and diseased brains without mixing the anisotropies of multiple fiber populations. This method should not be confused with simple interpolation. DAV uses fiber tract information, the ODF, and the proton density map to estimate the anisotropic map. Scalar maps like FA were used in [222] to map anisotropy onto fiber tracts. Scalar metrics were simply interpolated at each fiber point. In next section, we will demonstrate dAV technique on a simulated data set and on a healthy subject.
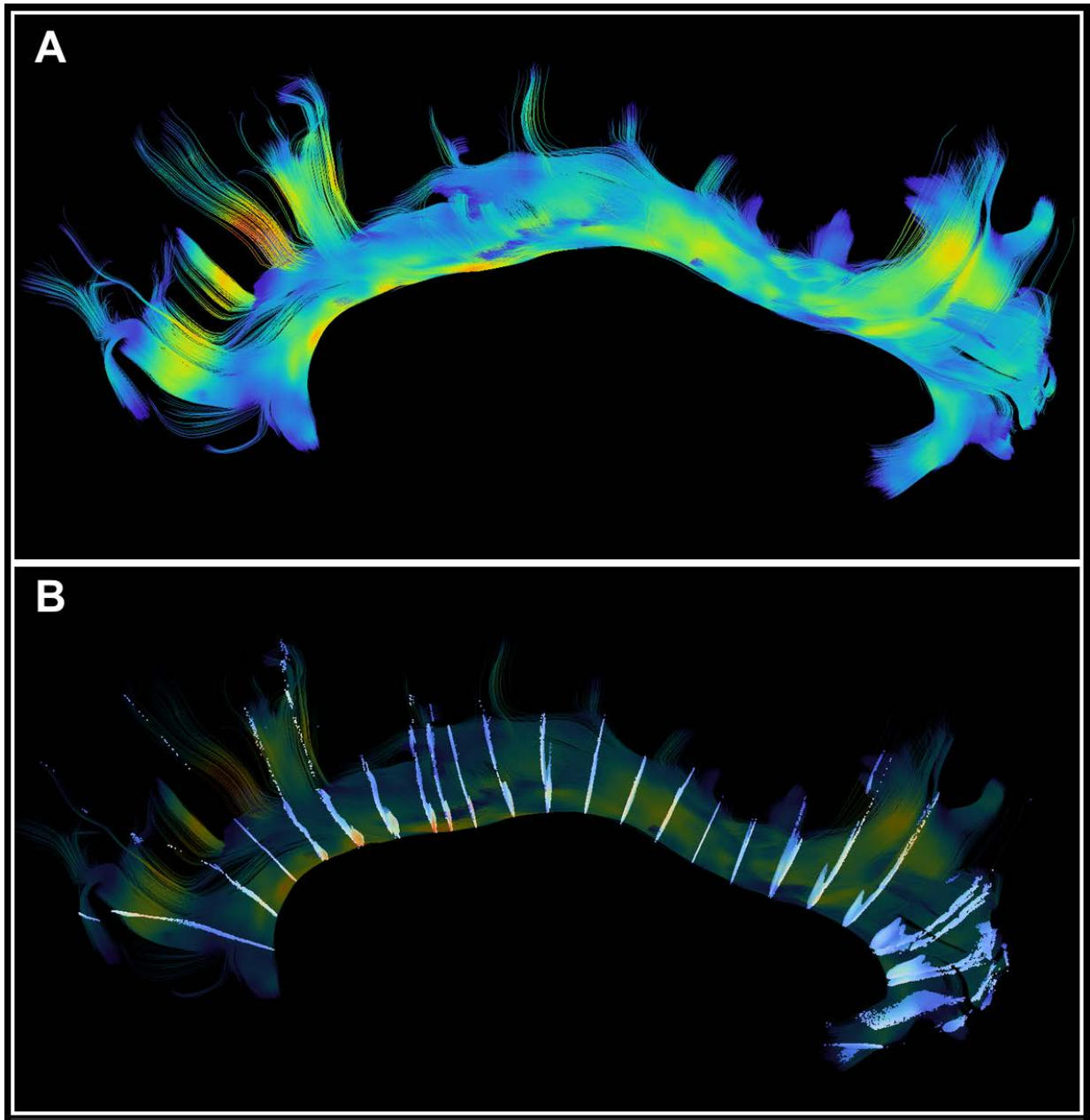
Figure 26. Estimation of dAV flux along fiber tracks. A) Voxel-wise dAV values are mapped onto the Cingulum Fiber Bundle. B) dAV flux is estimated by cutting the fiber bundle by orthogonal planes

4.5 DEMONSTRATION OF DAV METRIC ON SIMULATED AND HUMAN DATA SET

The proposed directional axonal volume method was tested on a simulated data set with known water content and directions of fiber populations. We used a diffusion spectrum imaging protocol to simulate diffusion weighted signals for each voxel. The fiber direction for each voxel was rotated accordingly. The axial and radial diffusivity constants is assumed to be 1.70×10^{-3} mm^2 s^{-1} and 0.30×10^{-3} mm^2 s^{-1} respectively for each voxel [226].

Simulated data was used to illustrate the dAV concept in case of a fiber divergence. We also showed mapping and profiling of dAV values on five major fiber bundle in a healthy human subject.

4.5.1 Simulated data set

A simulated data with known proton density and directional information in each voxel was created. This data represents a fiber bundle (100%) diverging into two fiber bundles equally. The original fiber bundle has 100% proton density in all voxels with the fiber direction pointing to the y-axis. Both divergent fiber bundles makes a 60° angle with y-axis and have half of the proton density.

4.5.2 Creation of simulated data set

Diffusion weighted images of size 12x9 voxel with two slices were simulated using diffusion spectrum imaging protocol; diffusion spectrum imaging protocol [48] is used in the simulation with 257 gradient directions, $\vec{g} = (\vec{g}_1, \vec{g}_2, ..., \vec{g}_{257})$ and $b_{max} = 7000$.

A "Y" pattern is created to simulate splitting (splaying) of a fiber bundle into two equal parts (see Figure 27). Proton density map reflects the amount of water content in each segments. The splitted segments have 50% water content (segment A and B in Figure 27) of the non-splitted segment (segment C in Figure 27).
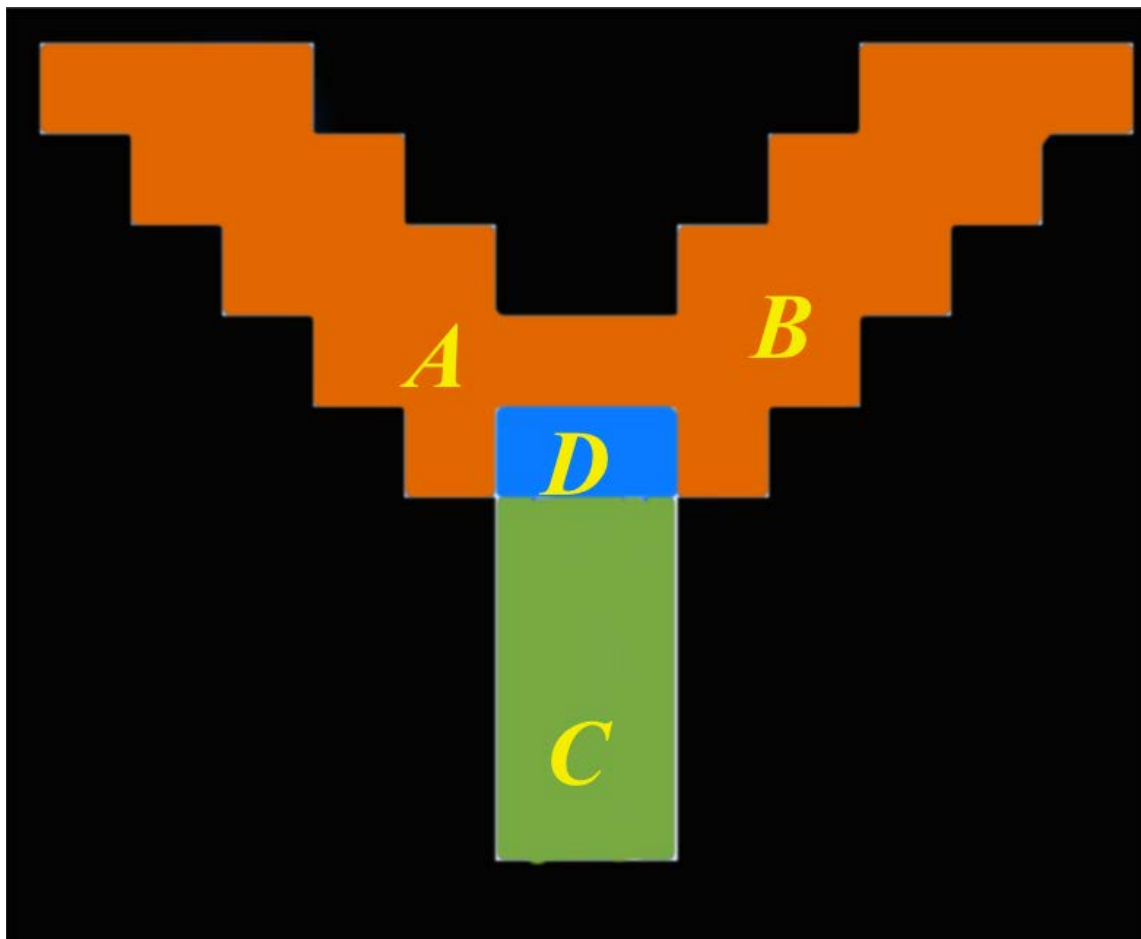
Figure 27. Simulated diffusion weighted imaging data set. Y-pattern shows fiber splitting.

For each voxel in "Y" pattern a fiber orientation and fiber volume fraction is assumed to simulated diffusion signals (see table 1).

Table 1. Diffusion weighted images are simulated with two fiber population. Parameters for each regions (see Figure 27) involved in simulation.

Segments	Fiber I			Fiber II		
	ϕ	θ	v	ϕ	θ	v
A	120	0	1.0	0	0	0
B	60	0	1.0	0	0	0
C	0	0	1.0	0	0	0
D	120	0	0.5	60	0	0.5

In a given voxel with fiber orientation (ϕ_i, θ_i), diffusion gradients g_i corresponding to b_i and volume fraction v_i of ith fiber population in a voxel, diffusion signals can be created using following equation,

$$\frac{S(\mathbf{g}_i, b_i)}{S_0} = \exp\left(-b_i \mathbf{g}_i^T R_{(\phi_i,\theta_i)}^T D_i \mathbf{g}_i R_{(\phi_i,\theta_i)}\right) \qquad (4.9)$$

where, D is the tensor matrix with the diagonal terms as longitudinal ($D_{\parallel}$) and transverse diffusivity ($D_{\perp}$), S_0 is the proton density map and $S(g_i, b_i)$ is the diffusion weighted signal corresponding to gradient direction g_i and b-vector b_i. Diffusion tensor model is used to demonstrate proton density weighting. In the future, a restricted diffusion model or a simulated diffusion model with given geometry can be used. In this simulation, $D_{\parallel}$ and $D_{\perp}$ are assumed to

be 1.70×10^{-3} mm^2 s^{-1} and 0.30×10^{-3} mm^2 s^{-1} for each fiber population respectively. The tensor matrix, D is rotated using the rotational matrix, $R(\phi_i, \theta_i)$ corresponding to each fiber orientation (ϕ_i, θ_i).

4.5.3 Results and discussion

In the simulate data set, the Directional Axonal Volume map in each of the two halves of the diverging fiber bundle shows half of the dAV value in the original combined bundle (see Figure 28 A and C). The estimated sum of the dAV values in the two diverging (green color in Figure 28) halves is equal to the estimated dAV map of original bundle (red color in Figure 28).
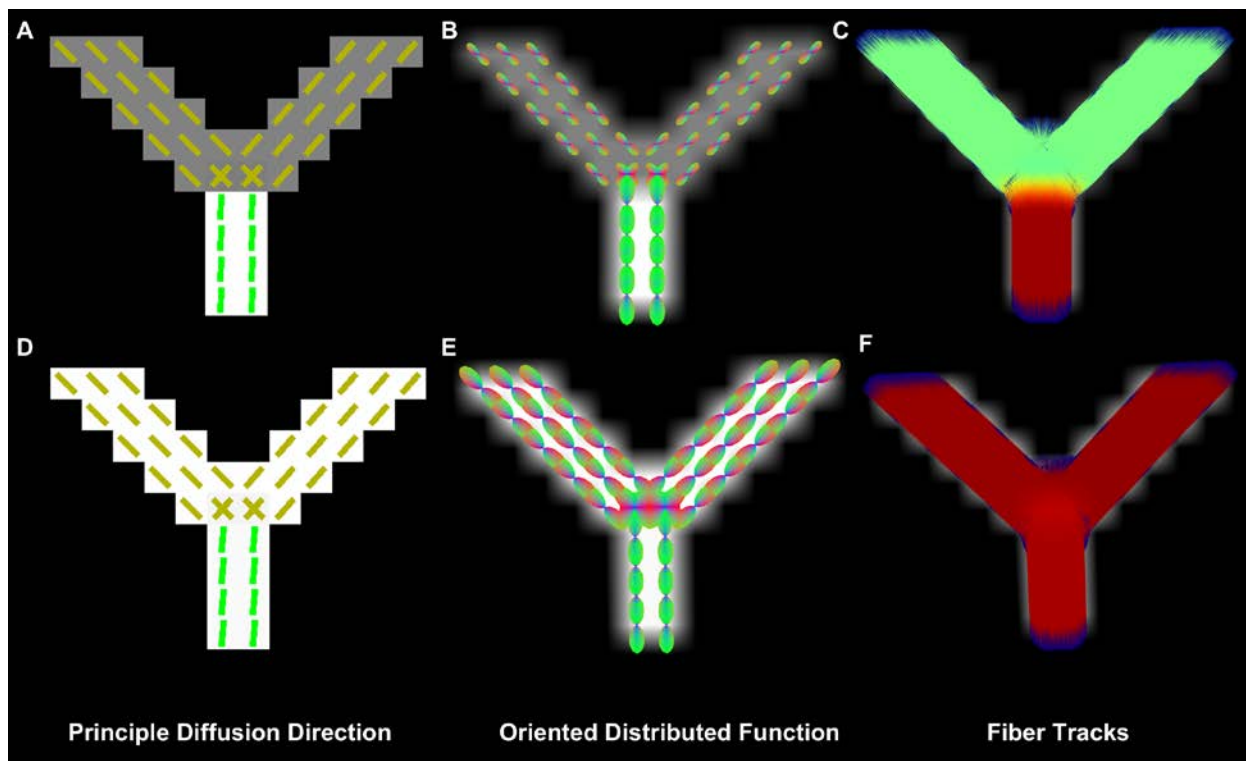
Figure 28. Simulated diffusion spectrum data of diverging fiber populations. A fiber bundle running along the y-axis diverges into two equal parts (splaying) at a 60 degree angle from y-axis.

The dAV effect will disappear if we normalize the diffusion weighted signal by the b = 0 image (see Figure 28 F). The ODF value is the same for each branch (see Figure 28 E). The important point to note here is that the geometrical information (direction of the fibers) is not affected in both scenarios (see Figure 28 A and D). A similar effect can also be illustrated on complex configurations.

Scalar metrics cannot account for the heterogeneity of water across voxels in the human brain. For example, fractional anisotropy (FA) has a value of 1.0 for all voxels except for the two crossing fibers (see Figure 28 A and D). It can't separate anisotropy for each fiber population and doesn't account for heterogeneity of total water content in each voxel.

4.6   HUMAN DATASET

4.6.1   MR Acquisition

MR images were collected on 3T Siemens Tim Trio with a 32 channel head coil with a whole body gradient $\|G\|_{max} = 40mT/s$ at the Magnetic Resonance Imaging Center (MRRC), University Of Pittsburgh. A diffusion spectrum imaging [48] scan with total of 258 diffusion weighted images, 257 gradient directions with $b_{max} = 7000 \ s \ mm^{-2}$ and one $b = 0$ with an axial echo-planar imaging readout (EPI) are acquired. Total time to acquire diffusion weighted images is 45 minutes. A fixed echo time of $TE=92ms$ and repetition time of $TR=3000ms$ is used for all diffusion measurements. A matrix of 96×96 is used over a field of view (FOV) of 224×224 mm for an EPI readout, which results in an isotropic voxel size of $2.4 \times 2.4 \times 2.4 mm^3$. A total of

63 axial slices are acquired over the whole brain. A high resolution T1 weighted image (10 minutes) is also acquired using an axial magnetization prepared rapid gradient echo (MPRAGE) sequence with $TR = 2110\,ms$, $TE = 2.63\,ms$ and a flip angle of $8°$. A total of 176 axial slices were acquired to cover the whole brain (see Figure 18 for raw images T1 and diffusion weighted images).

4.6.2 Directional Axonal Volume processing

Reconstruction of the fiber and diffusion ODFs was performed using the method specified in chapter two and chapter three. Both voxel-wise and tract-wise methods described in section 4.4 were developed and implemented in-house using MATLAB [135]. First, dAV was estimated for each voxel. Fiber peaks were estimated using the fiber ODF using the MRTrix software (MRTrix software [227]). These fiber peaks were then used to perform fiber tracking using DSIStudio [137] software. Five major tracts, Arcuate, Forcep major, Fornix, Cingulum and Uncinate, were segmented and dAV is mapped on to each tract. Arcuate and cingulum tracts was profiled to estimate dAV along tracts. DAV is mapped on the mean fiber and coefficient of variation was estimated for both arcuate and cingulum tracts.

4.6.3 Mapping dAV on fiber bundle

The dAV map was estimated for five major fiber bundles. Arcuate, Forcep major, fornix, cingulum and uncinate fiber tracts was reconstructed using DSIStudio [137] software. DAV values are then mapped according to the algorithm described in section 4.4 using MATLAB code. Fiber tracks are color coded with dAV values and are then visualized in TrackVIS [228]

software (see Figure 30 DAV values are constant along the fiber tracts (see orange color in Figure 30) suggesting that fiber pathways have same axonal mass. DAV values increase (see yellow color near the end of each tract in Figure 30) near the cortex due to the U-fiber bundles near cerebral cortex.

Arcuate and cingulum tracts were reconstructed using the fiber tracking algorithm described in [32]. First, a region of interest (ROI) was selected in DSI Studio, approximately located at the center of the arcuate tracts. ROI is manually drawn to select voxels in the core of the tract. A similar procedure is followed for the cingulum tract. A manually created ROI was then used to seed fiber tractography. 50,000 fibers were created for both arcuate and cingulum tracts. 5% - 10% of the computed fibers were trimmed to select tract of interest. Voxed-based dAV and segmented tract is then used to map dAV at each fiber points and profiled. For each profiled slice dAV values were estimated and mapped onto mean fiber.

DAV is estimated along the arcuate and cingulum by profiling both tracts (y-axis) and then plotted for each cutting plane (x-axis) see Figure 29 and 30. A coefficient of variation 15.97% and 17.53% was estimated using mapped dAV onto mean fiber tracts. Small variation of dAV along tracts show it is conserved along tracts.
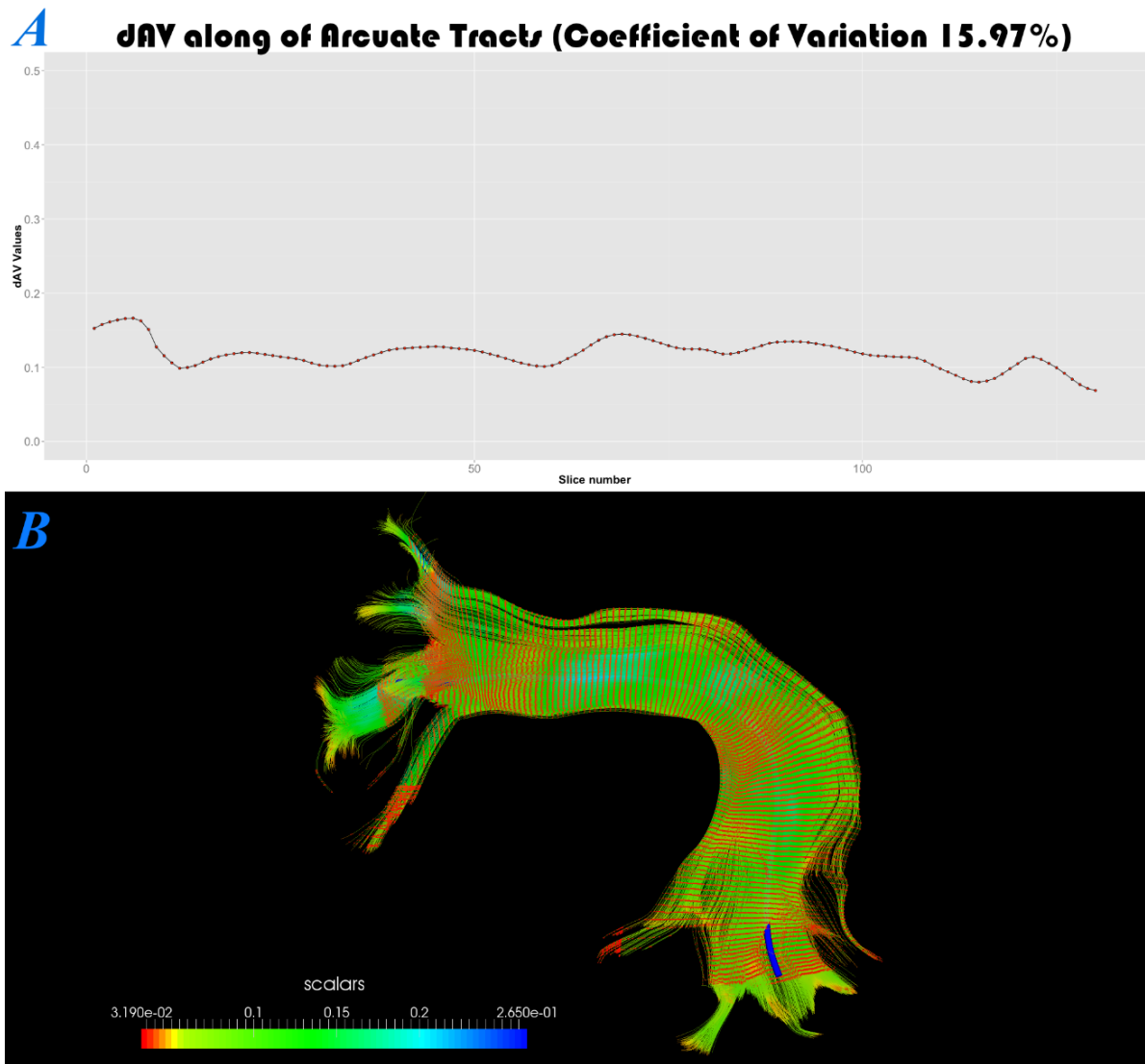
Figure 29. Mapping dAV and profiling of Arcuate tract.
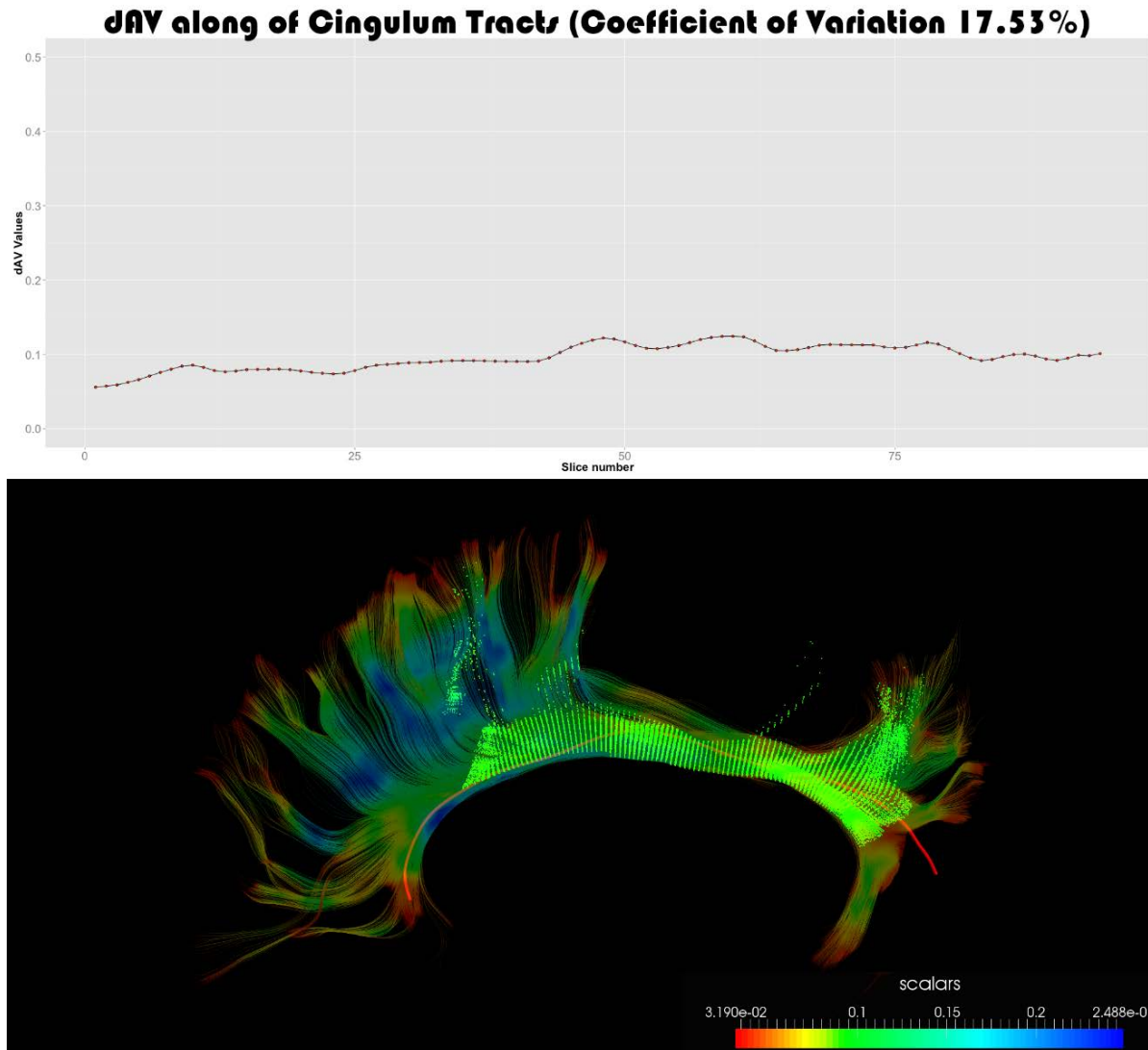
Figure 30. Mapping and profiling of Cingulum tract

This is a demonstration of the dAV mapping algorithm applied to the selected tracts. For more results and validation of dAV on a textile-based anisotropic phantom see chapter five.
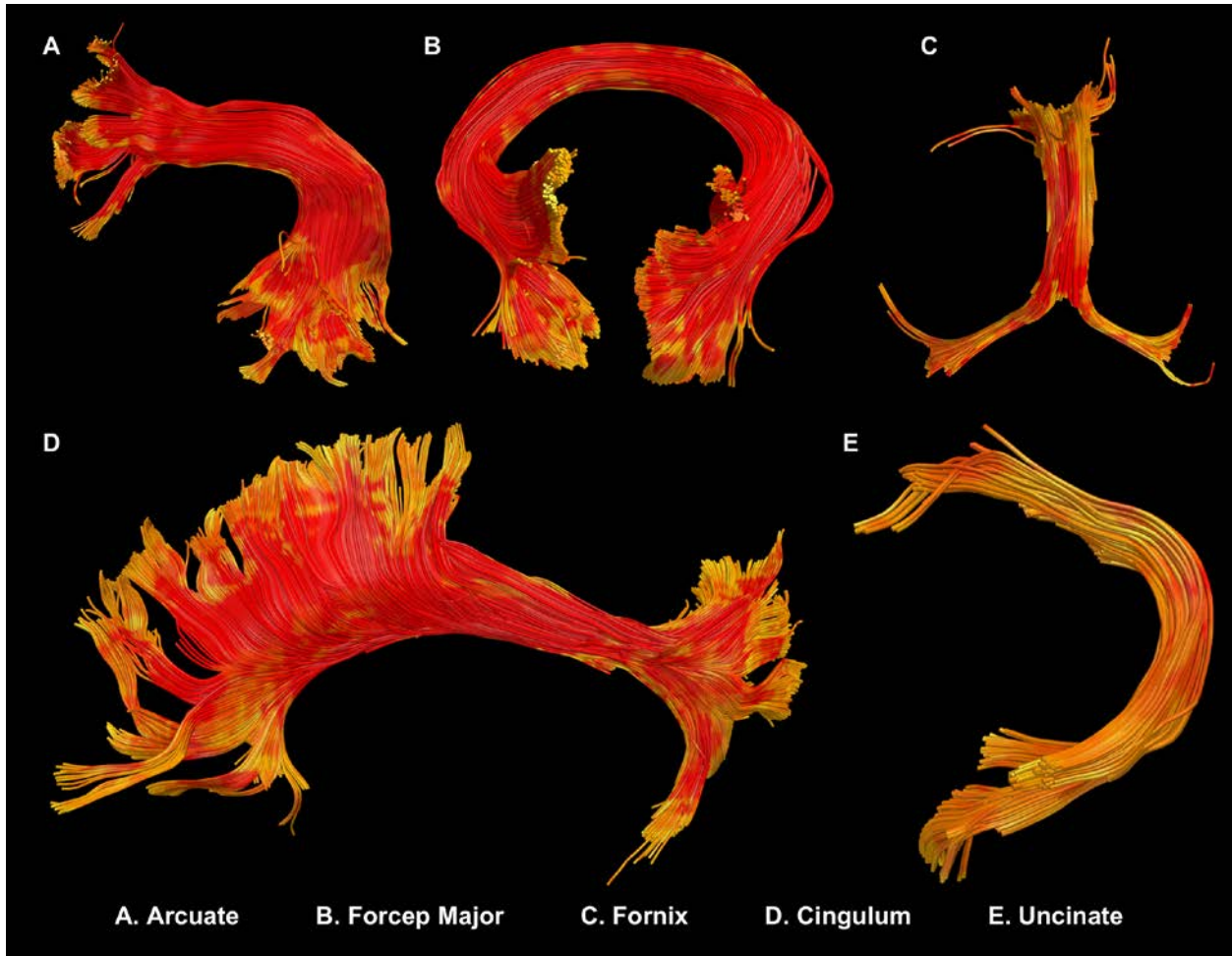
Figure 31. Tract-based dAV maps of five major fiber bundles in the human brain. The dAV maps show a constant value along fiber tracts suggesting that the directional axonal volume is constant for a given fiber population

We have also tested robustness of dAV metric with respect to number of fiber tracts created during fiber tractography. Cortico-spinal tracts (CST) was created using a varying number of tracts. Segmented tracts were then used to estimate total dAV for each version of CST. We have used 10,000 to 100,000 fibers for this test. Plot of dAV w.r.t. number of fiber shows convergence of dAV values after 4,000 fibers. 5.2% of coefficient of variation was observed in dAV values

(see Figure 32). This shows the robustness of dAV metric w.r.t. number of fiber tracts, which is a parameter in fiber tracking algorithms.
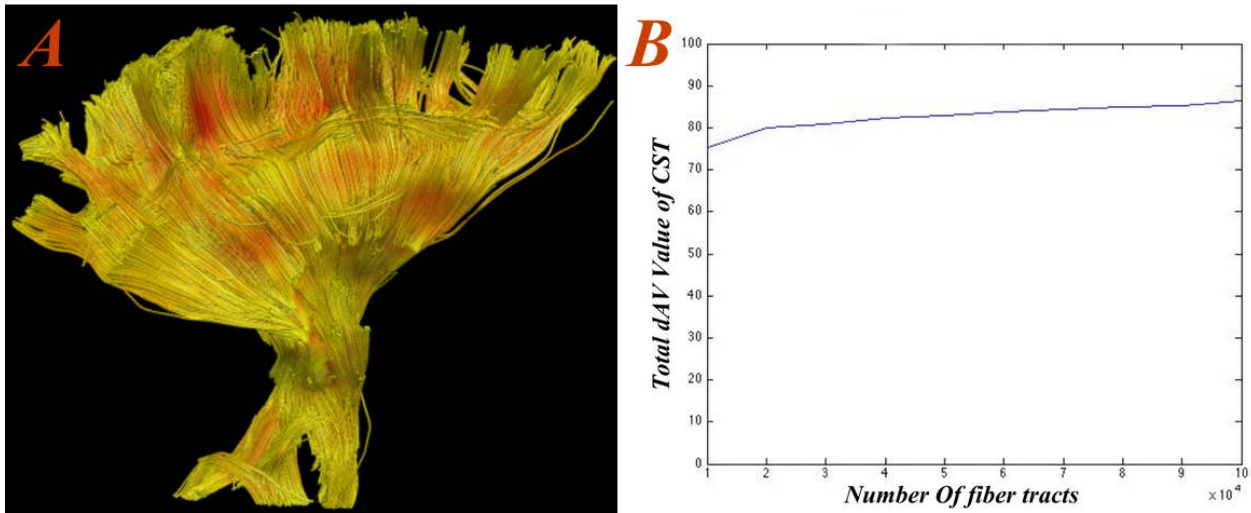
Figure 32. Total dAV value of CST versus number of tracts.

Although not shown in this chapter, dAV is sensitive to amount of underlying axons in white matter structure. In chapter five, we have tested this hypothesis on a textile based anisotropic phantom.

4.7   CONCLUSION

This chapter presented a novel metric to quantify anisotropy, directional axonal volume (dAV), which can resolved some of the limitations of scalar metrics like fractional anisotropy (FA). A voxel-based formulation of dAV was derived that accounts for the heterogeneity of water content across voxels. All scalar metrics normalize water content by dividing b = 0 in to all diffusion

weighted images. dAV solves disentanglement of anisotropy of crossing fibers. This chapter derived an algorithmic framework to map anisotropic values onto fiber bundles. In the case of crossing fibers, this algorithm only maps anisotropic values in the direction of each fiber. It does not mix anisotropy from different fiber populations.

Tract-based dAV metric is demonstrated on a arcuate and cingulum tracts. Profiling of arcuate and cingulum tracts showed robustness of dAV metric. A coefficient of variation (approximately 16%) was observed for fiber tracts. We have also shown that dAV is insensitive to number of fibers set in fiber tracking. This makes dAV a powerful technique to study structural connectivity between functional regions. DAV mapped along the fiber could potentially be used to localize fiber damage in pathological brains. Chapter five will show the use of a textile based anisotropic phantom for the validation of the dAV metric.

4.8   LIMITATION AND FUTURE EXTENSIONS

There are three limitations to the dAV metric proposed in this chapter that will be addressed in future extensions. One of the major limitations of the dAV based metric is that it suffers when two parallel fiber populations pass through the same location (voxel). DAV successfully measures the "volume" of all coherent (same direction) fibers passing through a voxel. This set of coherent fibers may not, however, belong to the same functional fiber bundle. For example, regions near the cortex have U-fibers parallel to association fibers or projection fibers (e.g. cortico-spinal tract) that will both contribute to the dAV components. While the dAV metric correctly estimates anisotropy in voxel, it would be more useful to separate anisotropy not only by direction but also by functional bundle. A future extension will resolve this by subtracting

dAV values from the other sets of the fiber bundles. A second limitation comes from MR in-homogeneity of signal near the cortex as compared to signal in the deep brain due to the fact that the receiver channels are nearer to the cortex. This will overestimate the proton density map and thus can be reflected in the dAV estimation near the cortex. This issue can be resolved by a separate scan that maps signal decay as we move away from the head-channel coil. A third limitation is related to calibration of water content. A known reliable water content source is needed for calibration of the estimated proton density. Regions (voxels) within the scan object/tissue, can serve as a reference. In chapter five we will present a textile-based anisotropic phantom to overcome some of these issues.

5.0   PHANTOM BASED VALIDATION

5.1   INTRODUCTION

Chapters one through four in this thesis provide a mathematical formulation for diffusion processes in white matter tissue. This chapter focuses on the validation of these methods through known ground truth in controlled MRI experiments. These diffusion models and validation frameworks can be utilized in clinical and neuroscience research. This chapter presents use of a novel Textile Anisotropic Brain Imaging Phantom (TABIP) that has a manufactured microstructure of textile fibers called TAXONS to address the following hypotheses:

1. Diffusion imaging techniques can be utilized to visualize anisotropy and orientation of microstructure in the phantom.

2. Diffusion patterns estimated from diffusion MRI in a voxel can resolve underlying taxonal crossing.

3. The diffusion MRI derived anisotropic metric is sensitive to taxon quantity.

In order to test these hypotheses the TABIP was scanned at two different sites: Children's Hospital in Pittsburgh and Massachusetts General Hospital (MGH) in Boston. The TABIP simulates different compartments as free, hindered, and restricted water, which are unique

features to test biophysical models like CHARMED [41, 103] NODDI [39], DIAMOND [229], AxCaliber [42] etc. The phantom can be configured to different crossing patterns in order to also test fiber tracking methods.

In this study various methods are used to address these hypotheses, namely, three reconstruction algorithms: diffusion tensor imaging [68, 202] (DTI), generalized q-sampling imaging [36] (GQI), the reconstruction algorithm proposed in chapter two of this thesis, and two quantification methods: directional axonal volume (see chapter four), and Neurite Orientation Dispersion and Density Imaging (NODDI) [39].

5.2   BACKGROUND

5.2.1   Imaging Phantoms

Phantoms are used in imaging experiments to provide a ground truth (**gold standard**) for various mathematical imaging models [186, 230-233]. Imaging phantoms are also used to evaluate, analyze and test the performance of imaging systems [72, 73, 234-236]. Phantoms can provide a manufactured consistency and a non-MR based measurement of diffusion paths that are stable, which is impossible to achieve with living or cadaver tissue. For example, we can control the number of taxon tubes, packing density (amount of hindered water), crossing geometry, tube diameters, and presence or absence of water inside or outside the tubes. The textiles are stable for months, potentially years (studies ongoing), and the phantom may allow for repeated testing longitudinally for a single scanner or across scanners, vendors, pulse programs, and post processing routines. Also since the phantom has no physiological noise (movement, respiration,

heart beats), we can examine measurements without these noise components. It can also be scanned for long sessions allowing for comprehensive mapping and testing of acquisition parameter spaces.

There has been a long history of using phantoms in magnetic resonance based imaging experiments. MR phantoms are used for evaluation and calibration of multi-modal MR signals from various MR sequences. In 1973, Paul Lauterbur (Father of MRI) described the use of an MR phantom in his first Nature publication Lauterbur [25]. He demonstrated proof of concept by showing 2D images of two micro-tubes of H_2O in a background of D_2O. Later, he ~~also~~ introduced magnetic resonance imaging (also called zeugmatography) and established that it could produce three-dimensional MR images. He also showed that isotopic exchange could be visualized using MRI. This capability allowed for the imaging and measurement of water diffusion. In order to show this, he used the same two-capillary setup as shown in his Nature paper [26, 237]. Further, he used a biological example, a parsley stem, to image diffusion.

Many MR centers use phantoms for testing scanner performance and to validate MR derived metrics [238, 239]. A formal testing mechanism and validation framework are needed for reproducibly and reliability of the MR metrics [240, 241]. There are two organizations that provide phantom and reliability testing for the quantification of MR metrics: The American College of Radiology and The Quantitative Imaging Biomarkers Alliance.

The American College of Radiology (ACR) [73, 238, 242] has an MRI accredited program [243] for phantom scanning. This program has seven quantitative tests for the measurement of digital data:

1. Geometric Accuracy
2. High-contrast spatial resolution

3. Slice thickness accuracy

4. Slice position accuracy

5. Percent-signal ghosting

6. Image intensity uniformity

7. Low contrast object detectability

Each test provides the quantitative and qualitative assurance of MR images and also gives proper guidelines to correct them in case of failure.

The Quantitative Imaging Biomarkers Alliance (QIBA) [239] on the other hand provides various phantom tests and guidelines to develop and insure consistent, reliable, valid, and achievable quantitative imaging biomarkers. Their goal is to achieve reproducible quantitative results from imaging methods for multi-vendor, multi-site, and test-retest phantom assessments. For details see [24, 71, 244].

5.2.2 Diffusion Phantoms

Diffusion phantoms are specially designed to evaluate the performance of diffusion imaging sequences and various mathematical models for diffusion as well as the metrics derived from these models [74, 94, 245]. Primarily, diffusion phantoms are used to estimate the known diffusivity constant of various liquids [246]. These phantoms measure the directionally independent (isotropic) diffusion properties of material/tissue and thus fall into category of isotropic phantoms.

Geometrical phantoms on the other hand are used to access the directionally dependent (anisotropic) diffusion properties of the underlying material. They are used to access underlying geometrical information (fiber direction) and to quantify properties of diffusion along a principle

direction(s) (fiber direction). These phantoms can also be used to simulate multiple diffusion compartments (free, hindered and restricted) with complex geometrical arrangements. A restricted compartment, for example, would depend upon the phantom being constructed from solid or hollow tubes. Various materials are used to build fibers with known diffusion properties similar to those of living tissue. Both biological materials and synthetic materials are used to create fibers. Biological materials such as fibrous vegetables (e.g. bamboo stems) are good candidates for building these fibers. To simulate a restricted compartment, glass capillaries with 10-90 μm as the inner diameter have been used [247]. Although glass capillaries have the advantage of a restricted diffusion compartment, it is hard to make complex geometric patterns with them. Other materials, such as cloth tape [248], silk [249], wood [250], and glass fiber cord [251] are also used to create fibers. Glass capillary-based phantoms provide diffusion tubes of a known size to estimate the compartment size with a high q-values scan. Komlosh et al [209] shows that an angular double PGSE sequence can be used to extract the dimensions of a confined geometry, even at low q-values [194, 208, 209].

Currently, the field of diffusion MRI lacks a ground truth standard that can be used to validate diffusion models for the microstructure of tissue. Many attempts have been made to create a phantom simulating diffusion patterns using biological and synthetic fibers as describe above.

In this study, we are utilizing the Taxon Anisotropic Brain Imaging Phantom (TABIP) created by Psychology Software Tools [76] that can address some of the shortcomings of current diffusion phantoms. This phantom uses hollow fibers with known inner and outer diameters made up of textile strands (Taxons). Taxons simulate restricted diffusion compartments with configurable volume fractions and orientations. The TABIP can be configured to provide

different packing densities with varying crossing angles between taxonal bundles. It has the potential to simulate white matter damage and fiber loss and can provide insight into quantifying traumatic brain injury and other neuro-degenerative diseases. It can be used as a ground truth standard for validating diffusion models in micro-tissue. The TABIP used for this thesis is one of the first textile phantoms manufactured by PST; more validation and testing of these phantoms are planned in near future.

5.2.3   Modeling and Quantification

The implicit assumptions in the construction of a geometrical phantom are:

1. It should provide a ground truth for connectivity strength, which can be related to anisotropic metrics derived from diffusion models.

2. It should provide a ground truth for complex geometrical patterns, which can be resolved through diffusion modeling.

These characteristics of a geometrical phantom can be achieved by creating complex geometrical patterns like crossings at different angles, kissing, merging and diverging of fiber bundles in combination with different volume fractions of free, hindered, and restricted compartments.

Various diffusion reconstruction algorithms and corresponding fiber tracking methods [75] are used to describe the underlying diffusion pattern in tissue and phantoms. Each of these methods has advantages and disadvantages in terms of complexity and stability of numerical solution. A phantom with solid fibers [70, 75] has been used to compare multiple diffusion models to test their accuracy in resolving crossings. This phantom was also used in the FiberCup Challenge [75] to test these reconstruction methods in fiber tractography. The important difference between the FiberCup phantom [75] and the TABIP used in this study is the presence of restricted

110

compartments in TABIP, which makes it ideal for biophysical diffusion models such as NODDI [39], CHRAMED [41], and AxCaliber [42].

In this study we are testing two quantification frameworks: dAV and NODDI. DAV provides quantification of the anisotropic components along the fiber tracts. NODDI estimates isotropic, extra, and intra cellular water content for each voxel.

Diffusion models are also used to resolve fiber crossings in a voxel. Accurate representation of fiber crossings is crucial in delineating fiber bundles in the human brain. All diffusion models (or all mathematical models) have variable sensitivity. For example some diffusion models can detect $90°$ but not $30°$ crossings.

In this study we test three reconstruction methods, namely, diffusion tensor imaging [68] (DTI), generalized q-sampling imaging [36] (GQI) and the proposed reconstruction algorithm discussed in chapter two, and evaluate their sensitivity to resolve three different crossing patterns. This will identify the "viable accurate range" for each of the reconstruction methods as well as their potential limitations.

5.2.4 Hypotheses

The TABIP is scanned at two sites to test the three hypotheses below:

1. **Anisotropy** This hypothesis tests that diffusion MRI can image a taxonal bundle of the TABIP. Diffusion derived metrics such as fractional anisotropy (FA), mean diffusivity (MD), axial diffusivity (AD), radial diffusivity (RD), and apparent diffusion coefficient (ADC) are estimated for each bundle and compared with the same metrics in standard human brain scans.

2. **Resolving Crossings** To correctly resolve the complex geometrical patterns of white matter pathways in the human brain, The TABIP provides $30°, 45°$, and $90°$ crossing patterns. This hypothesis tests that diffusion reconstruction methods can resolve fiber crossing patterns with $30°, 45°$, and $90°$ angles using three reconstruction algorithms: DTI, GQI and the proposed reconstruction method in chapter two.

3. **Number of Taxons** Another key goal of diffusion MR imaging is to quantify axonal bundles volume in the human brain. Quantification of axonal bundles is crucial for longitudinal studies in neuro-degenerative diseases such as Huntington's disease [14], Parkinson's disease [34], and ALS [17]. Even for basic neuroscience, this type of quantification can help in identifying axonal changes in the human brain [252, 253]. This hypothesis tests that diffusion derived anisotropy metrics can predict tract reduction and compression within a given volume. These metrics are compared with the "ground truth" phantom, which will have different manipulations of tract size reduction, tract compression, and increasing isotropic water volume.

To test this, the TABIP provides five cylindrical tubes with a known number of taxons. The volume of each tube is constant. Taxon packing densities of $20\%, 40\%, 60\%, 80\%$ and 100% are used to simulate axonal loss patterns. Packing density is also changed along the tube by compression while keeping the number of taxons in the tube constant.

5.3   MATERIAL AND METHODS

5.3.1   Design of Phantom

PST created a hollow textile phantom, which can simulate hindered and restricted water compartments[1]. It is made of material used in polypropylene textiles; filling was performed by pressure filling each of the bundles and verifying the fill rate via microscope and visual inspection of each fiber. Each of the hollow fibers have an outer diameter of 35 micron and an inner diameter of 12 micron. Crossing tracts were made of 2.5 mm by 10 mm ribbons of fibers. The fibers were filled with distilled water internally and externally.

5.3.1.1 Crossing

The crossing fixture was 3D printed out of Visijet M3 Black, and affixed to the disk with $8-32$ PEEK screws. The crossing fixture was comprised of three different bundles, two straight and one crossing bundle. The central straight portion where the crossing bundle weaved through had a void size of $7.5mm \times 5mm$. The void surrounding the crossing bundle was $2.5mm \times 5mm$ to allow for compression. The fill rates and number of fibers of the crossing fixture are outlined in this table:

---

[1] I have no financial conflict of interest (COI) issues relating to the phantom. I note that Dr. Schneider does have equity in the company that produces the phantom. That potential for COI is declared and the management plan of any conflict is reviewed annually by the University of Pittsburgh COI office and the Dean of the Kenneth P. Dietrich School of Arts and Sciences. It is also reviewed by the Department Chair of Bioengineering, Dr. Sanjeev Govind Das Shroff.

Table 2. Percentage of water filled for packing density and crossing pattern.

Fiber Bundle	Number of Fibers	Filled Percentage
Straight 1	14080	80.22
Straight 2	14080	77.23
Crossing	14080	78.81

5.3.1.2 Packing Density

The materials were selected to be non-RF reactive, stable in water, and for ease of machining. The outer shell was composed of acrylic, and then solvent glued to the acrylic base. An acrylic cap was affixed with nylon $0.25" - 20"$ screws to the base. Supports were machined out of polycarbonate rods and used to position the disks. The supports were threaded into the acrylic cap. The disks were machined out of polycarbonate and held to the supports by polycarbonate $0.25" - 20"$ machine screws. The density fixture was 3D printed out of Visijet Crystal, and affixed to the disk with 8-32 PEEK screws. The density fixture comprised five different sized bundles, which were percentages of the full 5×5 mm bundle. Each bundle had four stages of compression: $1 \times, 1.5 \times, 2.5 \times$ and $3 \times$. The dimensions and fill rates are outlined in table below.

Table 3. Fill rate in packing density pattern

	Number of Fibers	Fiber Filled Percentage	Compression Region	Void Side (mm²)
Density Fixture				
	28160	76.19	1	5.00
			1.5	7.50
			2	10.00
			3	15.00
	22528	78.39	1	4.47
			1.5	6.71
			2	8.94
			3	13.42
	16896	78.39	1	3.87
			1.5	5.81
			2	7.75
			3	11.62
	11264	77.06	1	3.16
			1.5	4.74
			2	6.33
			3	9.49
	5632	81.49	1	2.24
			1.5	3.35
			2	4.47
			3	6.71

5.3.2   MR Acquisition

The TABIP was scanned at two different sites, Children's Hospital in Pittsburgh and Massachusetts General Hospital (MGH) in Boston. Children's Hospital has a 3T Trio MR Siemens system with a whole body gradient $\|G\|_{max} = 40mT/s$ and a 32 channel head coil. Three shells are acquired using a multi-band spin echo diffusion weighted pulse sequence [124] with an axial echo-planer imaging readout (EPI). A multi-band acceleration factor of 3 is used to accelerate scanning time. Different b-values, $b = 1000/3000/5000s/mm^2$, are acquired with a fixed echo time *TE=92ms* and repetition time *TR=3000ms* for all measurements. A matrix of 96×96 is used over a field of view (FOV) of 224×224 for an EPI readout, which results in an isotropic voxel size of $2.4 \times 2.4 \times 2.4mm^3$. A total of 63 axial slices are acquired over the whole phantom. For each shell, a non-weighted (b = 0) diffusion image is acquired every tenth b-value acquisition. 64 diffusion-weighted images for each shell are acquired with non-collinear gradient directions sampled uniformly on a unit sphere. The total time for this acquisition was 16 min (14 min for b = 1000, 3000 and 5000 shells). A high resolution T1 weighted image is also acquired using an axial magnetization prepared rapid gradient echo (MP-RAGE) sequence with $TR = 2110\,ms$, $TE = 2.63\,ms$ and flip angle 8°. A total of 176 axial slices were acquired to cover the whole phantom.

The second scan was performed on the 3T Connectome scanner [254] at Massachusetts General Hospital (MGH) in Boston. This is a unique scanner with custom built gradients, which can reach to gradient strength of $\|G\|_{max} = 300mT/s$. A 128-channel head coil is used to scan the phantom. High gradients allow scanning with very high b-values and high spatial resolution. Ten shells were acquired using a spin echo diffusion weighted pulse sequence with axial echo-planar

imaging readout (EPI). Different b-values, $b = 1000, 2000, \cdots, 10,000 \ s / mm^2$, are acquired with a fixed echo time of TE = 80 ms and a repetition time of $TR = 8000 ms$ for all measurements. A matrix of 90×90 is used over a field of view (FOV) of 180×180 mm for the EPI readout, which results in an isotropic voxel size of $2.0 \times 2.0 \times 2.0 \ mm^3$. A total of 68 axial slices are acquired over the whole phantom. For each shell a non-weighted (b = 0) diffusion image was acquired every tenth b-value acquisition. 128 diffusion-weighted images for each shell are acquired with non-collinear gradient directions sampled uniformly on a unit sphere. The total time for this acquisition was 184 min (18.4 min per $b = 1000, 2000, \cdots, 10,000 \ s / mm^2$ shells). High resolution T1, T2, and Proton density MR images were also acquired. A high resolution T1 weighted image was acquired using an axial magnetization prepared rapid gradient echo (MP-RAGE) sequence with $TR = 2530 \ ms$, $TE = 1.15 \ ms$ and flip angle $7°$ with 176 axial slices, scan time 6.02 minutes, a T2 weighted image was acquired with $TR = 3200 \ ms$, $TE = 561 \ ms$ with 256 axial slices, scan time 6.48 minutes, and a proton density image was acquired with $TR = 4.3 \ ms$, $TE = 1.82 \ ms$ and flip angle $5°$ with 256 axial slices, scan time 5.52 minutes.
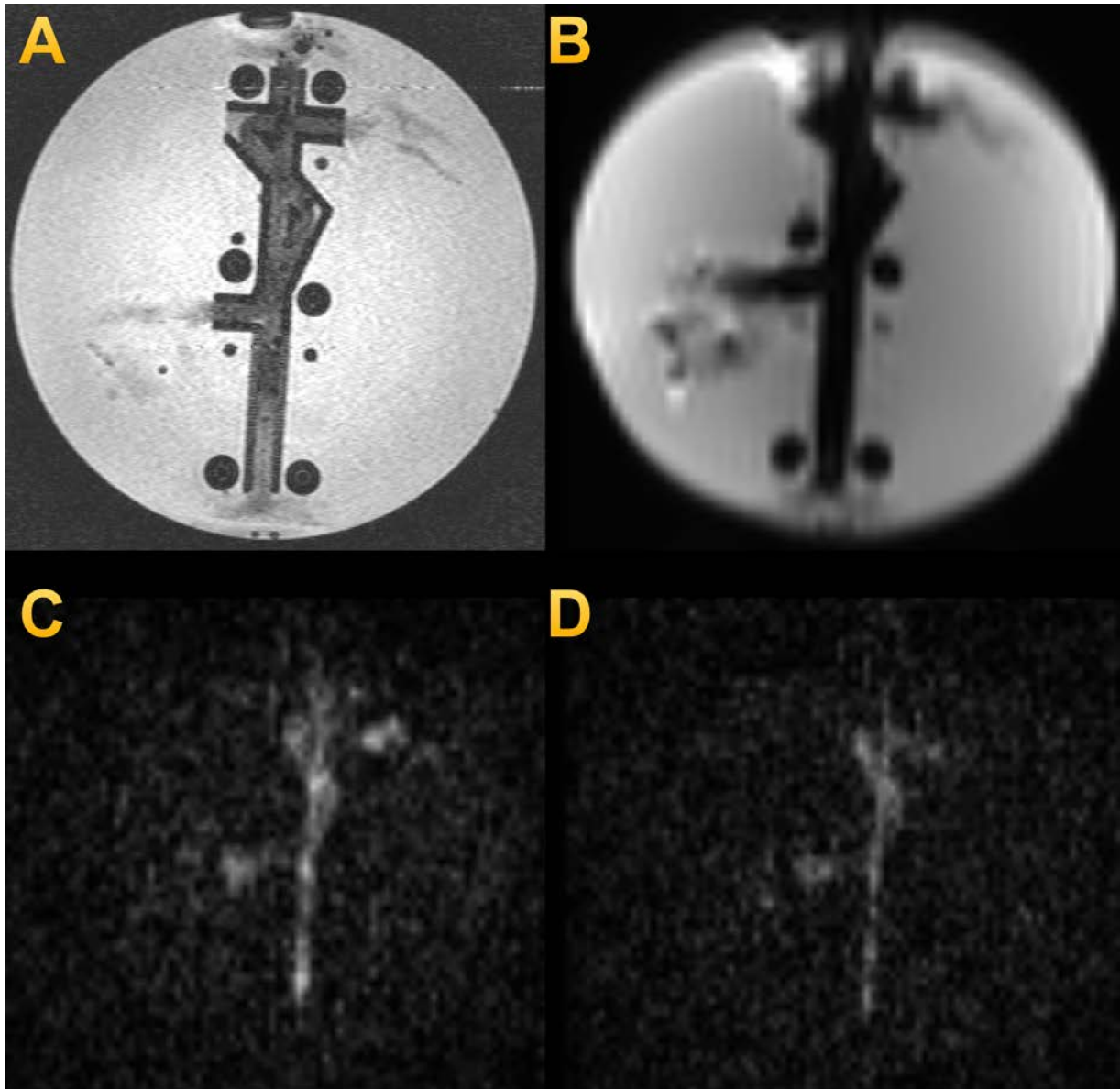
Figure 33. Axial slice of the crossing pattern. (A) T1 images. (B), (C) and (D) show b = 0, 3000 and 5000 diffusion weighted images.
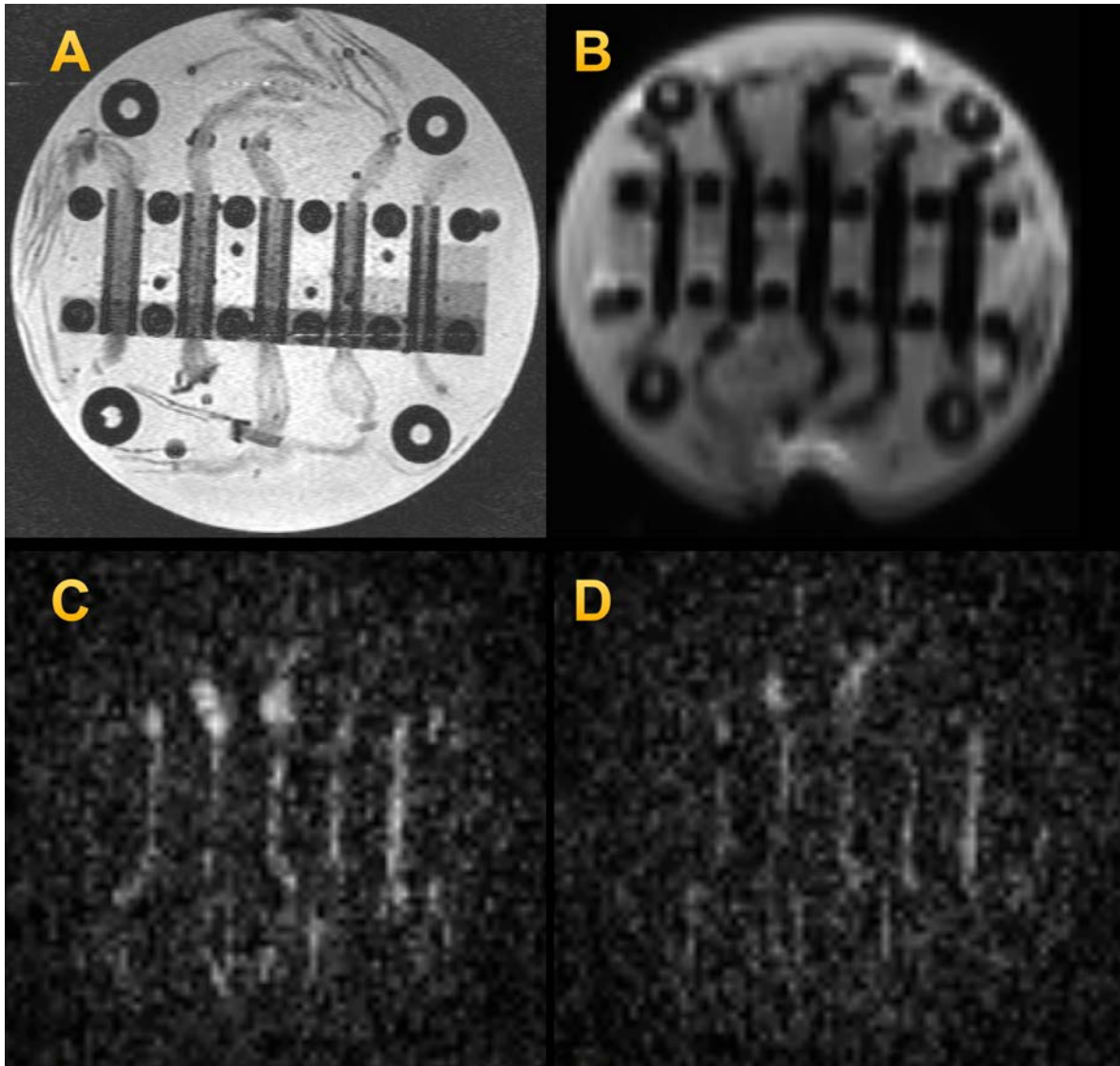
Figure 34. Axial slice of packing density pattern. (A) T1 images. (B), (C) and (D) show b = 0, 3000 and 5000 diffusion weighted images.

5.3.3 Structural Image Processing

The T1 image of the phantom was visualized using the MRICroGL volume rendering software [255]. Volume rendered T1 images are sliced axially to visualize different segments (number of taxons and crossing patterns) of interest. Axial cuts though these segments clearly show three

$(30^\circ, 45^\circ, 90^\circ)$ crossing patterns and density patterns with five equal volume chambers with varying amount of fiber, $20\%, 40\%, 60\%, 80\%, 100\%$ (see Figure 35). Regions of Interest (ROIs) were created in T1 image space using FSL's fslview [138] package. These ROIs were then transformed to diffusion space (b0-space) using FSL's Flirt package [256, 257]. These ROIs were used to estimate anisotropic metrics and taxonal crossing angles.
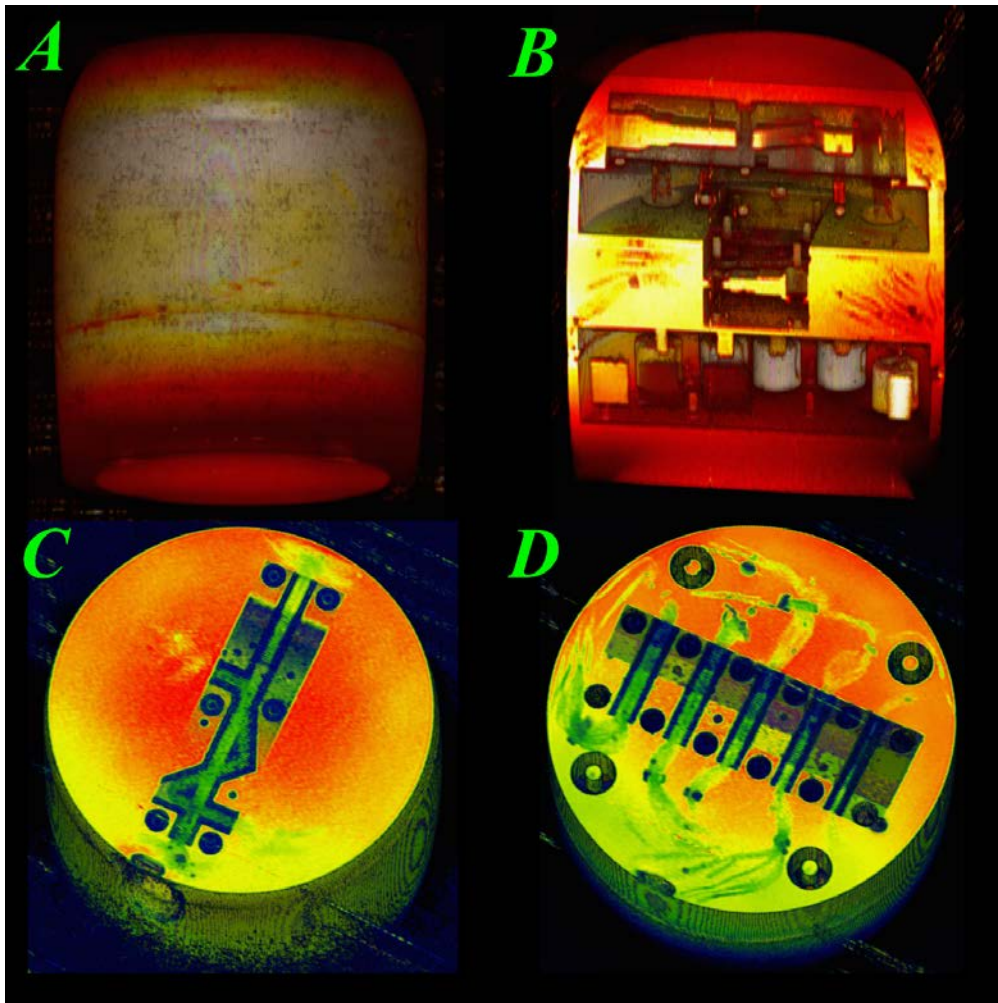
Figure 35. Volume rendering of textile phantom. It shows internal structures such as the crossing pattern and different packing densities. (A) Outer surface of Phantom. (B) Vertical cross-section shows different chambers. (C) Horizontal sections at crossing pattern. $30^\circ, 45^\circ, 90^\circ$ Crossing angle are shown. (D) Five equal volume chambers with fiber density of $20\%, 40\%, 60\%, 80\%, 100\%$.

5.3.4 Diffusion Reconstruction Methods

Diffusion reconstruction algorithms are used to test hypotheses 1 and 2. The diffusion tensor and its derived metrics are used for hypothesis 1, and GQI and the proposed reconstruction algorithm in chapter two, and the resulting fiber tractography are used to test hypothesis 2.

5.3.4.1 Diffusion Tensor imaging

Diffusion Tensor analysis is performed on both multi-shell diffusion data sets using FSL's *dtifit* package [118, 139] on each shell using a least squares estimation method as described in chapter two. Fractional anisotropy, mean diffusivity, and radial and axial diffusivity are estimated for each of the ROIs. Three eigenvalues and eigenvectors are estimated by performing eigenvalue decomposition using FSL's dtifit package [118, 139]. The orientation of the taxonal bundle is visualized in each voxel by mapping the principle diffusion direction onto the red, green and blue color channels. The green fiber bundle is parallel to the y-axis, the red fiber bundle shows a 90° crossing angle and yellow shows a 45° crossing angle in Figure 36.
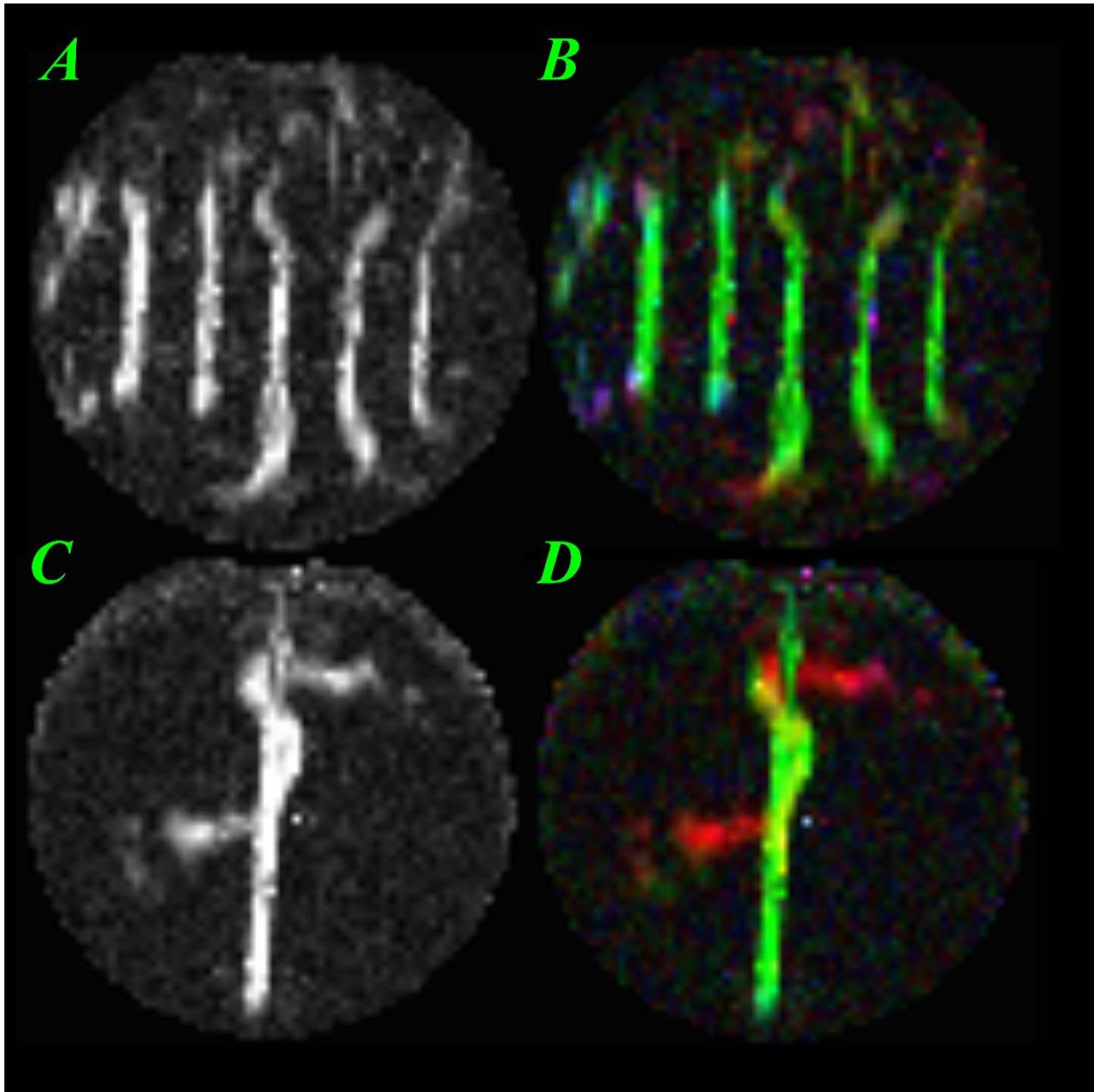
Figure 36. Fractional Anisotropy map and directional color encoding of a horizontal slice of the Crossing and Packing density patterns. (A) Fractional anisotropy map shows high intensity values for voxels containing textile fibers. (B) Color encoded principal diffusion direction. One fiber is running across the phantom and the other bundles are crossing it at $30^{°}, 45^{°}, 90^{°}$ angle. (C) Fractional anisotropy map of the packing densities. (D) Color encoded principal diffusion direction of the packing density pattern. Mid sections of the fibers are packed in different chambers. Fiber chambers are created with same volume and different ($20\%, 40\%, 60\%$, $80\%, 100\%$) numbers of fibers.

5.3.4.2 Generalized Q-sampling imaging

Generalized Q-sampling imaging [36] (GQI) was performed on multi-shell (both data sets) diffusion weighted images to create diffusion ODFs for each voxel as described in chapter two. Diffusion ODFs are functions on a sphere and were reconstructed at discrete spherical points uniformly distributed on a unit sphere. We used 362 discrete spherical points for all ODF calculations. A value of 1.2 mean diffusion distance [32, 36] was set for GQI reconstruction in the DSI Studio software [137] (see Figure 37).
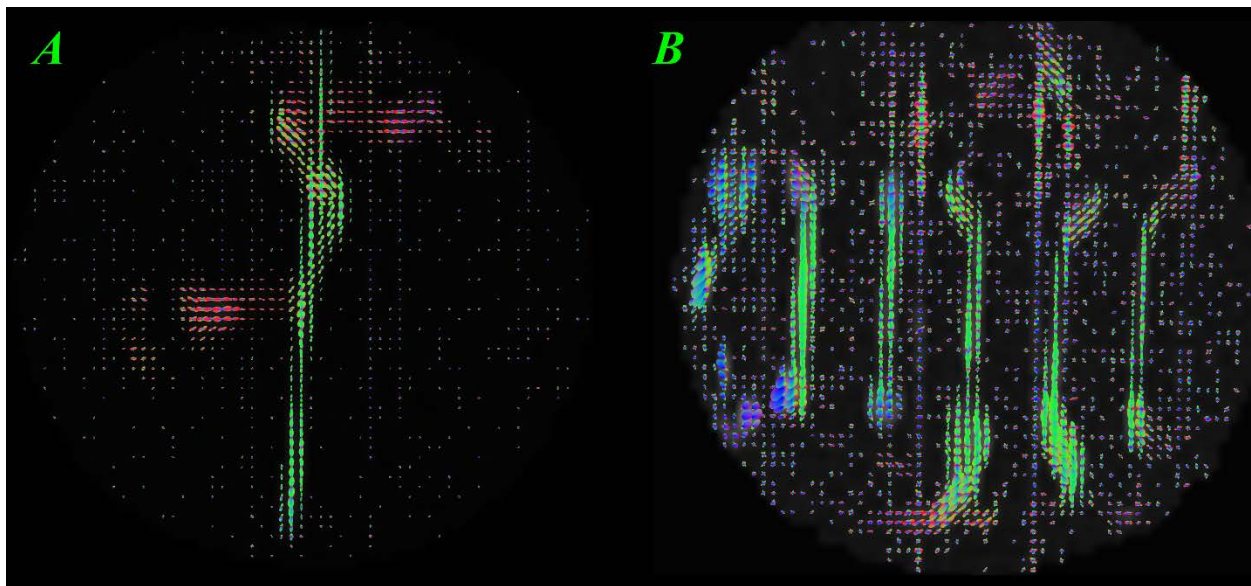
Figure 37. Horizontal slice of the crossing pattern with diffusion ODFs reconstructed using GQI.

5.3.4.3 Proposed Reconstruction Algorithm

Spherical harmonics coefficients of diffusion ODFs were estimated using the proposed reconstruction algorithm described in chapter two. After estimation of spherical harmonics coefficients of diffusion ODFs, constrained spherical deconvolution is performed to estimate the spherical coefficients of fiber ODFs as described in chapter three (see Figure 38). The response function for deconvolution is estimated from voxels with a fractional anisotropy greater than 0.7.

Peaks of the fiber ODFs are then estimated by finding the maxima on a sphere using MRtrix [37, 38]. These peaks are further used to compare known crossing patterns and to perform fiber tracking. Proposed reconstruction, generalized q-sampling reconstruction and dAV related calculations are performed using in-house MATLAB [135] functions.
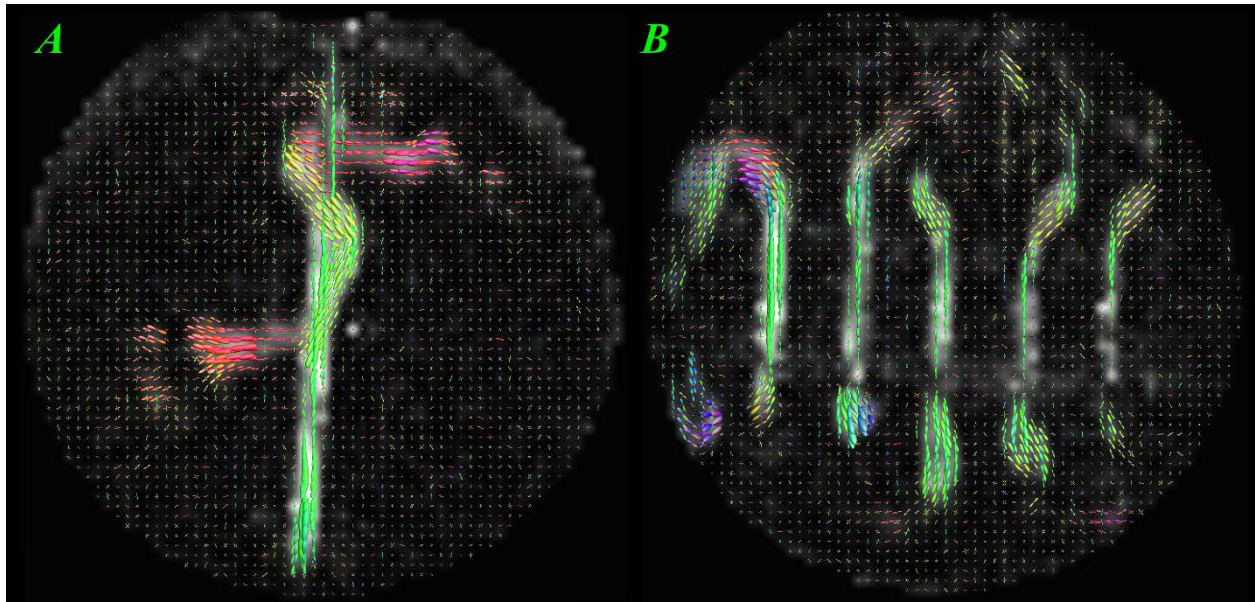
Figure 38. Horizontal slice of crossing pattern with fiber-ODF reconstructed using proposed reconstruction algorithm described in chapter two and three.

5.3.5   Fiber Tractography

The effects of the reconstruction algorithm are shown using fiber tracking. The choice of reconstruction method can affect peak estimation and hence the fiber tracking. Fiber tracking is performed after peak estimation from (fiber and diffusion) ODFs for each voxel. The multi-FACT algorithm (as described in [32]) is used to create fiber tracts. Fibers in crossing patterns are used to evaluate how the tracking algorithm performs. Fiber tracts in the packing density chambers are used to map the dAV metric for quantification (see Figure 39).

124
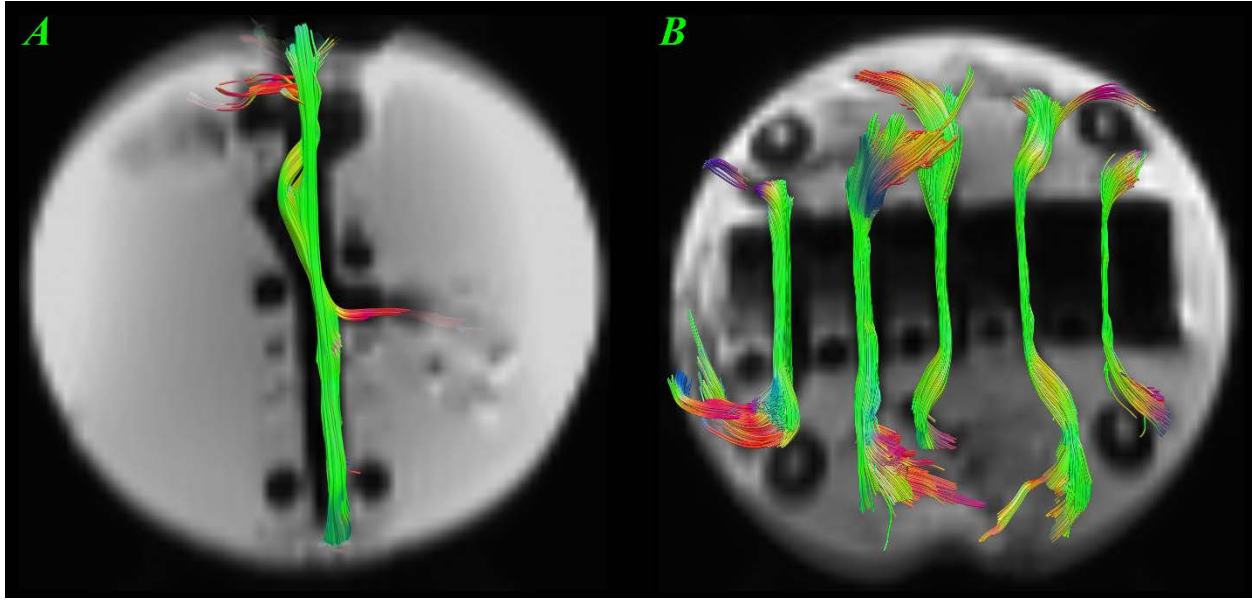
Figure 39. Fiber tracking is performed using principle diffusion directions calculated using the proposed reconstruction method.

5.3.6 Quantification of Taxonal Bundles

Two quantification methods are used to test hypothesis 3. The dAV and the NODDI models provide tract-based and voxel-based quantification of the underlying material.

5.3.6.1 dAV maps along fiber tracts

Isotropic and anisotropic water content is estimated using diffusion ODFs as described in Chapter 4. The isotropic part of the diffusion ODF was considered as free water content. Peaks of anisotropic ODFs were estimated and then used to perform fiber tracking in DSI Studio software [137]. A local seeding method is used to calculate fiber tracts in the five packing density chambers. The mean fiber is calculated for each chamber by selecting a fiber passing through the middle section of the bundle. Each fiber bundle was then sliced along the tangent of the mean fiber and the sum of the dAV values over the plane is calculated for each slice. The

summed dAV value is then plotted along the fiber bundle for all five tracts with varying number of taxons. Mean and standard deviation were also calculated for each bundle and plotted to correlate with the known fiber densities.

5.3.6.2 NODDI based voxel-wise quantification

The NODDI model [39] is used to model tissue micro-structure by modeling free, hindered, and restricted compartments. Unlike dAV, NODDI models isotropic water content separately. dAV uses the minimum of each ODF to estimate the isotropic value; this approach over estimates free water content in a voxel. There is no multiple fiber population support in the NODDI model yet, which makes NODDI under perform in detecting crossing patterns. NODDI models the MR signal in a voxel as a weighted linear sum of free, hindered, and restricted water diffusion.

$$\frac{\mathbf{S}(\vec{\mathbf{q}})}{\mathbf{S}(0)} = \mathbf{A}(\vec{\mathbf{q}}) = (1 - v_{iso})(v_{ic}\mathbf{A}_{ic} + (1 - v_{ic})\mathbf{A}_{ec}) + v_{iso}\mathbf{A}_{iso} \qquad (5.1)$$

where $\mathbf{A}_{ic}$ and v_{ic} are the normalized signal and volume fractions of the intra-cellular compartment, $\mathbf{A}_{ec}$ is the normalized signal of the extra-cellular compartment, and $\mathbf{A}_{iso}$ and v_{iso} are the normalized signal and volume fractions of the free water compartment. See [39] for details about the mathematical model used for $\mathbf{A}_{ic}$, $\mathbf{A}_{ec}$ and $\mathbf{A}_{iso}$. This model makes the ideal assumption that the radii of all taxons are zero. The analysis also fitted a diffusion model, which describes diffusion of water in an impermeable cylinder with a single non-zero radius for all taxons in a homogeneous medium [41, 42, 203, 204, 258, 259]. The radius of the taxons is estimated using this model and found to be 10.5 μm diameter with error of 0.5 μm.

5.4   RESULTS AND DISCUSSION

5.4.1   Anisotropic reconstruction of fibers

Diffusion tensor imaging shows high anisotropic water diffusion in voxels containing taxons. Fractional anisotropy and other related diffusion tensor-based metrics are calculated in five packing regions and one crossing region (see Table 4 and Figure 36) An average fractional anisotropy value of 0.75 is observed in voxels containing taxons, which is comparable to an FA value of (0.7) observed in the corpus callosum in the human brain [260].

Table 4. Mean values for Fractional Anisotropy (FA), Apparent Diffusion Coefficient (ADC), Mean Diffusivity (MD), Radial Diffusivity (RD) and Axial Diffusivity (AD) metrics across ROIs for the packing and crossing chambers.

DTI-based metric	20%	40%	60%	80%	100%	Crossing
FA	0.808	0.800	0.770	0.780	0.850	0.730
ADC x 10^{-3}	0.150	0.190	0.223	0.160	0.185	0.230
MD x 10^{-3}	0.150	0.190	0.223	0.160	0.185	0.230
RD x 10^{-3}	0.080	0.110	0.120	0.090	0.080	0.133
AD x 10^{-3}	0.330	0.411	0.470	0.344	0.460	0.500

5.4.2 Resolving fiber crossing

The principal diffusion direction derived from the first reconstruction method, DTI (described in section 5.3.4.1), is matched with the orientation of the taxonal bundle in voxels with single fiber populations. In voxels with fiber crossings, the DTI estimation of the principal diffusion direction is the average orientation of the underlying fiber population (see Figure 40).
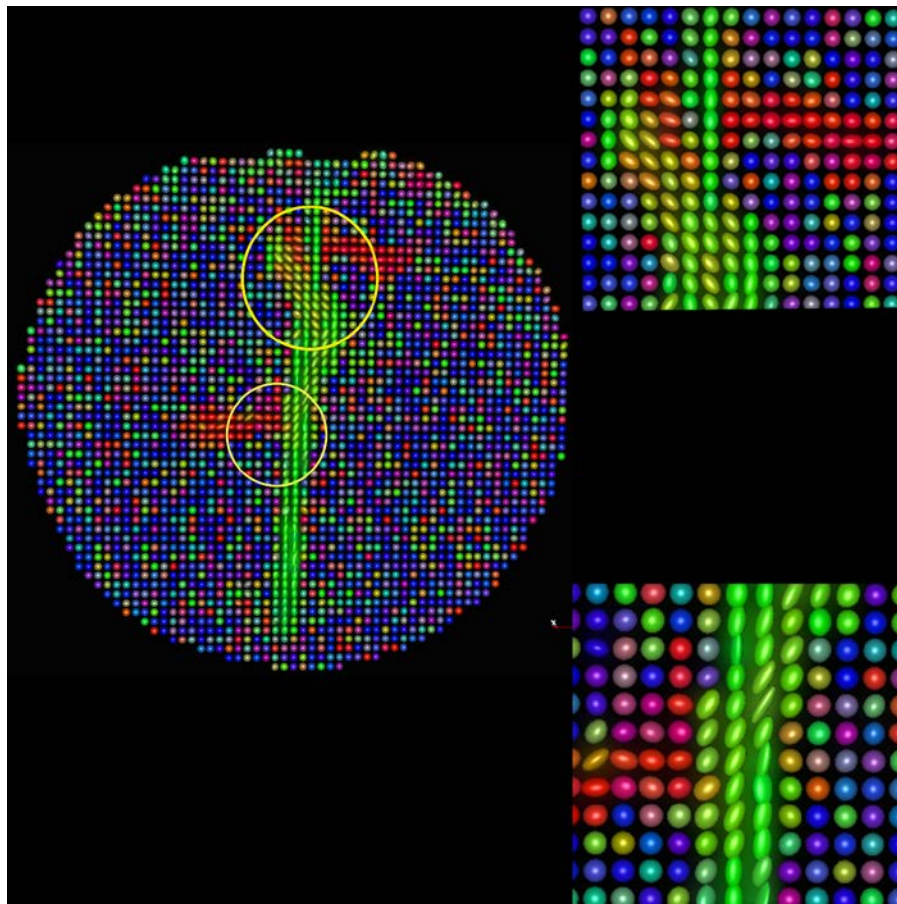
Figure 40. Diffusion Tensor estimated using reconstruction method described in chapter two. Upper right corner shows tensors in 90 degree and 45 degree crossing. Lower corner shows 30 degree crossing. Color in each voxel represents the orientation of the fiber (red color shows fiber oriented in left-right (x-axis) direction, green for anterior-posterior (y-axis) and blue for inferior-superior (z-axis). In case of isotropic diffusion i.e., non-determinant fiber orientation the voxel has a random color.

The second reconstruction method, Generalized Q-sampling Imaging (GQI), yields diffusion ODFs in crossing patterns that show that it can accurately resolve a 90° crossing angle in most of the voxels. Some voxels with 45° crossing angles can be accurately resolved but it fails to resolve any 30° crossings. GQI based diffusion ODFs have blurred peaks, which merge the two fiber populations as in DTI imaging, by smoothing the ridges of two peaks. The resulting peaks depend upon the volume fraction of the two-fiber population. More investigation is needed to verify these observations. dODFs are estimated on discrete spherical points, which adds a bias in estimation of the principal diffusion direction of the underlying fiber population (see Figure 41).
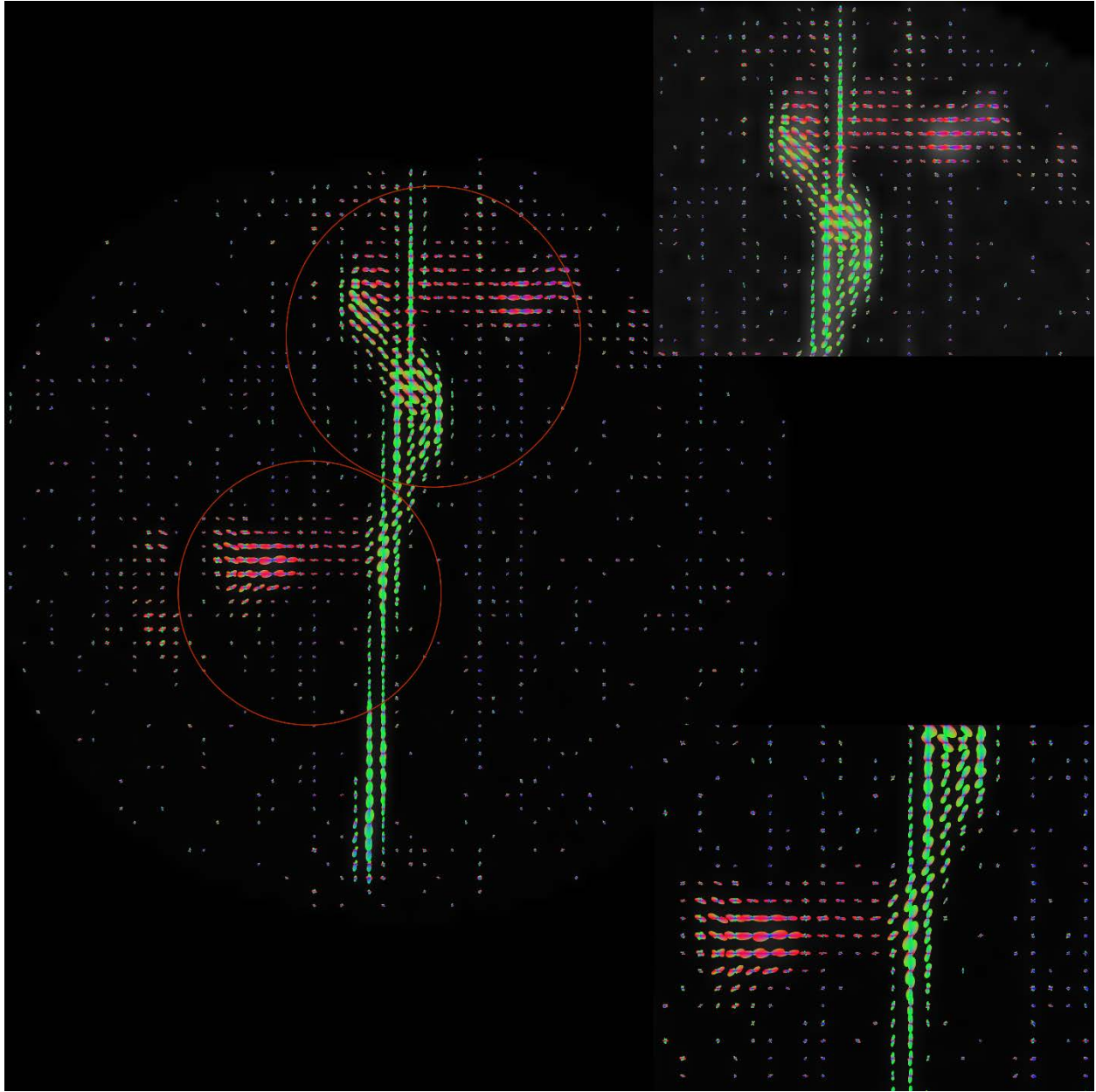
Figure 41. Diffusion ODF estimated using generalized q-sampling imaging. Upper right corner shows dODF in 90 degree and 45 degree crossing. Lower corner shows 30 degree crossing.

Fiber ODFs estimated from the proposed reconstruction algorithm shows that two peaks in $45°$ and $90°$ crossing patterns are aligned with the ground truth fiber population. fODFs in the $30°$ fiber crossing show only a single peak. It merges the peaks of two-fiber populations

crossing at a $30^{°}$ angle. Peaks of the fiber ODFs are sharper than diffusion-ODF based GQI methods as shown in Figure 37. Also, the peaks of fODFs are estimated in continuous space as compared to the dODF, which is defined on discrete points on a sphere. This suggests that spherical deconvolution may reduce bias in the estimation of peaks.
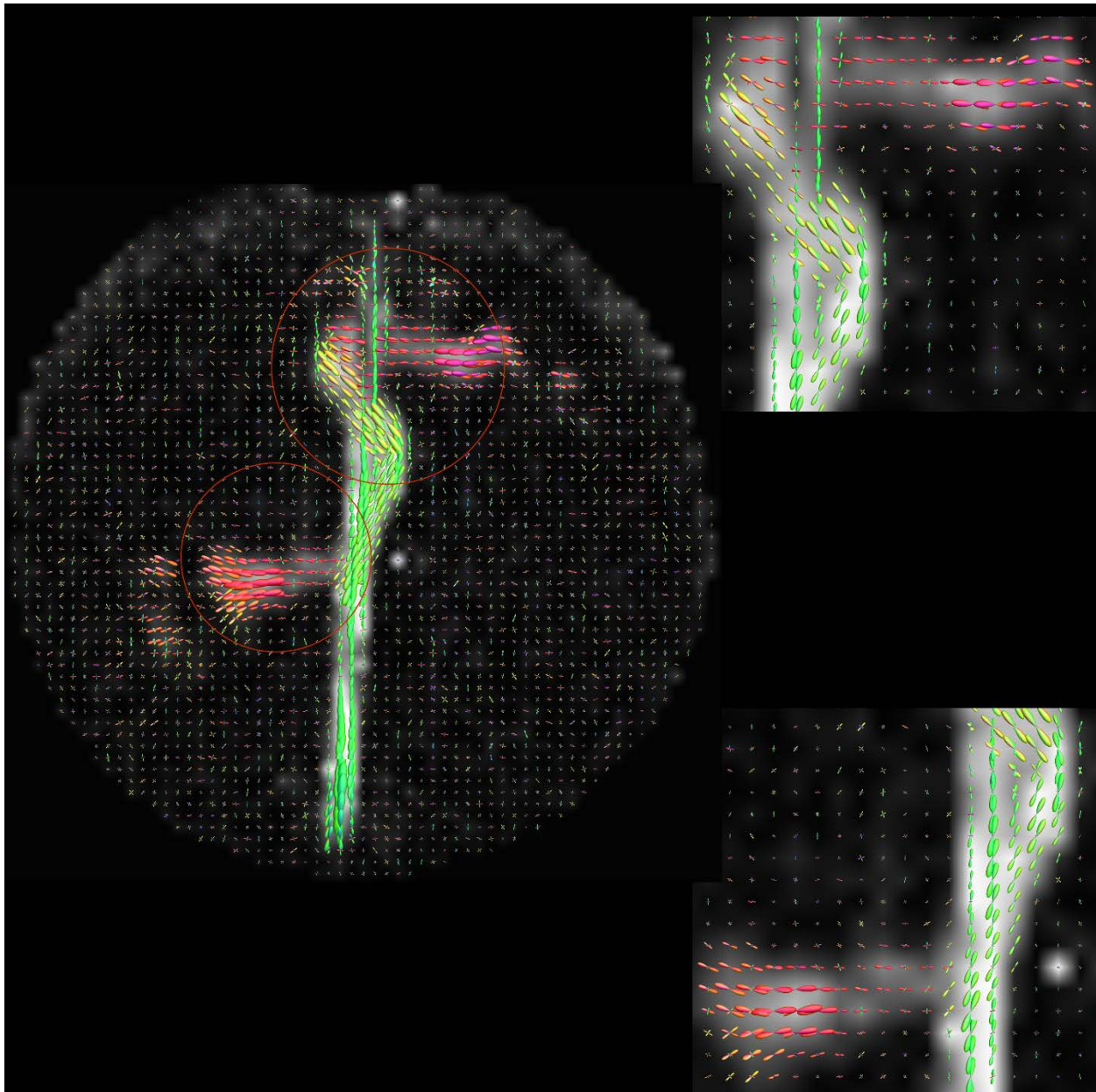
Figure 42. Fiber ODF estimated using proposed reconstruction method described in chapter three. Upper right corner shows fODF in $90^{°}$ and $45^{°}$ crossing. Lower corner shows $30^{°}$ crossing.

131

Table 5. The number of voxels with crossing resolved by three reconstruction algorithms: Diffusion Tensor Imaging (DTI), Generalized Q-sampling Imaging (GQI) and Proposed Reconstruction Algorithm described in chapter two. Regions of Interest are manually drawn at each crossing. A bigger ROI is drawn to make sure that all voxels with a crossing are selected. All methods failed to resolve the 30 degree crossing in any voxel. DTI failed to resolve any crossings for all voxels. GQI resolved less crossings when compared with the proposed reconstruction algorithm described in chapter two. The effect is due to the fact that GQI estimates diffusion ODFs as opposed to fiber ODFs.

Number Of Voxels	30°	45°	90°
Diffusion Tensor Imaging	0	0	0
Generalized Q-sampling Imaging	0	3	13
Proposed Reconstruction Algorithm	0	8	19

5.4.3 Quantifying number of taxons of fiber tracts

Fractional anisotropy is estimated for each taxon packing density chambers. FA is then plotted against the know number of taxons for each chambers. FA curve is expected non-monotonic. A correlation coefficient of $r = 0.33$ is estimated between FA and number of taxons (see Figure 43). This shows that FA is poor predictor of underlying taxonal volume but it is sensitive to the voxels with anisotropic water content.
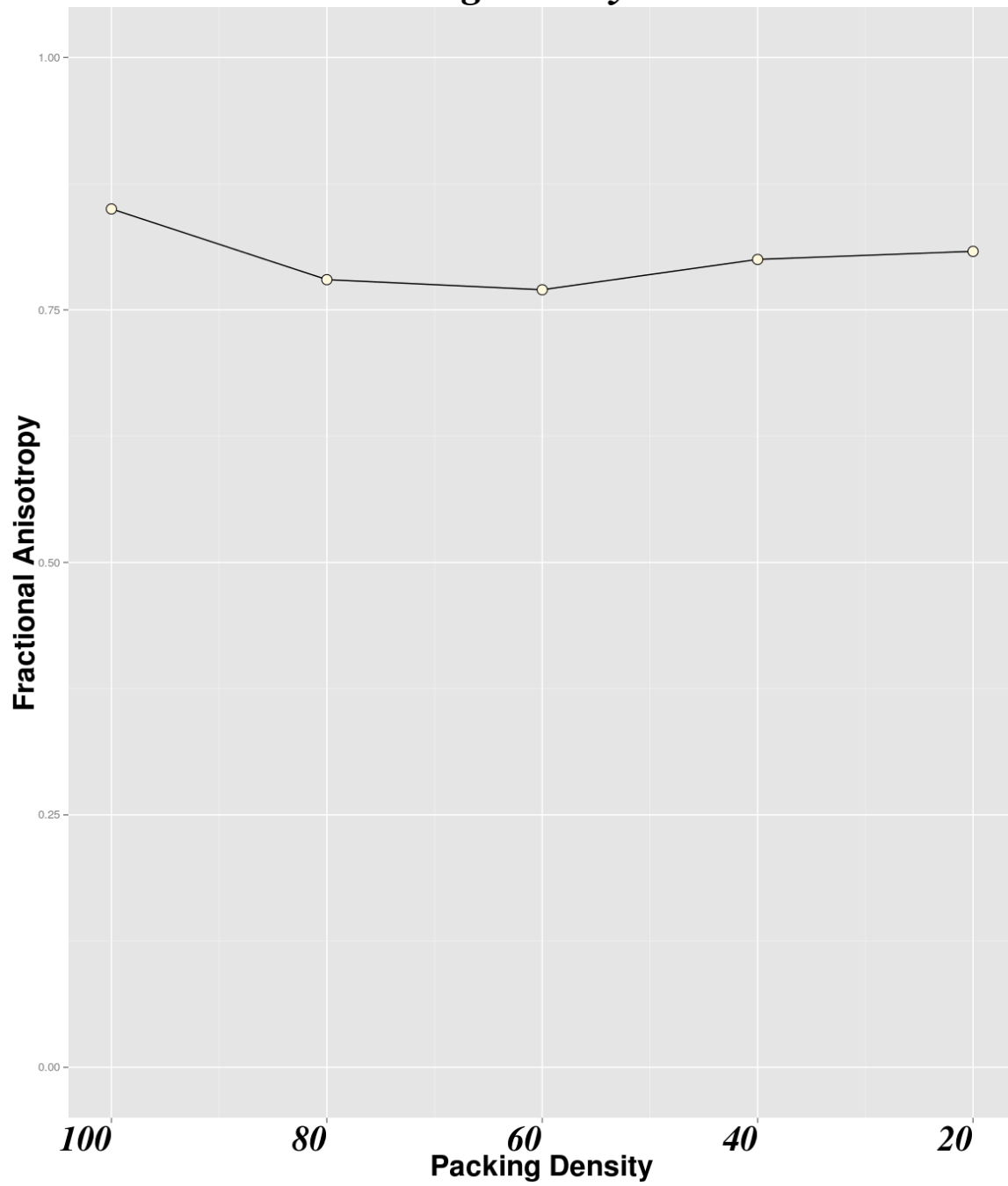
Figure 43. Mean FA values is estimated for each taxonal bundle. FA show a 0.33 correlation with the actual number of fibers.

DAV is estimated for the taxon packing density chambers using the framework described in chapter four. Estimated dAV values for each fiber bundle are then plotted against the known numbers of taxons for each chamber (see Figure 43 and 44). A correlation coefficient of 0.85 is computed between the known number of taxons and the dAV values. For the taxon fiber bundles with 60%, 80%, and 100% density patterns, a linear pattern is observed in the dAV metric. For the 20% and 40% density patterns, the dAV value dropped to 5% (see Figure 45). One of the reasons for this might be the simplified model of isotropic water content. dAV uses a very crude model for estimating the isotropic part, the minimum of the diffusion ODF, which is an overestimation of free water content. Separate modeling of isotropic water can provide a robust estimate for free and restricted water content in a voxel.
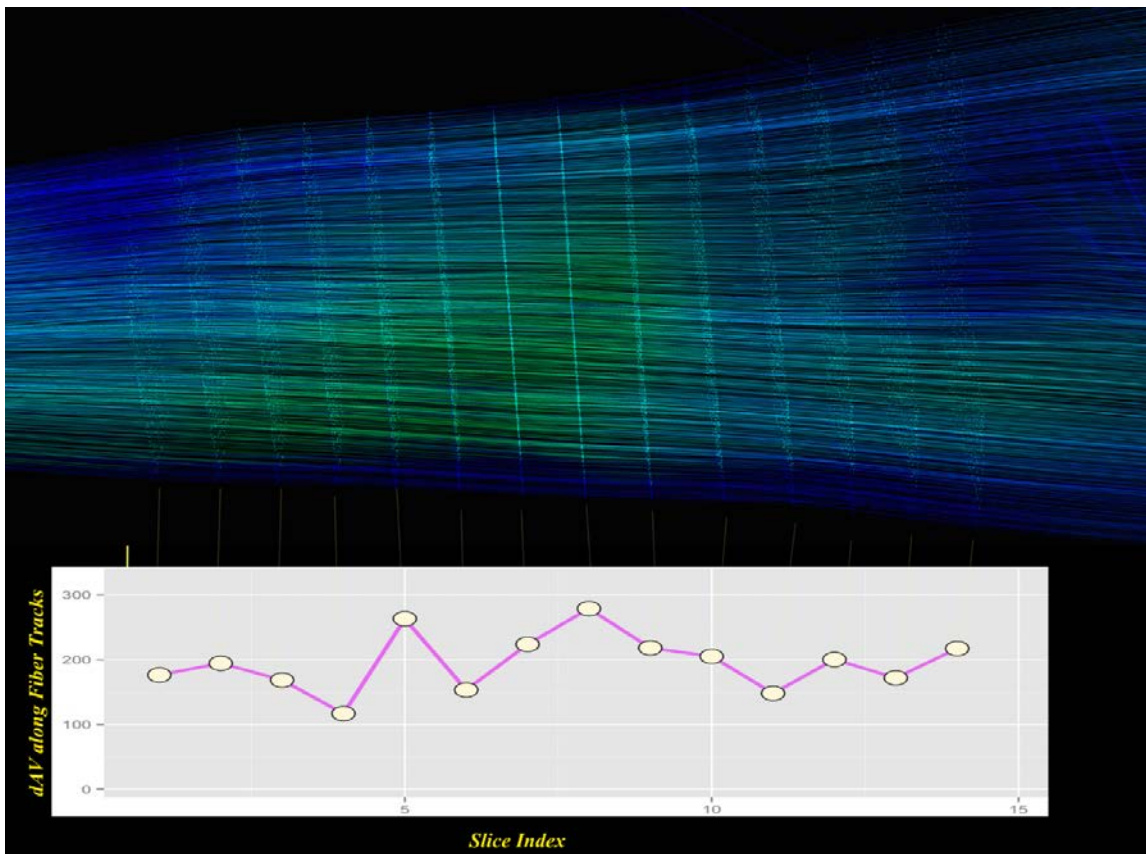
Figure 44. dAV is estimated for each fiber cut based on mean fiber. dAV Mapping and quantification framework is described in chapter four.
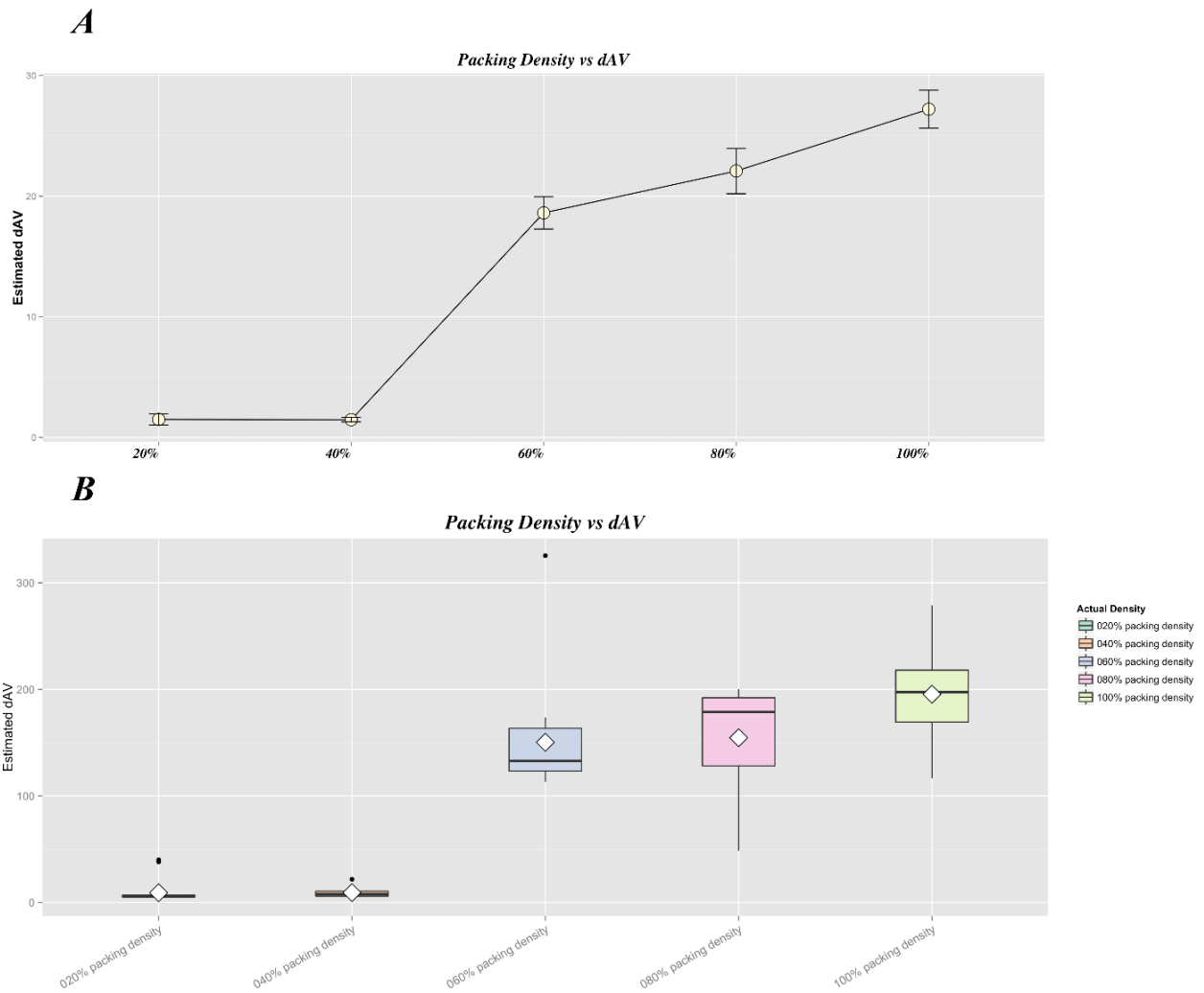
Figure 45. (A) Mean dAV value is estimated for each fiber bundle $(20\%,40\%,60\%,80\%,100\%)$. Mean dAV maps show a 0.85 correlation with the actual number of fibers. Fiber bundles with $(60\%,80\%,100\%)$ the number of fibers show a good agreements with the known number of fibers. (B) Boxplot of the dAV values for each fiber bundle.
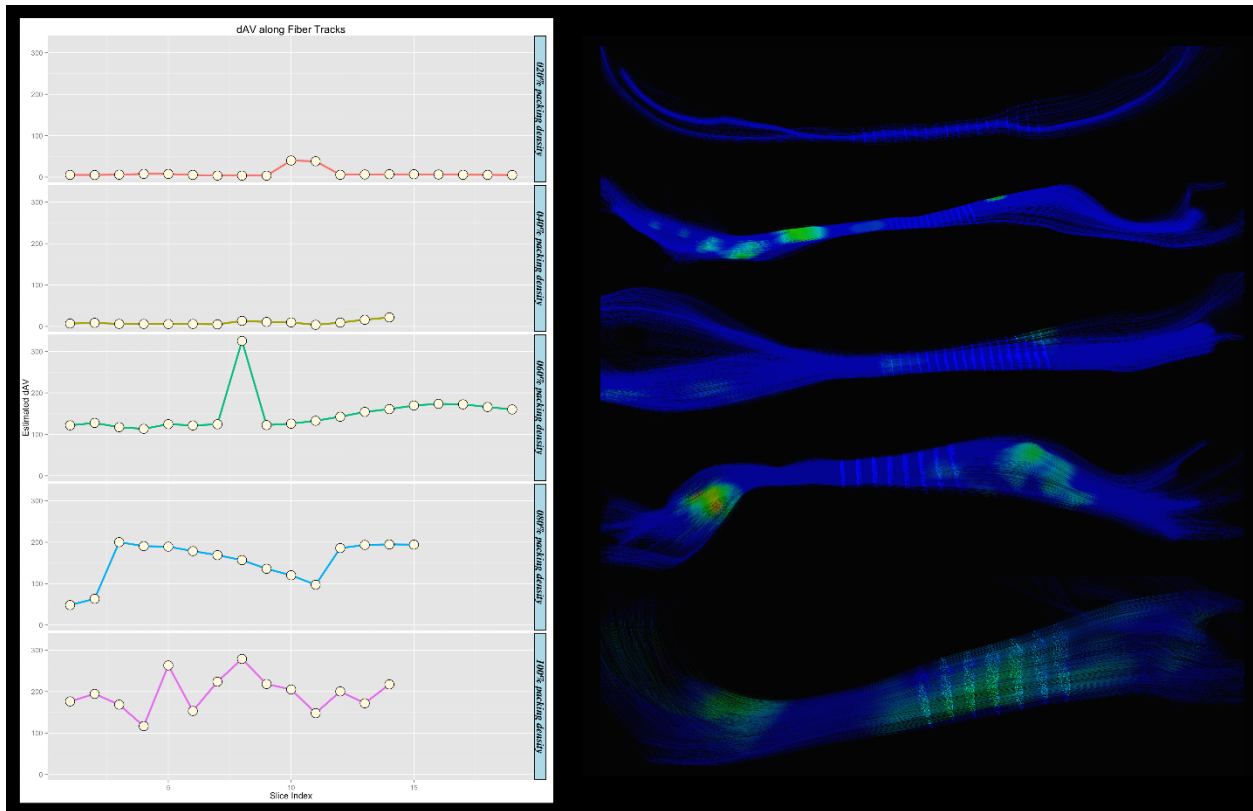
Figure 46. dAV along each fiber bundle is estimated for the packing density pattern. Fibers are sliced based on the mean fiber from each bundle. The graph shows the profile of dAV along the fiber bundles.

NODDI addresses this issue by modeling the isotropic part separately. NODDI estimates a volume fraction of isotropic, hindered, and restricted compartments in a voxel. The NODDI model (and CHAMRED model) can be used with different combinations of hindered and restricted compartments. A typical model includes fibers with zero radius. In this study, two versions of the NODDI model were used: one with zero diameter fibers and another one with unknown non-zero diameter fibers (see Figure 47).
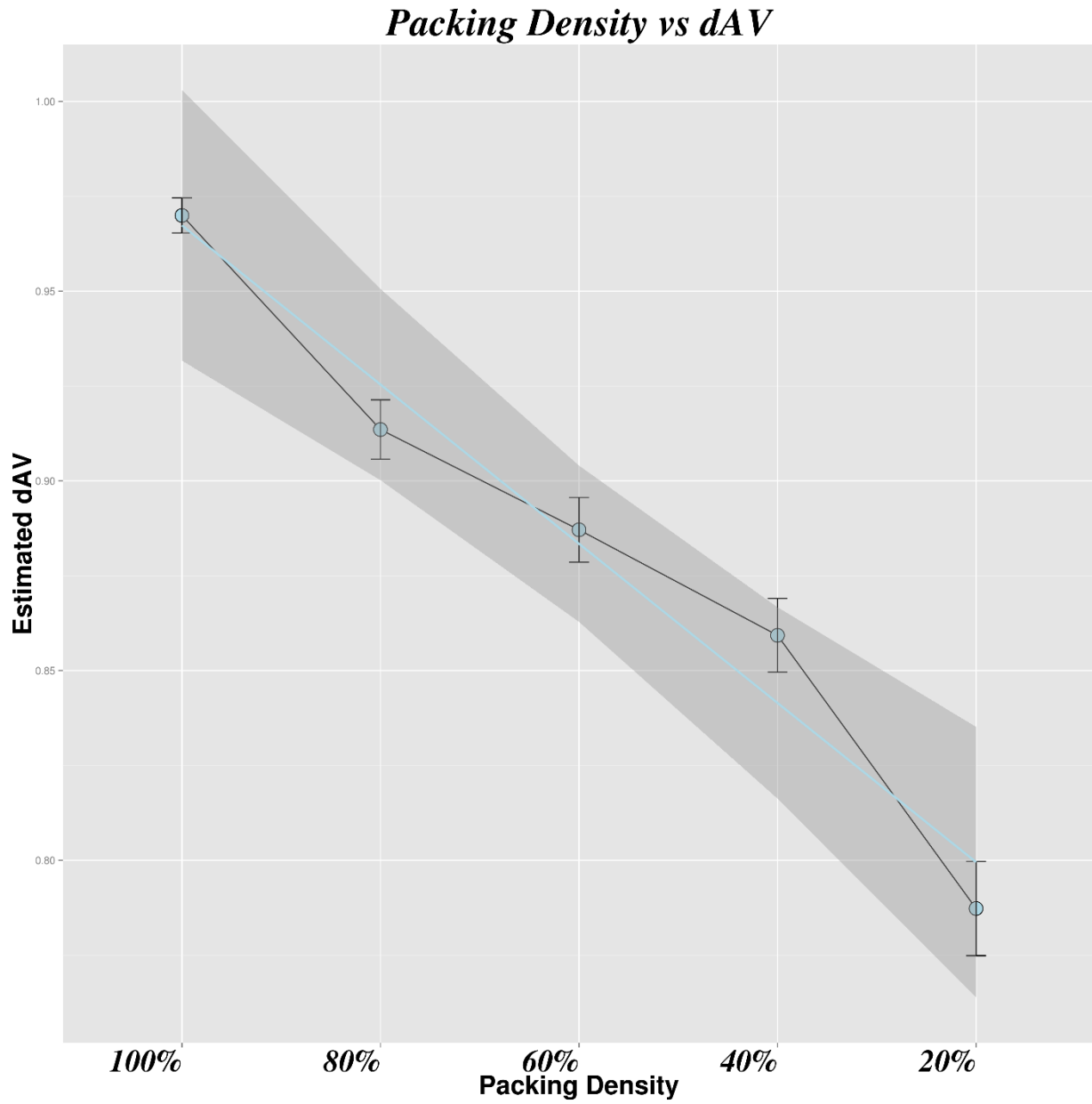
Figure 47. NODDI based intra-cellular volume fraction v_{ic} is estimated for each voxel for each fiber bundle. Mean v_{ic} is estimated for each fiber bundle. A correlation of 0.95 is estimated between mean (v_{ic}) and the known number of fibers in each bundle

The model with the zero radius is used to estimate the volume fraction of isotropic and restricted water content. For each fiber bundle, the volume fraction of intra-cellular water content

is plotted against a known number of taxon fiber bundles. A correlation coefficient of 0.95 is obtained by correlating the mean of the volume fraction of intra-cellular water content of each voxel corresponding to each chamber with a known number of taxon fiber bundles.

We need to be careful about the limitation of NODDI to just fit single fiber populations, which makes it difficult to apply this method in the whole human brain. Also this is a voxel based method, in order to calculate structural connectivity between cortical regions we need a tract based metric.

The model with the non-zero diameter of cylinder (taxons) is used estimate the diameter of the taxons in each voxel. A mean value of $10.2 \, \mu m$ is estimated for each chamber, irrespective of the number of taxons. The known diameter of taxons used in this study is $12 \, \mu m$.

In previous studies, phantoms with solid fibers were used to test the geometrical properties of fiber bundles (crossing pattern) and their effect on the fiber tracking. On the other hand, glass capillaries based phantoms are used to test the size of compartments (and underlying geometry) on NMR machines with advanced pulse sequences (single and double PGSE) [194, 208, 209]. In this study, textile based phantoms are used to test both the geometrical information and the compartment size on a clinical scanner. Therefore, the results of this study show a good agreement between the manufactured dimensions and the estimated configuration of fiber bundles.

5.5   LIMITATIONS AND EXTENSIONS

The TABIP is the very first version of a hollow fiber fabric phantom, which can be configured to different numbers of taxons and crossing patterns. Manufacturing tests are needed to further

validate this phantom. In this study, the TABIP is considered as a ground truth for diffusion model testing. More investigation is needed to establish further agreement between manufactured information and diffusion model information.

The analysis of crossing taxonal bundles is limited due to the coarse level of inter-digitation (2 and $5\,mm$), which is comparable to MR voxel size. High-resolution scans of the phantom are not able to capture multiple fiber populations in a voxel. Future experiments should design layers of taxonal bundles such that MR imaging with inter-digitation of the tracts at the $0.5\,mm$ scale.

The TABIP controls hindered water (water between taxons) by controlling the number of taxons and their packing density. A true test to extract the contribution of the MR diffusion signal from hindered compartments is to mask the restricted compartment completely. This can be achieved by filling taxons with D_2O which is insensitive to H_2O based imaging. In future experiments taxons filled with D_2O will be utilized to test the effect of hindered and restricted compartments on the diffusion MR signal.

The Directional Axonal Volume along the fiber tracts shows small variation which suggest that the amount of water content (dAV) is preserved. We have observed more dAV variation for chambers with a greater number of fibers. Future experiments will explore conservation of dAV along tracts.

Effect of susceptibility artifacts due to 80% fill rate on crossing and quantification measurement is not addressed in this thesis. In future experiments a detailed MR experiment can be designed to further explore the susceptibility artifacts.

The fiber tracking experiment in this study tested on three basic crossing patterns. A more sophisticated design is needed to test fiber-tracking algorithms. In future experiments,

complex routing phantoms can be used to test known start and end points with crossing, kissing, and merging patterns of taxonal bundles.

The TABIP is designed to simulate three compartments: free, hindered and restricted with taxons of same diameter. In future experiments, taxons with multiple diameters and known volume fractions can be used to simulate multiple restricted compartments. AxCaliber [41, 42], restricted spectrum imaging [125] etc. can be used to validate such configurations.

5.6   CONCLUSION

In this chapter, three hypotheses are tested and confirmed on TABIP. First hypothesis states that diffusion MRI can image anisotropy in taxonal bundle. Results show diffusion tensor imaging can successfully image the location of the taxonal bundles. Both crossing and packing density pattern is seen in fractional anisotropy volume (FA greater than 0.7). Orientation of the taxonal bundle is also accurately mapped in the regions with single fiber populations using DTI (see Figure 36).

Second hypothesis, which relates to resolving of fiber crossing, is tested using three reconstruction method, DTI, GQI and proposed reconstruction method described in chapter three. DTI fails to resolve crossings in all three test regions ($30^{\circ}, 45^{\circ}, 90^{\circ}$) as shown in Figure 37. GQI and the proposed reconstruction method are able to resolve crossings at 45° and 90°. Both methods resolve more voxels at 90° than 45° crossings. The proposed reconstruction method can resolve more voxels with crossings. Spherical deconvolution used in the proposed reconstruction method creates sharper ODFs than GQI. Both methods failed to resolve crossings

at 30°. More investigation is needed to determine whether this is a limitation caused by the model or a limitation of the current diffusion imaging acquisition technology.

Third hypothesis is that diffusion MRI based anisotropic metric can be sensitive to amount of fibers. FA, dAV and NODDI model is tested if they are sensitive to amount of underlying fibers. dAV values vary with the number of taxons accurately with correlation coefficient of ($r = 0.85$) whereas the most commonly utilized metric, FA, correlated only at $r = 0.33$ and was not monotonically related to the ground truth number of taxons (see Figure 43). dAV values along the fiber bundles in a number of taxon regions show little variation along the fiber bundle. This suggests that fiber-based dAV quantification is robust. There are some slices that show large variations due to partial volume effects. Further analysis is required to estimate the error in dAV maps and different voxel resolution scans can provide insight into the partial volume effect.

The NODDI model can predict the number of taxons with a correlation coefficient of 0.98. Such a high correlation coefficient suggests that estimation of free water content plays important role in quantifying connectivity. Combining the NODDI method with a dAV-based framework can provide a robust quantification of isotropic water content and mapping of anisotropic metrics on fiber tracts. Fiber based metrics like dAV combined with NODDI (or CHARMED model combined with free water) can provide an accurate structural connectivity metric between cortical regions.

Novel textile phantom used in this chapter is key to evaluate reconstruction methods and related anisotropic metrics. It provides ground truth, which is missing in diffusion MRI field. It can also be used in further testing of reliability of these metrics.

6.0   CONCLUSION

This thesis work presents contributions in three major areas of diffusion imaging: reconstruction, quantification and validation. Chapters two and three present a novel reconstruction method by combining generalized q-sampling imaging, spherical harmonic basis functions and constrained spherical deconvolution methods to estimate the fiber oriented distribution function. Chapter four presents a novel metric, directional Axonal Volume, to estimate directional anisotropy using the oriented distribution function (ODF) and proton density map. It also describes a tract based mapping algorithm to map the directional Axonal Volume metric onto the fiber tracts. Chapter five presents the validation of reconstruction and quantification methods using a textile based anisotropic phantom. The reconstruction and quantification algorithms presented in the previous chapters are tested on known fiber crossing and density patterns.

Reconstruction of diffusion in a voxel is the first step in the analysis of diffusion weighted imaging. Accuracy of the reconstruction method can affect subsequent processing such as fiber tracking. There are two popular non-parametric methods, q-ball imaging [1]) and generalized q-sampling imaging [2], used to reconstruct the diffusion ODF. Q-ball imaging is used for a single shell (constant b-value) image acquisition. Spherical harmonic coefficients estimated from q-ball imaging can further be used to create the fiber ODF using the constrained spherical deconvolution method [3]. CSD is becoming a more popular diffusion reconstruction method in both the clinical and neuroscience research fields. Generalized q-sampling imaging on

the other hand utilizes a better q-space sampling, such as diffusion spectrum imaging, for reconstruction of the diffusion ODF. In chapter two, I have combined both methods to derive an analytic closed form solution for spherical harmonic coefficients of the diffusion ODF (see equation 2.49 in chapter two). This method enables us to apply constrained spherical deconvolution techniques for estimation of spherical harmonic coefficient of the fiber ODF.

In chapter three, I have derived a novel mathematical formation to estimate spherical harmonic coefficients of the fiber ODF using the constrained spherical deconvolution (CSD) method on a diffusion spectrum imaging dataset. CSD was originally used on a single shell diffusion acquisition sampling. This novel formulation of combining CSD and GQI allows one to use advantages of CSD and GQI techniques on multiple b-value sampling. I have demonstrated the CSD technique on a simulated data set. The CSD technique reconstructs shaper peaks (see Figure 17 in chapter three) than the diffusion ODF. Another key advantage of the spherical harmonic method is that one can resample the fODF to a high spatial resolution space. I have demonstrated, qualitatively, the effect of peak sharpness and resampling on a diffusion spectrum scan of a healthy human subject. A directionally encoded color map of the fiber peaks estimated using high resolution fODFs shows the anatomical location of thalamic nuclei (VL and VP) and cerebellar nuclei that are missing in low resolution diffusion ODF maps (see Figure 19 and 20 in chapter three). In the area of the brain stem, boundaries of the white matter structures are clearly identified in the high resolution fiber ODF map (see Figure 21 in chapter three). Sharper fiber peaks in fiber tractography were demonstrated on the fornix tract, arcuate and superior cerebral peduncle in both high resolution fiber ODF and low resolution diffusion ODF. Qualitative comparison of the fiber tracts shows a clear advantage of the proposed CSD method and resampling of the fiber ODFs in finding interhemispheric space, fiber termination at the grey-

white matter boundary, and less noise in the fiber crossing region (see Figure 22, 23 and 24 in chapter three).

Quantification of the underlying white matter structure using diffusion MRI based metrics is an active research area. Clinicians and researcher are looking for a robust diffusion MRI based metric that can relate to axonal volume and is sensitive to white matter changes in pathological brains. Previously, scalar metrics such as fractional anisotropy have been used to indicate white matter changes. Scalar metrics provide summary statistics of anisotropy from each fiber population present in a voxel. In chapter four I derived a mathematical formulation of a novel metric, directional axonal volume dAV, to quantify anisotropy in each direction (see section 4.3 in chapter four). It uses the full oriented distribution function in a voxel weighted by a proton density map to estimate anisotropy of diffusion in each direction. The key feature that differentiates directional axonal volume from scalar metrics is that it is direction sensitive and thus does not mix the anisotropies of multiple fiber populations. An algorithmic framework that maps voxel-wise dAV to tracts and profiles the fiber tracts (see section 4.4 in chapter four) is also presented. This method permits voxel-based dAV to become a tract-based metric. The novel contribution of tract-based dAV is that it maps only anisotropic values that are aligned with the fiber tract, unlike Yeatman et al [4] who map FA onto the fiber tract by interpolating the FA volume for each fiber point. Typically, canonical planes that are parallel to the scan axis are used for profiling. I have also presented an informative way to profile of the dAV metric along a mean fiber. Profiling in this way will potentially be used to identify white matter damage along a fiber tract. Profiling of the arcuate and cingulum in a healthy subject shows small variation of dAV along tracts (see Figure 29 and 30 in chapter four). This suggests that dAV is conserved along the tract (with coefficient of variation of 16%). In contrast, techniques such as Yeatman el al [4],

show a bell curve along the tract. In chapter five, I used an anisotropic textile based phantom to test if dAV relates to the number of taxons present. A correlation coefficient of 0.85 is estimated between number of taxons and total dAV (see Figure 44 in chapter five), which suggest that dAV is potentially related to the intra-cellular water content and thus eventually related to underlying axonal volume.

Validation of the diffusion reconstruction methods, the fiber orientations estimated from the reconstruction methods, the derived anisotropic metrics is essential for robustness of the analyses and in particular longitudinal and multi-site analyses. Validation of the anisotropic metric is key in order to use it as a biomarker in neurological studies. For example, a validated diffusion metric can provide regions of white matter changes affected in neurodegenerative diseases like Huntington's disease and Parkinson's disease.

In chapter five I used a novel textile based anisotropic phantom (TABIP) to validate three diffusion reconstruction methods: diffusion tensor imaging, generalized q-sampling imaging and proposed reconstruction method described in chapter two, and three anisotropic metrics: fractional anisotropy, directional axonal volume and the NODDI model. It is the first textile hollow tube phantom that can simulate the complex geometry of curves, crossing, shape deformation, and compression that are representative of human tract anatomy. It provides ground truth testing of key variables in MRI such as crossing patterns and intra Taxon water content (see Figure 47 in chapter five). I have tested three hypotheses using TABIP, 1) taxons can be imaged using diffusion MRI and recorded metrics such as FA can be in the range of human tissue, 2) the diffusion MRI based reconstruction method can resolve known crossings, and 3) the diffusion MRI based anisotropic metric is sensitive to the number of taxons in a

volume and there is reasonable agreement between the electron microscope measurement of the diameter and the MRI measurement.

All reconstruction methods tested can localize anisotropic regions of taxons. I used the diffusion tensor imaging method to estimate FA in all regions with taxons. Regions with taxons have FA values (max FA = 0.7) that are similar to previously reported FA values in white matter areas (in corpus callosm FA = 0.8) in the human brain (see Figure 36 in chapter five). White matter tissue in the human brain is very complex due to the combination of various tissues (glial cells, CSF, axons with different diameters). In comparison, TABIP used in this study has a perfect tube that can be used as a known calibration reference. We were able to do ground truth tests such as accuracy of the taxon diameter measurements using NODDI model. Electron microscope based measurements estimate 12-13 diameter of taxons and the NODDI based metric estimates 10.5 with standard deviation 0.5.

The second hypothesis, resolving crossing fibers, was tested using a manufactured crossing pattern with 90, 45, and 30 degree crossing angles. Three reconstruction methods: diffusion tensor imaging, generalized q-sampling and the proposed reconstruction method described in chapter two and three were tested. GQI and the proposed method can successfully identify 90 and 45 degree but fails to resolve 30 degree crossings. DTI fails to identify all crossing fiber populations (see Figure 40). The new reconstruction method produces sharpened peaks of the fiber orientation than the GQI techniques (see Figure 41 in chapter five).

All three reconstruction methods, diffusion tensor imaging, generalized q-sampling and the proposed reconstruction method described in chapter two and three fail to resolve the 30 degree crossing. Further investigation is needed to test whether this limitation of resolving the 30

degree crossing is due to diffusion image acquisition or diffusion modeling techniques. This limitation also affects further processing such as fiber tracking.

The third hypothesis, accuracy of fiber count estimation, is tested on a manufactured fiber density pattern with varying number of taxons (100%, 80%, 60%, 40% and 20%). Three anisotropic metrics, fractional anisotropy, directional axonal volume and NODDI are tested and correlated with the number of taxons in density pattern.

FA shows a correlation coefficient value of $r = 0.33$ with the number of taxons used in the density pattern (see Figure 43 in chapter five). As implicitly used by some investigators, FA would be expected to vary linearly with the underlying amount of taxons. The poor correlation and the non-monotonic relationship of FA to taxon counts suggest that FA is sensitive to identifying anisotropic areas in a diffusion scan but it is a poor predictor of number of fibers.

dAV on the other hand, shows a correlation value of $r = 0.85$ with the number of fibers used in the density pattern. However, estimated dAV values drop to a small value after a reduction of 40% or less of fibers in the density pattern (see Figure 45 in chapter five). This effect might be due to a very simplistic isotropic modeling. To address this issue I chose the NODDI model for estimation of isotropic and anisotropic volume fractions in each voxel from the density pattern. Better isotropic modeling in the NODDI technique improves the correlation between the number of taxons and the intra-cellular volume fraction to $r = 0.95$. This result suggests that NODDI and dAV are sensitive to the underlying amount of taxons. With advanced isotropic modeling for free water contents the sensitivity to the number of taxons can be increased. This hypothesis provides insight into anatomically relevant metrics and their potential usefulness in neuro-scientific studies.

I have successfully tested that diffusion MRI is sensitive to regions with fibers. Advanced diffusion imaging techniques can be used to resolve crossing fiber bundles. I also found that less than a 45 degree crossing cannot be resolved using diffusion MRI for the methods tested. Advanced biophysical model such as NODDI can be used to probe micro-structure information such as amount of fibers and diameter of fiber.

In future, I will improve constrained spherical deconvolution to include multiple response functions from different tissue types. This type of multi-tissue diffusion modeling can not only provide fiber orientation but can also estimates the volume fraction of tissue types in a voxel. Further, I will use the volume fraction of cerebro-spinal fluid (isotropic) estimated using the multi-tissue model in the directional axonal volume metric.

This work represents a new accurate quantification of axonal water through diffusion imaging. dAV show promise as a new anatomically interpretable metric of axonal connectivity that is not confounded by factors such as axon dispersion, crossing and local isotropic water content. I believe this will be helpful in better anatomical mapping of white matter and the detection of axonal tract pathology.

BIBLIOGRAPHY

1.   Farid, N., et al., Restriction-Spectrum Imaging of Bevacizumab-Related Necrosis in a Patient with GBM. Frontiers in oncology, 2013. **3**: p. 258.

2.   Fernandez-Miranda, J.C., et al., High-definition fiber tractography of the human brain: neuroanatomical validation and neurosurgical applications. Neurosurgery, 2012. **71**(2): p. 430-453.

3.   Hagmann, P., et al., White matter maturation reshapes structural connectivity in the late developing human brain. Proc Natl Acad Sci U S A, 2010. **107**(44): p. 19067-72.

4.   Horsfield, M. and D. Jones, Applications of diffusion-weighted and diffusion tensor MRI to white matter diseases - a review. NMR in biomedicine, 2002. **15**(7-8): p. 570-577.

5.   Klingberg, T., et al., Myelination and organization of the frontal white matter in children: a diffusion tensor MRI study. Neuroreport, 1999. **10**(13): p. 2817-21.

6.   Lochner, C., et al., Evidence for fractional anisotropy and mean diffusivity white matter abnormalities in the internal capsule and cingulum in patients with obsessive-compulsive disorder. Journal of psychiatry & neuroscience : JPN, 2012. **37**: p. 193-9.

7.   Mädler, B., et al., Is diffusion anisotropy an accurate monitor of myelination?. Correlation of multicomponent T2 relaxation and diffusion tensor anisotropy in human brain. Magnetic Resonance Imaging, 2008. **26**: p. 874-888.

8.   Metwalli, N.S., et al., Utility of axial and radial diffusivity from diffusion tensor MRI as markers of neurodegeneration in amyotrophic lateral sclerosis. Brain Research, 2010. **1348**: p. 156-164.

9.   Oishi, K., et al., The fornix sign: a potential sign for Alzheimer's disease based on diffusion tensor imaging. Journal of neuroimaging : official journal of the American Society of Neuroimaging, 2012. **22**: p. 365-74.

10.   Pasternak, O., et al., Excessive extracellular volume reveals a neurodegenerative pattern in schizophrenia onset. J Neurosci, 2012. **32**(48): p. 17365-72.

11.   Pierpaoli, C., et al., Water diffusion changes in Wallerian degeneration and their dependence on white matter architecture. Neuroimage, 2001. **13**(6 Pt 1): p. 1174-85.

12.   Puig, J., et al., Decreased corticospinal tract fractional anisotropy predicts long-term motor outcome after stroke. Stroke, 2013. **44**: p. 2016-2018.

13.   Rae, C.L., et al., White matter pathology in Parkinson's disease: The effect of imaging protocol differences and relevance to executive function. NeuroImage, 2012. **62**: p. 1675-1684.

14.   Rosas, H., et al., Diffusion tensor imaging in presymptomatic and early Huntington's disease: Selective white matter pathology and its relationship to clinical measures. Movement disorders : official journal of the Movement Disorder Society, 2006. **21**(9): p. 1317-1325.

15.   CDC. Center for disease control. Available from: http://www.cdc.gov/.

16.   Ciccarelli, O., et al., Diffusion-based tractography in neurological disorders: concepts, applications, and future developments. Lancet neurology, 2008. **7**(8): p. 715-727.

17.   Ellis, C., et al., Diffusion tensor MRI assesses corticospinal tract damage in ALS. Neurology, 1999. **53**(5): p. 1051-1058.

18.   Fernandez-Miranda, J.C., et al., High-definition fiber tracking guidance for intraparenchymal endoscopic port surgery: Technical note. Journal of neurosurgery, 2010. **113**(5): p. 990-999.

19.   Shin, S.S., et al., High-definition fiber tracking for assessment of neurological deficit in a case of traumatic brain injury: finding, visualizing, and interpreting small sites of damage: Case report. Journal of neurosurgery, 2012. **116**(5): p. 1062-1069.

20.   Finch, D.M., E.L. Derian, and T.L. Babb, Afferent fibers to rat cingulate cortex. Exp Neurol, 1984. **83**: p. 468-485.

21.   Schmahmann, J.D. and D. Pandya, Fiber Pathways of the Brain. 2009: p. 654.

22.   Rinaman, L. and G. Schwartz, Anterograde transneuronal viral tracing of central viscerosensory pathways in rats. The Journal of neuroscience : the official journal of the Society for Neuroscience, 2004. **24**: p. 2782-2786.

23.   Oh, S.W., et al., A mesoscale connectome of the mouse brain. Nature, 2014. **508**: p. 207-14.

24.   Obuchowski, N.a., et al., Quantitative imaging biomarkers: A review of statistical methods for computer algorithm comparisons. Statistical methods in medical research, 2014.

25.   Lauterbur, P.C., Image Formation by Induced Local Interactions: Examples Employing Nuclear Magnetic Resonance. Nature, 1973. **242**: p. 190-191.

26.   Lauterbur, P.G. and C.-M. Lai. Zeugmatography by Reconstruction from Projections. IEEE Transactions on Nuclear Science 1980 [cited 27; 1227-1231]. Available from: 10.1109/TNS.1980.4330995.

27.   Mansfield, P., A.A. Maudsley, and T. Bains, Fast scan proton density imaging by NMR. Journal of Physics E: Scientific Instruments, 1976. **9**.

28.   Frey, S., et al., Dissociating the human language pathways with high angular resolution diffusion fiber tractography. The Journal of neuroscience : the official journal of the Society for Neuroscience, 2008. **28**: p. 11435-11444.

29.   Jones, D.K., Studying connections in the living human brain with diffusion MRI. Cortex, 2008. **44**: p. 936-952.

30.   Toosy, A.T., et al., Characterizing function-structure relationships in the human visual system with functional MRI and diffusion tensor imaging. Neuroimage, 2004. **21**: p. 1452-1463.

31.   Verstynen, T., et al., In vivo mapping of microstructural somatotopies in the human corticospinal pathways. Journal of Neurophysiology, 2011. **105**(1): p. 336-346.

32.   Yeh, F.-C., et al., Deterministic Diffusion Fiber Tracking Improved by Quantitative Anisotropy. PLoS One, 2013. **8**(11): p. e80713.

33.   Radanovic, M., et al., White matter abnormalities associated with Alzheimer's disease and mild cognitive impairment: a critical review of MRI studies. Expert Review of Neurotherapeutics, 2013. **13**(5): p. 483-493.

34.   Rizzo, G., et al., Diffusion-weighted brain imaging study of patients with clinical diagnosis of corticobasal degeneration, progressive supranuclear palsy and Parkinson's disease. Brain : a journal of neurology, 2008. **131**(Pt 10): p. 2690-2700.

35.   Fernandez-Miranda, J.C., S. Pathak, and W. Schneider, High-definition fiber tractography and language. J Neurosurg, 2010. **113**(1): p. 156-7; author reply 157-8.

36.   Yeh, F.-C., V.J. Wedeen, and W. Tseng, Generalized q-sampling imaging. IEEE transactions on medical imaging, 2010. **29**(9): p. 1626.

37.   Tournier, J.D., F. Calamante, and A. Connelly, Robust determination of the fibre orientation distribution in diffusion MRI: non-negativity constrained super-resolved spherical deconvolution. NeuroImage, 2007. **35**(4): p. 1459-1472.

38.   Tournier, J.D., et al., Direct estimation of the fiber orientation density function from diffusion-weighted MRI data using spherical deconvolution. NeuroImage, 2004. **23**(3): p. 1176-1185.

39.   Zhang, H., et al., NODDI: practical in vivo neurite orientation dispersion and density imaging of the human brain. NeuroImage, 2012. **61**(4): p. 1000-1016.

40. Einstein, A., Investigations on the Theory of the Brownian Movement. Annalen der Physik, 1905. **17**: p. 549.

41. Assaf, Y. and P.J. Basser, Composite hindered and restricted model of diffusion (CHARMED) MR imaging of the human brain. Neuroimage, 2005. **27**(1): p. 48-58.

42. Assaf, Y., et al., AxCaliber: a method for measuring axon diameter distribution from diffusion MRI. Magn Reson Med, 2008. **59**(6): p. 1347-54.

43. Assaf, Y., et al., New modeling and experimental framework to characterize hindered and restricted water diffusion in brain white matter. Magn Reson Med, 2004. **52**(5): p. 965-78.

44. Clark, C.A., M. Hedehus, and M.E. Moseley, In vivo mapping of the fast and slow diffusion tensors in human brain. Magnetic resonance in medicine, 2002. **47**: p. 623-8.

45. Clark, C.A. and D. Le Bihan, Water diffusion compartmentation and anisotropy at high b values in the human brain. Magnetic Resonance in Medicine, 2000. **44**: p. 852-859.

46. Stejskal, E. and J. Tanner, Spin diffusion measurements: spin echoes in the presence of a time-dependent field gradient. The journal of chemical physics, 1965. **42**(1): p. 288-292.

47. Callaghan, P.T., et al., Diffraction-like effects in NMR diffusion studies of fluids in porous solids. 1991.

48. Wedeen, V.J., et al., Mapping complex tissue architecture with diffusion spectrum magnetic resonance imaging. Magn Reson Med, 2005. **54**(6): p. 1377-86.

49. Wedeen, V.J., et al., Diffusion spectrum magnetic resonance imaging (DSI) tractography of crossing fibers. Neuroimage, 2008. **41**(4): p. 1267-77.

50. Assemlal, H.-E., et al., Recent advances in diffusion MRI modeling: Angular and radial reconstruction. Medical image analysis, 2011. **15**(4): p. 369-396.

51. Hagmann, P., et al., Understanding diffusion MR imaging techniques: from scalar diffusion-weighted imaging to diffusion tensor imaging and beyond. Radiographics, 2006. **26 Suppl 1**: p. S205-23.

52. Lenglet, C., et al., Mathematical methods for diffusion MRI processing. Neuroimage, 2009. **45**(1): p. S111-S122.

53. Caruyer, E., et al., Optimal Design of Multiple Q-shells experiments for Diffusion MRI, in MICCAI Workshop on Computational Diffusion MRI - CDMRI'11. 2011.

54. Cheng, J., et al., Novel Single and Multiple Shell Uniform Sampling Schemes for Diffusion MRI Using Spherical Codes, in Medical Image Computing and Computer-Assisted Intervention - MICCAI 2015. 2015.

55. Jones, D.K., The Effect of Gradient Sampling Schemes on Measures Derived from Diffusion Tensor MRI: A Monte Carlo Study. Magnetic Resonance in Medicine, 2004. **51**: p. 807-815.

56. Khan, A., L. Wang, and M. Beg, FreeSurfer-initiated fully-automated subcortical brain segmentation in MRI using large deformation diffeomorphic metric mapping. Neuroimage, 2008.

57. Le Bihan, D., et al., Diffusion tensor imaging: concepts and applications. Journal of magnetic resonance imaging, 2001. **13**(4): p. 534-546.

58. Tuch, D.S., et al., High angular resolution diffusion imaging reveals intravoxel white matter fiber heterogeneity. Magn Reson Med, 2002. **48**(4): p. 577-82.

59. Tuch, D.S., et al., Diffusion MRI of complex neural architecture. Neuron, 2003. **40**(5): p. 885-95.

60. Descoteaux, M., et al., A fast and robust odf estimation algorithm in q-ball imaging, in Biomedical Imaging: Nano to Macro, 2006. 3rd IEEE International Symposium on. 2006, IEEE. p. 81-84.

61. Descoteaux, M., et al., Regularized, fast, and robust analytical Q???ball imaging. Magnetic Resonance in Medicine, 2007. **58**(3): p. 497-510.

62. Caruyer, E., et al., Design of multishell sampling schemes with uniform coverage in diffusion MRI. Magnetic resonance in medicine, 2013. **69**: p. 1534-40.

63. Aganj, I., C. Lenglet, and G. Sapiro. ODF reconstruction in q-ball imaging with solid angle consideration. in Biomedical Imaging: From Nano to Macro, 2009. ISBI'09. IEEE International Symposium on. 2009. IEEE.

64. Tristan-Vega, A. and C.F. Westin, Probabilistic ODF estimation from reduced HARDI data with sparse regularization. Med Image Comput Comput Assist Interv, 2011. **14**(Pt 2): p. 182-90.

65. Tristan-Vega, A., C.F. Westin, and S. Aja-Fernandez, Estimation of fiber orientation probability density functions in high angular resolution diffusion imaging. Neuroimage, 2009. **47**(2): p. 638-50.

66. Hagmann, P., et al., Mapping human whole-brain structural networks with diffusion MRI. PLoS One, 2007. **2**(7): p. e597.

67. Pierpaoli, C. and P.J. Basser, Toward a quantitative assessment of diffusion anisotropy. Magn Reson Med, 1996. **36**(6): p. 893-906.

68. Basser, P.J., J. Mattiello, and D. LeBihan, Estimation of the effective self-diffusion tensor from the NMR spin echo. J Magn Reson B, 1994. **103**(3): p. 247-54.

69. Basser, P.J., Inferring microstructural features and the physiological state of tissues from diffusion-weighted images. NMR in Biomedicine, 1995. **8**(7): p. 333-344.

70. Perrin, M., et al., Validation of q-ball imaging with a diffusion fibre-crossing phantom on a clinical scanner. Philosophical transactions of the Royal Society of London. Series B, Biological sciences, 2005. **360**: p. 881-891.

71. Raunig, D.L., et al., Quantitative imaging biomarkers: A review of statistical methods for technical performance assessment. Statistical methods in medical research, 2014.

72. Reischauer, C., et al., Construction of a temperature-controlled diffusion phantom for quality control of diffusion measurements. Journal of Magnetic Resonance Imaging, 2009. **29**: p. 692-698.

73. Wang, Z.J., et al., A quality assurance protocol for diffusion tensor imaging using the head phantom from American College of Radiology. Medical physics, 2011. **38**: p. 4415-4421.

74. Fieremans, E., et al., Simulation and experimental verification of the diffusion in an anisotropic fiber phantom. Journal of Magnetic Resonance, 2008. **190**: p. 189-199.

75. Fillard, P., et al., Quantitative evaluation of 10 tractography algorithms on a realistic diffusion MR phantom. Neuroimage, 2011. **56**(1): p. 220-234.

76. Psychology Software Tools, Inc.

77. Basser, P.J., Relationships between diffusion tensor and q-space MRI. Magn Reson Med, 2002. **47**(2): p. 392-7.

78. Beaulieu, C., The basis of anisotropic water diffusion in the nervous system-a technical review. NMR in Biomedicine, 2002. **15**(7-8): p. 435-455.

79. Le Bihan, D., Looking into the functional architecture of the brain with diffusion MRI. Nature Reviews Neuroscience, 2003. **4**(6): p. 469-480.

80. Namimoto, T., et al., Measurement of the apparent diffusion coefficient in diffuse renal disease by diffusion-weighted echo-planar MR imaging. Journal of Magnetic Resonance Imaging, 1999. **9**(6): p. 832-837.

81. Schlaug, G., et al., Time course of the apparent diffusion coefficient (ADC) abnormality in human stroke. Neurology, 1997. **49**(1): p. 113-119.

82. Tievsky, A.L., T. Ptak, and J. Farkas, Investigation of apparent diffusion coefficient and diffusion tensor anisotropy in acute and chronic multiple sclerosis lesions. American Journal of Neuroradiology, 1999. **20**(8): p. 1491-1499.

83. Xing, D., et al., Optimised diffusion-weighting for measurement of apparent diffusion coefficient (ADC) in human brain. Magnetic resonance imaging, 1997. **15**(7): p. 771-784.

84. Yamasaki, F., et al., Apparent Diffusion Coefficient of Human Brain Tumors at MR Imaging 1. Radiology, 2005. **235**(3): p. 985-991.

85. Cheng, J., et al., Model-free and analytical EAP reconstruction via spherical polar Fourier diffusion MRI, in Lecture Notes in Computer Science (including subseries Lecture Notes in Artificial Intelligence and Lecture Notes in Bioinformatics). 2010. p. 590-597.

86. \"Ozarslan, E., et al., Mean apparent propagator (MAP) MRI: A novel diffusion imaging method for mapping tissue microstructure. NeuroImage, 2013. **78**: p. 16-32.

87. Delputte, S. and E. Fieremans, Quantitative validation of white matter fiber tractography by use of an anatomically realistic synthetic diffusion tensor phantom. Proc. Intl. Soc. Mag. \ldots, 2006. **14**: p. 2739.

88. Ardelean, I. and R. Kimmich, Diffusion measurements with the pulsed gradient nonlinear spin echo method. Journal of Chemical Physics, 2000. **112**(12): p. 5275-5280.

89. Moseley, M.E., et al., Anisotropy in diffusion-weighted MRI. Magnetic Resonance in Medicine, 1991. **19**(2): p. 321-326.

90. Mullins, M.E., et al., CT and Conventional and Diffusion-weighted MR Imaging in Acute Stroke: Study in 691 Patients at Presentation to the Emergency Department 1. Radiology, 2002. **224**(2): p. 353-360.

91. Lansberg, M.G., et al., Evolution of apparent diffusion coefficient, diffusion-weighted, and T2-weighted signal intensity of acute stroke. American Journal of Neuroradiology, 2001. **22**(4): p. 637-644.

92. Warach, S., et al., Fast magnetic resonance diffusion-weighted imaging of acute human stroke. Neurology, 1992. **42**(9): p. 1717-1717.

93. Fiebach, J., et al., Serial analysis of the apparent diffusion coefficient time course in human stroke. Neuroradiology, 2002. **44**(4): p. 294-298.

94. Fieremans, E., A. Pires, and J.H. Jensen, A simple isotropic phantom for diffusional kurtosis imaging. Magnetic Resonance in Medicine, 2012. **68**: p. 537-542.

95. Pierpaoli, C., et al., Diffusion tensor MR imaging of the human brain. Radiology, 1996. **201**(3): p. 637-48.

96. Mori, S. and P. van Zijl, Fiber tracking: principles and strategies - a technical review. NMR in biomedicine, 2002. **15**(7-8): p. 468-480.

97. Chang, L.C., D.K. Jones, and C. Pierpaoli, RESTORE: Robust estimation of tensors by outlier rejection. Magnetic Resonance in Medicine, 2005. **53**: p. 1088-1095.

98. Kindlmann, G., et al., Two-tensor fiber tractography, in Biomedical Imaging: From Nano to Macro, 2007. ISBI 2007. 4th IEEE International Symposium on. 2007. p. 796-799.

99.	Pajevic, S. and C. Pierpaoli, Color schemes to represent the orientation of anisotropic tissues from diffusion tensor data: Application to white matter fiber tract mapping in the human brain. Magnetic Resonance in Medicine, 1999. **42**(3): p. 526-540.

100.	Westin, C.F., et al., Processing and visualization for diffusion tensor MRI. Med Image Anal, 2002. **6**(2): p. 93-108.

101.	Focke, N.K., et al., Voxel-based diffusion tensor imaging in patients with mesial temporal lobe epilepsy and hippocampal sclerosis. Neuroimage, 2008. **40**(2): p. 728-737.

102.	Thivard, L., et al., Diffusion tensor imaging in medial temporal lobe epilepsy with hippocampal sclerosis. Neuroimage, 2005. **28**(3): p. 682-690.

103.	Assaf, Y., et al., High b-value q-space analyzed diffusion-weighted MRI: application to multiple sclerosis. Magn Reson Med, 2002. **47**(1): p. 115-26.

104.	Filippi, M., et al., Diffusion tensor magnetic resonance imaging in multiple sclerosis. Neurology, 2001. **56**(3): p. 304-311.

105.	Werring, D., et al., Diffusion tensor imaging of lesions and normal-appearing white matter in multiple sclerosis. Neurology, 1999. **52**(8): p. 1626-1626.

106.	Weaver, K., et al., Longitudinal diffusion tensor imaging in Huntington's Disease. Experimental neurology, 2009. **216**(2): p. 525-529.

107.	Jones, D.K., Challenges and limitations of quantifying brain connectivity in vivo with diffusion MRI. Imaging, 2010. **2**(3): p. 341-355.

108.	Koay, C.G., et al., A unifying theoretical and algorithmic framework for least squares methods of estimation in diffusion tensor imaging. J Magn Reson, 2006. **182**(1): p. 115-25.

109.	Barmpoutis, A., et al., Regularized positive-definite fourth order tensor field estimation from DW-MRI. NeuroImage, 2009. **45**(1 Suppl): p. 62.

110.	Barmpoutis, A., et al., Symmetric positive 4th order tensors & their estimation from diffusion weighted MRI. Information processing in medical imaging : proceedings of the ... conference, 2007. **20**: p. 308-319.

111.	Alexander, D.C., Multiple-fiber reconstruction algorithms for diffusion MRI, in Annals of the New York Academy of Sciences. 2005. p. 113-133.

112.	Parker, G.J.M. and D.C. Alexander, Probabilistic anatomical connectivity derived from the microscopic persistent angular structure of cerebral tissue. Philosophical transactions of the Royal Society of London. Series B, Biological sciences, 2005. **360**: p. 893-902.

113.   Pasternak, O., N. Sochen, and Y. Assaf, Variational regularization of multiple diffusion tensor fields, in Visualization and Processing of Tensor Fields. 2006, Springer Berlin Heidelberg. p. 165-176.

114.   Jensen, J.H., et al., Diffusional kurtosis imaging: The quantification of non-Gaussian water diffusion by means of magnetic resonance imaging. Magnetic Resonance in Medicine, 2005. **53**: p. 1432-1440.

115.   Levenberg, K., A Method for the Solution of Certain Non-Linear Problems in Least Squares. Quarterly of Applied Mathematics, 1944. **2**: p. 164-168.

116.   Marquardt, D.W. An Algorithm for Least-Squares Estimation of Nonlinear Parameters. Journal of the Society for Industrial and Applied Mathematics 1963 [cited 11; 431-441]. Available from: 10.1137/0111030.

117.   Alexander, D.C., G.J. Barker, and S.R. Arridge, Detection and modeling of non-Gaussian apparent diffusion coefficient profiles in human brain data. Magn Reson Med, 2002. **48**: p. 331-340.

118.   Behrens, T., et al., Characterization and propagation of uncertainty in diffusion-weighted MR imaging. Magnetic resonance in medicine, 2003. **50**(5): p. 1077-1088.

119.   Sotiropoulos, S.N., T.E. Behrens, and S. Jbabdi, Ball and rackets: inferring fiber fanning from diffusion-weighted MRI. Neuroimage, 2012. **60**(2): p. 1412-1425.

120.   Ypma, T.J. Historical Development of the Newton–Raphson Method. SIAM Review 1995 [cited 37; 531-551]. Available from: 10.1137/1037125.

121.   Courant, R. and D. Hilbert, Methods of Mathematical Physics, Volume 1. 1966: p. 561.

122.   Kuo, L.W., et al., Optimization of diffusion spectrum imaging and q-ball imaging on clinical MRI system. Neuroimage, 2008. **41**(1): p. 7-18.

123.   Feinberg, D.A. and K. Setsompop, Ultra-fast MRI of the human brain with simultaneous multi-slice imaging. Journal of Magnetic Resonance, 2013. **229**: p. 90-100.

124.   Setsompop, K., et al., Blipped-controlled aliasing in parallel imaging for simultaneous multislice echo planar imaging with reduced g-factor penalty. Magnetic Resonance in Medicine, 2012. **67**(5): p. 1210-1224.

125.   White, N., et al., Probing tissue microstructure with restriction spectrum imaging: Histological and theoretical validation. Human brain mapping, 2013. **34**(2): p. 327-346.

126.   Tournier, J.D., et al., Resolving crossing fibres using constrained spherical deconvolution: Validation using diffusion-weighted imaging phantom data. NeuroImage, 2008. **42**: p. 617-625.

127. Jeurissen, B., et al., Multi-tissue constrained spherical deconvolution for improved analysis of multi-shell diffusion MRI data. NeuroImage, 2014.

128. Seunarine, K., & Alexander, D. Linear persistent angular structure MRI and non-linear spherical deconvolution for diffusion MRI. in ISMRM. 2006.

129. Dell'Acqua, F., et al., A modified damped Richardson-Lucy algorithm to reduce isotropic background effects in spherical deconvolution. Neuroimage, 2010. **49**(2): p. 1446-1458.

130. Schultz, T., C.F. Westin, and G. Kindlmann, Multi-diffusion-tensor fitting via spherical deconvolution: a unifying framework. Med Image Comput Comput Assist Interv, 2010. **13**(Pt 1): p. 674-81.

131. Tax, C.M.W., et al., Recursive calibration of the fiber response function for spherical deconvolution of diffusion MRI data. Neuroimage, 2014. **86**: p. 67-80.

132. Cook, P., Alexander, D. C., & Parker, G. J. Modelling noise-induced fibre-orientation error in diffusion-tensor MRI. in Biomedical Imaging: Nano to Macro. 2004. IEEE International Symposium.

133. Malcolm, J.G., et al., A filtered approach to neural tractography using the Watson directional function. Medical Image Analysis, 2010. **14**(1): p. 58-69.

134. Kent, J.T., The Fisher-Bingham Distribution on the Sphere. Journal of the Royal Statistical Society Series B-Methodological, 1982. **44**(1): p. 71-80.

135. MATLAB, version 8.0 (R2012b). 2012, Natick, Massachusetts: The MathWorks Inc.

136. Raffelt, D., et al., Reorientation of fiber orientation distributions using apodized point spread functions. Magnetic Resonance in Medicine, 2012. **67**(3): p. 844-855.

137. Yeh, F.C. Diffusion Spectrum Imaging Studio: Recontruction, Fiber Tracking and Visulization of Diffusion MR Images.

138. Jenkinson, M., et al., FSL. NeuroImage, 2012. **62**(2): p. 782-790.

139. Behrens, T., et al., Non-invasive mapping of connections between human thalamus and cortex using diffusion imaging. Nature neuroscience, 2003. **6**(7): p. 750-757.

140. Calamante, F., et al., Super-resolution track-density imaging of thalamic substructures: Comparison with high-resolution anatomical magnetic resonance imaging at 7.0T. Human Brain Mapping, 2013. **34**: p. 2538-2548.

141. Jonasson, L., et al., A level set method for segmentation of the thalamus and its nuclei in DT-MRI. Signal Processing, 2007. **87**: p. 309-321.

142. Rittner, L., et al., Segmentation of thalamic nuclei based on tensorial morphological gradient of diffusion tensor fields, in 2010 7th IEEE International Symposium on

Biomedical Imaging: From Nano to Macro, ISBI 2010 - Proceedings. 2010. p. 1173-1176.

143.   Schultz, T., Segmenting thalamic nuclei: What can we gain from HARDI? Lecture Notes in Computer Science (including subseries Lecture Notes in Artificial Intelligence and Lecture Notes in Bioinformatics), 2011. **6892 LNCS**: p. 141-148.

144.   Ziyan, U., D. Tuch, and C.-F. Westin, Segmentation of thalamic nuclei from DTI using spectral clustering. Medical image computing and computer-assisted intervention : MICCAI ... International Conference on Medical Image Computing and Computer-Assisted Intervention, 2006. **9**: p. 807-814.

145.   Glimcher, P.W. and B. Lau, Rethinking the thalamus., in Nature neuroscience. 2005. p. 983-984.

146.   Sherman, S.M. and R.W. Guillery, Exploring the thalamus. San DiegoAcademic Press, 2006: p. 497.

147.   Perlmutter, J.S. and J.W. Mink, Deep brain stimulation. Annual review of neuroscience, 2006. **29**: p. 229-257.

148.   Torres, C.V., et al., Deep brain stimulation of the ventral intermediate nucleus of the thalamus for tremor in patients with multiple sclerosis. Neurosurgery, 2010. **67**: p. 646-651.

149.   Loddenkemper, T. and A. Pan, Deep brain stimulation in epilepsy. Journal of Clinical Neurophysiology, 2001. **116**: p. 217-34.

150.   Boertien, T., et al., Functional imaging of subthalamic nucleus deep brain stimulation in Parkinson's disease. Movement disorders : official journal of the Movement Disorder Society, 2011. **26**: p. 1835-43.

151.   Voon, V., et al., Deep brain stimulation: Neuropsychological and neuropsychiatric issues, in Movement Disorders. 2006.

152.   Lukhanina, E.P., Functional organization of the ventrolateral nucleus of the thalamus, in Neurophysiology. 1994. p. 378-390.

153.   Marlinski, V., et al., Signals from the ventrolateral thalamus to the motor cortex during locomotion, in Journal of Neurophysiology. 2012. p. 455-472.

154.   Groenewegen, H.J. and H.W. Berendse, The specificity of the 'nonspecific' midline and intralaminar thalamic nuclei, in Trends in Neurosciences. 1994. p. 52-57.

155.   Kinomura, S., et al., Activation by attention of the human reticular formation and thalamic intralaminar nuclei. Science (New York, N.Y.), 1996. **271**: p. 512-515.

156. Dimitrova, A., et al., Probabilistic 3D MRI atlas of the human cerebellar dentate/interposed nuclei. NeuroImage, 2006. **30**: p. 12-25.

157. Habas, C., Functional imaging of the deep cerebellar nuclei: A review, in Cerebellum. 2010. p. 22-28.

158. Jansen, A., et al., Crossed cerebro-cerebellar language dominance. Human Brain Mapping, 2005. **24**: p. 165-172.

159. Salmi, J., et al., Cognitive and motor loops of the human cerebro-cerebellar system. Journal of cognitive neuroscience, 2010. **22**: p. 2663-2676.

160. Stoodley, C.J. and J.D. Schmahmann, The cerebellum and language: Evidence from patients with cerebellar degeneration. Brain and Language, 2009. **110**: p. 149-153.

161. Maderwald, S., et al., 3D visualization of deep cerebellar nuclei using 7T MRI, in Proceedings 17th Scientific Meeting, International Society for Magnetic Resonance in Medicine. 2009. p. 963.

162. Deoni, S.C.L. and M. Catani, Visualization of the deep cerebellar nuclei using quantitative T1 and rho magnetic resonance imaging at 3 Tesla. NeuroImage, 2007. **37**: p. 1260-1266.

163. Diedrichsen, J., A spatially unbiased atlas template of the human cerebellum. NeuroImage, 2006. **33**: p. 127-138.

164. Dimitrova, A., et al. MRI atlas of the human cerebellar nuclei. in NeuroImage. 2002.

165. Erzurumlu, R.S., Y. Murakami, and F.M. Rijli, Mapping the face in the somatosensory brainstem. Nature reviews. Neuroscience, 2010. **11**: p. 252-263.

166. Ngeles Fernández-Gil, M., et al., Anatomy of the brainstem: A gaze into the stem of life. Seminars in Ultrasound, CT and MRI, 2010. **31**: p. 196-219.

167. Parvizi, J. and A. Damasio, Consciousness and the brainstem, in Cognition. 2001. p. 135-160.

168. Parvizi, J. and A.R. Damasio, Neuroanatomical correlates of brainstem coma. Brain : a journal of neurology, 2003. **126**: p. 1524-1536.

169. Russo, N., et al., Brainstem responses to speech syllables. Clinical Neurophysiology, 2004. **115**: p. 2021-2030.

170. Travagli, R.A., et al., Brainstem circuits regulating gastric function. Annual review of physiology, 2006. **68**: p. 279-305.

171. Alvarez-Linera, J., Magnetic resonance techniques for the brainstem. Seminars in ultrasound, CT, and MR, 2010. **31**: p. 230-245.

172. Flannigan, B.D., et al., Magnetic resonance imaging of the brainstem: normal structure and basic functional anatomy. Radiology, 1985. **154**: p. 375-383.

173. Ford, A.A., et al., Imaging white matter in human brainstem. Frontiers in human neuroscience, 2013. **7**: p. 400.

174. Burtscher, M., Computational Simulation and Visualization of Traumatic Brain Injuries. Injury: p. 0-6.

175. Jang, S.H., Somatotopic arrangement and location of the corticospinal tract in the brainstem of the human brain. Yonsei Medical Journal, 2011. **52**: p. 553-557.

176. Lee, S.H., et al., Sensory dermatomal representation in the medial lemniscus. Archives of neurology, 2001. **58**: p. 649-651.

177. Yang, J. and J. Dai, Simulation-based assessment of rear effect to ballistic helmet impact. Computer-Aided Design and Applications, 2010. **7**: p. 59-73.

178. Andrew, D. and A.D. Craig, Spinothalamic lamina I neurons selectively sensitive to histamine: a central neural pathway for itch. Nature neuroscience, 2001. **4**: p. 72-77.

179. Foreman, R.D., et al., Effects of dorsal column stimulation on primate spinothalamic tract neurons. Journal of neurophysiology, 1976. **39**: p. 534-546.

180. Wasner, G., et al., Residual spinothalamic tract pathways predict development of central pain after spinal cord injury. Brain : a journal of neurology, 2008. **131**: p. 2387-2400.

181. Dergacheva, O., et al., Respiratory modulation of premotor cardiac vagal neurons in the brainstem, in Respiratory Physiology and Neurobiology. 2010. p. 102-110.

182. Gaffan, D. and E.A. Gaffan, Amnesia in man following transection of the fornix. A review. Brain : a journal of neurology, 1991. **114 (Pt 6**: p. 2611-2618.

183. Gale, S.D., et al., Fornix degeneration and memory in traumatic brain injury. Brain Research Bulletin, 1993. **32**: p. 345-349.

184. Fitzsimmons, J., et al., Diffusion tractography of the fornix in schizophrenia. Schizophrenia Research, 2009. **107**: p. 39-46.

185. Hofstetter, S., et al., Short-term learning induces white matter plasticity in the fornix. The Journal of neuroscience : the official journal of the Society for Neuroscience, 2013. **33**: p. 12844-50.

186. Cho, G.Y., et al., A versatile flow phantom for intravoxel incoherent motion MRI. Magnetic Resonance in Medicine, 2012. **67**: p. 1710-1720.

187. Hong, J.H., et al., The anatomical location of the arcuate fasciculus in the human brain: A diffusion tensor tractography study. Brain Research Bulletin, 2009. **80**(1-2): p. 52-55.

188. Rilling, J.K., et al., The evolution of the arcuate fasciculus revealed with comparative DTI. Nature Neuroscience, 2008. **11**(4): p. 426-428.

189. Bernal, B. and A. Ardila, The role of the arcuate fasciculus in conduction aphasia. Brain, 2009. **132**: p. 2309-2316.

190. Fernandez-Miranda, J.C., et al., Asymmetry, connectivity, and segmentation of the arcuate fascicle in the human brain. Brain Struct Funct, 2015. **220**(3): p. 1665-80.

191. Catani, M., et al. Virtual in vivo interactive dissection of white matter fasciculi in the human brain. in NeuroImage. 2002.

192. Jellison, B.J., et al., Diffusion Tensor Imaging of Cerebral White Matter: A Pictorial Review of Physics, Fiber Tract Anatomy, and Tumor Imaging Patterns, in American Journal of Neuroradiology. 2004. p. 356-369.

193. Perrini, P., et al., Three-dimensional microsurgical anatomy of cerebellar peduncles. Neurosurgical Review, 2013. **36**: p. 215-224.

194. Benjamini, D., et al., Nonparametric pore size distribution using d-PFG: Comparison to s-PFG and migration to MRI. Journal of Magnetic Resonance, 2014. **246**: p. 36-45.

195. Clark, K.A., et al., Mean diffusivity and fractional anisotropy as indicators of disease and genetic liability to schizophrenia. Journal of Psychiatric Research, 2011. **45**: p. 980-988.

196. Ozsunar, Y., et al., Evolution of water diffusion and anisotropy in hyperacute stroke: Significant correlation between fractional anisotropy and T2. American Journal of Neuroradiology, 2004. **25**: p. 699-705.

197. Beppu, T., et al., Measurement of fractional anisotropy using diffusion tensor MRI in supratentorial astrocytic tumors. Journal of Neuro-Oncology, 2003. **63**: p. 109-116.

198. Khong, P.-L., et al., White matter anisotropy in post-treatment childhood cancer survivors: preliminary evidence of association with neurocognitive function. Journal of Clinical Oncology, 2006. **24**: p. 884-90.

199. Kinoshita, M., et al., Fractional anisotropy and tumor cell density of the tumor core show positive correlation in diffusion tensor magnetic resonance imaging of malignant brain tumors. NeuroImage, 2008. **43**: p. 29-35.

200. Roberts, T.P.L., et al., Fiber density index correlates with reduced fractional anisotropy in white matter of patients with glioblastoma. American Journal of Neuroradiology, 2005. **26**: p. 2183-2186.

201. Seal, M.L., et al., Abnormal white matter microstructure in schizophrenia: A voxelwise analysis of axial and radial diffusivity. Schizophrenia Research, 2008. **101**: p. 106-110.

202. Basser, P.J., J. Mattiello, and D. LeBihan, MR diffusion tensor spectroscopy and imaging. Biophys J, 1994. **66**(1): p. 259-67.

203. Alexander, D.C., A general framework for experiment design in diffusion MRI and its application in measuring direct tissue-microstructure features. Magnetic Resonance in Medicine, 2008. **60**(2): p. 439-448.

204. Alexander, D.C., et al., Orientationally invariant indices of axon diameter and density from diffusion MRI. Neuroimage, 2010. **52**(4): p. 1374-1389.

205. Leow, A.D., et al., White matter integrity measured by fractional anisotropy correlates poorly with actual individual fiber anisotropy, in Proceedings - 2009 IEEE International Symposium on Biomedical Imaging: From Nano to Macro, ISBI 2009. 2009. p. 622-625.

206. Cykowski, M.D., et al., A study of the reproducibility and etiology of diffusion anisotropy differences in developmental stuttering: A potential role for impaired myelination. NeuroImage, 2010. **52**: p. 1495-1504.

207. Sakuma, H., et al., Adult and neonatal human brain: diffusional anisotropy and myelination with diffusion-weighted MR imaging. Radiology, 1991. **180**: p. 229-233.

208. Komlosh, M., et al., Detection of microscopic anisotropy in gray matter and in a novel tissue phantom using double pulsed gradient spin echo MR. Journal of magnetic resonance, 2007. **189**(1): p. 38-45.

209. Komlosh, M.E., et al., Pore diameter mapping using double pulsed-field gradient MRI and its validation using a novel glass capillary array phantom. Journal of Magnetic Resonance, 2011. **208**: p. 128-135.

210. Chau, W. and A.R. McIntosh, The Talairach coordinate of a point in the MNI space: How to interpret it. NeuroImage, 2005. **25**: p. 408-416.

211. Collins, D.L. and J.C. Pruessner, Towards accurate, automatic segmentation of the hippocampus and amygdala from MRI by augmenting ANIMAL with a template library and label fusion. NeuroImage, 2010. **52**: p. 1355-1366.

212. Jao, T., et al., Development of NTU standard Chinese brain template: Morphologic and functional comparison with MNI template using magnetic resonance imaging, in Proceedings of the 31st Annual International Conference of the IEEE Engineering in Medicine and Biology Society: Engineering the Future of Biomedicine, EMBC 2009. 2009. p. 4779-4782.

213. Lalys, F., et al., Construction and assessment of a 3-T MRI brain template. NeuroImage, 2010. **49**: p. 345-354.

214. Roland, P.E., et al., Human brain atlas: For high-resolution functional and anatomical mapping. Human Brain Mapping, 1993. **1**: p. 173-184.

215. Chen, T., et al., Construction of a neuroanatomical shape complex atlas from 3D MRI brain structures. NeuroImage, 2012. **60**: p. 1778-1787.

216. Evans, A.C., et al., 3D statistical neuroanatomical models from 305 MRI volumes. 1993 IEEE Conference Record Nuclear Science Symposium and Medical Imaging Conference, 1993.

217. Tzourio-Mazoyer, N., et al., Automated anatomical labeling of activations in SPM using a macroscopic anatomical parcellation of the MNI MRI single-subject brain. NeuroImage, 2002. **15**: p. 273-289.

218. Fischl, B., et al., Whole brain segmentation: Automated labeling of neuroanatomical structures in the human brain. Neuron, 2002. **33**: p. 341-355.

219. Klein, A., et al., Evaluation of 14 nonlinear deformation algorithms applied to human brain MRI registration. NeuroImage, 2009. **46**: p. 786-802.

220. Smith, S.M., et al., Tract-based spatial statistics: Voxelwise analysis of multi-subject diffusion data. NeuroImage, 2006. **31**: p. 1487-1505.

221. Smith, S.M., et al., Acquisition and voxelwise analysis of multi-subject diffusion data with tract-based spatial statistics. Nature protocols, 2007. **2**: p. 499-503.

222. Yeatman, J., et al., Tract profiles of white matter properties: automating fiber-tract quantification. PloS one, 2012. **7**(11).

223. Just, M. and M. Thelen, Tissue characterization with T1, T2, and proton density values: results in 160 patients with brain tumors. Radiology, 1988. **169**(3): p. 779-785.

224. Warntjes, J., O. Dahlqvist, and P. Lundberg, Novel method for rapid, simultaneous T1, T*2, and proton density quantification. Magnetic resonance in medicine : official journal of the Society of Magnetic Resonance in Medicine / Society of Magnetic Resonance in Medicine, 2007. **57**(3): p. 528-537.

225. Pasternak, O., M.E. Shenton, and C.F. Westin, Estimation of extracellular volume from regularized multi-shell diffusion MRI. Med Image Comput Comput Assist Interv, 2012. **15**(Pt 2): p. 305-12.

226. Canales-Rodriguez, E.J., et al., Deconvolution in diffusion spectrum imaging. Neuroimage, 2010. **50**(1): p. 136-49.

227. Tournier, J.D., F. Calamante, and A. Connelly, MRtrix: Diffusion tractography in crossing fiber regions. International journal of imaging systems and technology, 2012. **22**(1): p. 53-66.

228. Wang, R., et al., Diffusion toolkit: a software package for diffusion imaging data processing and tractography, in Diffusion toolkit: a software package for diffusion imaging data processing and tractography. 2007. p. 3720.

229. Scherrer, B., et al., Characterizing the DIstribution of Anisotropic MicrO-structural eNvironments with diffusion-weighted imaging (DIAMOND), in Lecture Notes in Computer Science (including subseries Lecture Notes in Artificial Intelligence and Lecture Notes in Bioinformatics). 2013. p. 518-526.

230. Dabrowski, W., et al., A real vessel phantom for imaging experimentation. Medical physics, 1997. **24**: p. 687-693.

231. D'Souza, W.D., et al., Tissue mimicking materials for a multi-imaging modality prostate phantom. Medical physics, 2001. **28**: p. 688-700.

232. Huber, J.S., Q. Peng, and W.W. Moses, Multi-modality phantom development. IEEE Transactions on Nuclear Science, 2009. **56**: p. 2722-2727.

233. Lavdas, I., et al., A phantom for diffusion-weighted MRI (DW-MRI). Journal of Magnetic Resonance Imaging, 2013. **38**: p. 173-179.

234. Malyarenko, D., et al., Multi-system repeatability and reproducibility of apparent diffusion coefficient measurement using an ice-water phantom. Journal of Magnetic Resonance Imaging, 2013. **37**: p. 1238-1246.

235. Mattila, S., et al., Phantom-based evaluation of geometric distortions in functional magnetic resonance and diffusion tensor imaging. Magnetic Resonance in Medicine, 2007. **57**: p. 754-763.

236. Teipel, S.J., et al., Multicenter stability of diffusion tensor imaging measures: A European clinical and physical phantom study. Psychiatry Research - Neuroimaging, 2011. **194**: p. 363-371.

237. Lauterbur, P.C. NMR images of microscopic flow. Nature 1988 [cited 336; 310-310]. Available from: 10.1038/336310a0.

238. Chen, C.C., et al., Quality assurance of clinical MRI scanners using ACR MRI phantom: Preliminary results. Journal of Digital Imaging, 2004. **17**: p. 279-284.

239. RSNA. Quantitative Imaging Biomarkers Alliance. Available from: https://www.rsna.org/QIBA.aspx.

240. Chen, B. and A.W. Song, Diffusion tensor imaging fiber tracking with local tissue property sensitivity: phantom and in vivo validation. Magnetic Resonance Imaging, 2008. **26**: p. 103-108.

241. Chenevert, T.L., et al., Diffusion coefficient measurement using a temperature-controlled fluid for quality control in multicenter studies. Journal of Magnetic Resonance Imaging, 2011. **34**: p. 983-987.

242. Ihalainen, T.M., et al., MRI quality assurance using the ACR phantom in a multi-unit imaging center. Acta oncologica (Stockholm, Sweden), 2011. **50**: p. 966-972.

243.   Huda, W., et al., How good is the ACR accreditation phantom for assessing image quality in digital mammography? Academic Radiology, 2002. **9**: p. 764-772.

244.   Kessler, L.G., et al., The emerging science of quantitative imaging biomarkers terminology and definitions for scientific studies and regulatory submissions. Statistical methods in medical research, 2014.

245.   Avram, L., et al., Three-dimensional water diffusion in impermeable cylindrical tubes: theory versus experiments. NMR Biomed, 2008. **21**(8): p. 888-98.

246.   Baslow, M.H. and D.N. Guilfoyle, Effect of N-acetylaspartic acid on the diffusion coefficient of water: a proton magnetic resonance phantom method for measurement of osmolyte-obligated water. Analytical biochemistry, 2002. **311**(2): p. 133-138.

247.   Yanasak, N. and J. Allison, Use of capillaries in the construction of an MRI phantom for the assessment of diffusion tensor imaging: demonstration of performance. Magnetic Resonance Imaging, 2006. **24**: p. 1349-1361.

248.   Matsuya, R., et al., A new phantom using polyethylene glycol as an apparent diffusion coefficient standard for MR imaging. International Journal of Oncology, 2009. **35**: p. 893-900.

249.   Lee, S., et al., Electrical conductivity estimation from diffusion tensor and T2: a silk yarn phantom study. Proceedings 14th Scientific Meeting, International Society for Magnetic Resonance in Medicine, 2006. **26**: p. 3034.

250.   Horkay, F., C. Pierpaoli, and P.J. Basser. Phantom for diffusion mri imaging. 2010 Januar1 26.

251.   Ogrezeanu, G. and A. Hartlep. Fiber tracking phantom. 2009 Apri1 21.

252.   Bengtsson, S.L., et al., Extensive piano practicing has regionally specific effects on white matter development. Nature neuroscience, 2005. **8**(9): p. 1148-1150.

253.   Scholz, J., et al., Training induces changes in white-matter architecture. Nature neuroscience, 2009. **12**(11): p. 1370-1371.

254.   Fan, Q., et al., Investigating the capability to resolve complex white matter structures with high b-value diffusion magnetic resonance imaging on the MGH-USC Connectom scanner. Brain connectivity, 2014. **4**(9): p. 718-726.

255.   MRICroGL 3D Medical Imaging.

256.   Jenkinson, M., et al., Improved optimization for the robust and accurate linear registration and motion correction of brain images. Neuroimage, 2002. **17**(2): p. 825-841.

257.   Jenkinson, M. and S. Smith, A global optimisation method for robust affine registration of brain images. Medical image analysis, 2001. **5**(2): p. 143-156.

258. Barazany, D., P.J. Basser, and Y. Assaf, In vivo measurement of axon diameter distribution in the corpus callosum of rat brain. Brain, 2009. **132**(5): p. 1210-1220.

259. Stepi\vsnik, J., Time-dependent self-diffusion by NMR spin-echo. Physica B: Condensed Matter, 1993. **183**(4): p. 343-350.

260. Kim, E.Y., et al., Measuring fractional anisotropy of the corpus callosum using diffusion tensor imaging: mid-sagittal versus axial imaging planes. Korean Journal of Radiology, 2008. **9**(5): p. 391-395.